Final Report Prepared Under
NASA Grant NAG 1-837

AERODYNAMICS OF THRUST VECTORING BY NAVIER-STOKES SOLUTIONS

KU-FRL-795-2

Jing-Biau Tseng

and

C. Edward Lan

Flight Research Laboratory
The University of Kansas Center for Research, Inc.
Lawrence, Kansas 66045-2969

February 1991

ABSTRACT

Induced aerodynamics from thrust vectoring are investigated in the present study by a computational fluid-dynamic method. A thin-layer Reynolds-averaged Navier-Stokes code with multiblock capability is used. Jet properties are specified on the nozzle exit plane to simulate the jet momentum. Results for a rectangular jet in a cross flow are compared with data to verify the code. Further verification of the calculation is made by comparing the numerical results with transonic data for a wing-body combination. Additional calculations are performed to elucidate the following thrust vectoring effects:

- thrust-vectoring effect on shock and expansion waves,
- induced effects on nearby surfaces, and
- thrust-vectoring effect on the leading-edge vortex.

These calculations are performed on a body with a rectangular nozzle and a thick delta wing of 63-deg sweep. The results show that a vectored jet induces flow acceleration and lower pressure in the region with flow expansion. Flow deceleration and higher pressure exist in the region of flow compression. When a jet is vectored downwards, incremental lift, drag and negative pitching moment are induced. Furthermore, induced flow acceleration from a vectored jet can change the strength and location of the shock and expansion waves. These results depend significantly on the magnitude of jet static pressure. Calculation with the delta wing indicates that vectored thrust makes leading-edge vortices less diffusive.

TABLE OF CONTENTS

LIST OF SYMBOLS

a	speed of sound
b	span
C	speed of sound
C_T	gross thrust coefficient along the jet axis
e	total energy per unit volume
F	flux
G	flux
H	flux or enthalpy
F_{ijk}	surface integral
J	volume of a cell
k	heat transfer coefficient
$k^{(2)}$	artificial damping coefficient
$k^{(4)}$	artificial damping coefficient
M	Mach number
P	pressure
P^i	control function for elliptic grid generation
P_r	Prandtl number
q,Q	flow-variable vector
r	radius of curvature
R	jet-to-freestream velocity ratio
R_e	Reynolds number

S	area of cell surfaces
S_{ref}	reference area
T	temperature
u	velocity component in the x-direction
v	velocity component in the y-direction
w	velocity component in the z-direction
x,y,z	Cartesian coordinates
X	length of the afterbody, or local chord length
α	angle of attack
γ	specific heat ratio
δ_d	jet deflection angle
Δ, δ^+	forward difference
∇, δ^-	backward difference
ε	eddy viscosity
λ	coefficient of bulks viscosity
μ	viscosity
ρ	density
τ	shear stress
υ	artificial damping sensor
ω	vorticity

1. INTRODUCTION

Thrust vectoring has been considered as a means to enhance maneuverability and aerodynamic performance of a tactical aircraft (Refs. 1-17). This concept usually involves the installation of multifunctional nozzles. With the multifunctional nozzles, the engine thrust can be changed in direction without changing the attitude of the aircraft. A change in the thrust direction can induce extra aerodynamic forces on the aircraft. Therefore, this device can be used for lift-augmentation as well as stability and control purposes. When the jet stream is deflected in the longitudinal direction, the lift force and pitching stability can be manipulated, while yawing stability can be controlled by directing the thrust in the lateral direction.

The augmented lift force from thrust vectoring can also be used for short takeoff and landing (STOL) purposes (Ref. 17). This will allow highways, small airports, and bombed runways to be bases for fighter operations (Ref. 10), not to mention the safer landing operations on aircraft carriers provided by using this concept. Also, the induced aerodynamic forces from thrust vectoring devices allow the aircraft to operate in the high angle-of-attack flight regime (Ref. 14). Most of the current fighter airplanes are limited in high-angle-of-attack maneuverability because of degraded control power. The primary reason for the control power deterioration is that massive flow separation occurs at high angles of attack on the lee side of the airplane. Utilizing the propulsion system and vectoring the

exhaust, powered control can provide auxiliary high-angle-of-attack maneuvering capability (Ref. 6).

On the other hand, the pitching and yawing moments generated from these kinds of devices can be used to enhance or replace the elevator and rudder control power. Test results show that afterbodies of various aircraft comprised 20% to 25% of the total model length but produced 38% to 50% of the total aircraft drag (Ref. 3). Up to half of the afterbody drag results from adverse interference and pressure drag in the afterbody region. One way to eliminate the large adverse interference effect is to reduce the size of, or simply eliminate, the horizontal and vertical tails. This would require some other methods of achieving the necessary control power (Ref. 18). A well-designed thrust- vectoring nozzle providing the required control power can replace the roles of horizontal and vertical tails. Without the adverse interference among control surfaces and afterbody, the total drag of the aircraft can be reduced.

In an attempt to provide vectoring capability by deflecting the jet stream, several devices have been considered. Some of the proposed devices are internal turning vanes, external turning flaps, gimbal nozzles, and ramp expansion nozzles. These devices produce the desired aerodynamic forces on the aircraft by directing the thrust in the longitudinal and/or lateral directions. To determine these forces, experimental investigation has been under way for decades (Refs. 2, 3, 5, 12, 14, 19). To effectively incorporate this technology into future aircraft, the propulsion system must be efficiently integrated into the airframe. This involves determining

the characteristics of afterbody flows in the presence of a jet exhaust. Advanced computational methods are becoming increasingly useful in providing analyses of this nature. Tasks associated with thrust vectoring computation include induced surface pressure calculation, jet deformation effect, crossflow velocity distribution, and induced shock wave at high speed. To fully understand the flow properties of thrust vectoring, interaction between the deflected jet and external flow should be studied first.

Experiments show that a crossflow jet injected from a surface produces low pressures on the surface downstream of the jet exit. There is also a high pressure region due to crossflow deceleration (Ref. 20). The trajectory of the jet mainly depends on the jet-to-freestream speed ratio, the nozzle exit geometry, the jet injection angle, and the jet exit profile (Refs. 21-23). Experiments also show that large-scale rolled-up vortices are generated in a crossflow jet (Ref. 24). These phenomena are expected to be present in the thrust vectoring operation.

Reported numerical simulations of crossflow applications are limited to simple configurations (Refs. 25-31). For configurations having multifunctional nozzles, the flow field about the nozzle exit becomes very complicated due to the interaction among the turning devices, the freestream, and the vectored jet. Jet mixing as well as shock waves induced by the jet turning will be present. For high nozzle pressure ratio (NPR) or supersonic nozzles, the shock waves inside the jet stream will affect the jet deformation. Also, pressure differences across the jet can produce vortices, which will induce jet roll-up. In addition, vectoring the

thrust may create flow expansion in the external region around the nozzle exit. Flow expansion in this region induce shock waves at a transonic speed. With all the complicated flow physics induced from the vectored thrust, methods beyond crossflow prediction are needed for thrust vectoring computation. As a general goal of this study, numerical methods resolving induced aerodynamic effects--namely, pressure distribution change on the control surfaces, shock location variation around the jet exhaust region, and the effect on vortices--should be developed.

One thrust vectoring computational method based on a panel method was developed in Reference 32. Due to the limitation of flow singularity methods, important flow characteristics such as shock waves and shock cells inside the jet stream can not be predicted. Another drawback of panel methods is the absence of the energy (or pressure) term in the computation. Therefore, the jet stream is frequently modeled as a plume or wake, requiring empirical methods to determine the jet shape. To fully understand the induced aerodynamic effects from the jet stream deflection, methods other than a panel approach would be needed.

Methods in Computational Fluid Dynamics (CFD) are more suitable for the present problem. In more recent simulations of unvectored jets, flow characteristics at the nozzle exit plane were specified and the exhaust plume was calculated based on a Navier-Stokes method (Ref. 33). However, calculation for an airplane configuration with a vectored jet has not been reported in the literature. Usually flow properties involved in CFD are density, velocity, energy, and/or

pressure. Boundary conditions can be specified in terms of these quantities. For example, on solid boundaries, velocity components can be specified as zero to simulate the no-slip boundary condition. For thrust vectoring computation, jet exit conditions can be specified on the nozzle exit plane. The jet deformation or trajectory can be calculated instead of using empirical formulas to represent the jet effect.

In the present study of thrust vectoring aerodynamics, nonaxisymmetric nozzle with turning vanes are investigated with a multiple-block thin-layer Reynolds-averaged Navier-Stokes code, CFL3D (Ref. 35). The numerical grid generation program EAGLE (Ref. 34), with the options of algebraic and elliptical grid generation systems, has been used to produce grids in this study. To properly simulate the jet interaction effect, the calculation is carried out inside the jet region as well as the flow field around the nozzle and the airplane configuration. This approach captures the jet deflection trajectory through the thin-layer Reynolds averaged Navier-Stokes equations. Shock cells inside the jet stream and the interaction between the jet and the freestream can also be predicted. For the nozzle of a turning-vane configuration, the vanes are not directly modeled in the present study. Instead, the turning angle, velocity components, and pressure of the jet are specified as boundary conditions on the exit plane. Under most circumstances, available test conditions inside the thrust vectoring nozzles are total temperature and total pressure. To convert total pressure into CFD variables, isentropic expansion formulas are used to determine the jet exit

pressure. The temperature effect is not considered at present. The Navier-Stokes approach of CFL3D (Ref. 35) is based on a finite volume scheme and will be used here for a thrust vectoring nozzle configuration. The finite volume scheme features momentum conservation in the computation. Therefore, this scheme is suitable to calculate the jet momentum transfer.

To verify the jet flow calculation, a 90-degree crossflow jet is treated first. The pressure distribution is compared with experimental measurements. A generic airplane with a rectangular nozzle is used to demonstrate the calculation of the induced pressure and shock location changes due to a vectored jet. Computational results of this configuration with various NPR's and deflection angles will be presented and compared with test results.

To investigate the vectored-jet effect on the leading edge vortex, a 63-degree delta wing integrated with trapezoidal nozzles is used. Pressure distributions and leading-edge vortex filaments under the influences of a straight jet and a vectored jet will be presented. Vectored-jet influence on vortex breakdown will also be discussed.

2. THEORETICAL APPROACH

Generally, tasks in developing CFD programs include derivation of the governing equations, solution of the flow equations, accuracy and stability analysis of the scheme, grid generation, etc. In this section, outline of the theories as used in the CFL3D code will be presented. The grid generation method used in this study will also be discussed.

The program CFL3D utilizes thin-layer Reynolds averaged Navier-Stokes equations, enabling detailed flow properties to be obtained. In solving the governing equations, the program is based on a finite volume approach. In addition, the accuracy of the solution depends on the smoothness of the grids.

In spatially discretizing equations into finite difference forms, central difference is usually used. This formulation ensures a second order accuracy. From the consideration of accuracy, a central difference is better than either the backward or forward difference. However, in some particular situations, backward difference has to be used to satisfy the physics of the flow field. For example, in a supersonic flow region, the Mach lines drawn from a point divide the flow into zones of influence. Properties at this point can only be affected by flow in the zone of influence. Therefore, while formulating differentiation in difference forms, only the points in the zone of influence should be taken into consideration. In this situation, the backward difference scheme has to be used. For subsonic flow, characteristics at each point can be affected by any other points in the flow field. Thus, the central difference scheme is suitable for subsonic flow calculation.

In transonic flow computations, the formulation of the difference equations becomes more difficult due to combination of subsonic and supersonic regions. As stated earlier, in the subsonic region, the central difference scheme should be used. On the other hand, in the supersonic region, backward difference has to be applied. Upwind difference was developed to solve this problem. Take the differentiation $\partial F/\partial \xi$ as an example. The formulation can be written as

$$\frac{\partial F}{\partial \xi} = \mu\left(\frac{F_{i+1} - F_{i-1}}{2\Delta\xi}\right) + (1 - \mu)\left(\frac{F_i - F_{i-1}}{\Delta\xi}\right) \qquad (1)$$

$\mu = 1$ subsonic

$\mu = 0$ supersonic

Therefore, central difference is used in the subsonic region. In a supersonic region, backward difference is used.

In CFL3D, options of central difference with added dissipative terms, flux difference splitting, and flux vector splitting are provided to separate the flow field into regions with different flow characteristics. Details of upwind differencing used in the program will be discussed later. In addition, CFL3D has the capability of multiblock computation. The development of multiblock computation enables CFD to be applied to complicated configurations. Also, this concept makes the grid generation an easier task. For example, an individual block can be formed in the region where smooth continuation of the grids is not possible.

Therefore, smooth grids can be constructed in each block. Flow properties can also be solved accurately in each block. Transmission of flow characteristics among blocks can be achieved through interpolations.

2.1 Governing Equations

From the conservation of mass, momentum, and energy, the Navier-Stokes equations can be written as

$$\frac{\partial Q}{\partial t} + \frac{\partial}{\partial x}(F - F_v) + \frac{\partial}{\partial y}(G - G_v) + \frac{\partial}{\partial z}(H - H_v) = 0 \qquad (2)$$

where

$$Q = \begin{pmatrix} \rho \\ \rho u \\ \rho v \\ \rho w \\ e \end{pmatrix}$$

Flux in the x-direction:

$$F = \begin{pmatrix} \rho u \\ \rho u^2 + p \\ \rho uv \\ \rho uw \\ (e + p)u \end{pmatrix} \qquad F_v = \begin{pmatrix} 0 \\ \tau_{xx} \\ \tau_{xy} \\ \tau_{xz} \\ u\tau_{xx} + v\tau_{xy} + w\tau_{xz} - \dot{q}_x \end{pmatrix} \qquad (3)$$

Flux in the y-direction:

$$G = \begin{pmatrix} \rho v \\ \rho uv \\ \rho u^2 + p \\ \rho uw \\ (e + p)v \end{pmatrix} \qquad G_v = \begin{pmatrix} 0 \\ \tau_{xy} \\ \tau_{yy} \\ \tau_{xy} \\ u\tau_{yx} + v\tau_{yy} + w\tau_{yz} - \dot{q}_y \end{pmatrix} \tag{4}$$

Flux in the z-direction:

$$H = \begin{pmatrix} \rho w \\ \rho wu \\ \rho wv \\ \rho w^2 + p \\ (e + p)w \end{pmatrix} \qquad H_v = \begin{pmatrix} 0 \\ \tau_{zx} \\ \tau_{zy} \\ \tau_{zz} \\ u\tau_{zx} + v\tau_{zy} + w\tau_{zz} - \dot{q}_z \end{pmatrix} \tag{5}$$

where e is the total energy per unit volume defined as

$$e = \frac{p}{\gamma - 1} + \frac{1}{2}\rho(u^2 + v^2 + w^2)$$

The shear stress $\tau_{x_i x_j}$ and heat flux $\dot{q}_{x_i}$ are defined as

$$\tau_{x_i x_j} = \frac{M_\infty}{R_e}\left[\mu\left(\frac{\partial u_i}{\partial x_j} + \frac{\partial u_j}{\partial x_i}\right) + \lambda \frac{\partial u_k}{\partial x_k}\delta_{ij}\right]$$

$$\dot{q}_{x_i} = \frac{\gamma}{P_r} k \frac{\partial T}{\partial x}$$

2.2 Coordinate Transformation

Because of the irregular grid spacing in the physical domain (x-, y-, z-coordinates), the order of computational accuracy is difficult to predict. From a scheme-stability point of view, it is better to perform the calculation in a generalized coordinate domain (so-called computational domain). The generalized coordinate transformation can be described as

$$\begin{aligned} \xi &= \xi(x, y, z, t) \\ \eta &= \eta(x, y, x, t) \\ \zeta &= \zeta(x, y, z, t) \end{aligned} \tag{6}$$

The Jacobian of this generalized transformation is obtained as

$$\begin{aligned} J &= \frac{\partial(\xi, \eta, \zeta)}{\partial(x, y, z)} \\ &= [x_\xi(y_\eta z_\zeta - y_\zeta z_\eta) - y_\xi(x_\eta z_\tau - x_\zeta z_\eta) + z_\xi(x_\eta y_\zeta - y_\eta x_\zeta)]^{-1} \end{aligned} \tag{7}$$

The governing equation becomes

$$\frac{\partial \hat{Q}}{\partial t} + \frac{\partial}{\partial \xi}(\hat{F} - \hat{F}_v) + \frac{\partial}{\partial \eta}(\hat{G} - \hat{G}_v) + \frac{\partial}{\partial \zeta}(\hat{H} - \hat{H}_v) = 0 \tag{8}$$

where

$$\hat{Q} = Q/J$$

$$\hat{F} - \hat{F}_v = \frac{|\nabla\xi|}{J}\left[\xi_x(F - F_v) + \xi_y(G - G_v) + \xi_z(H - H_v) + \xi Q\right]$$

$$\hat{G} - \hat{G}_v = \frac{|\nabla\eta|}{J}\left[\eta_x(F - F_v) + \eta_y(G - G_v) + \eta_z(H - H_v) + \eta_t Q\right]$$

$$\hat{H} - \hat{H}_v = \frac{|\nabla\xi|}{J}\left[\zeta_x(F - F_v) + \zeta_y(G - G_v) + \zeta_z(h - H_v) + \zeta_t Q\right]$$

$$(\hat{K}_x, \hat{K}_y, \hat{K}_z, \hat{K}_t) = (K_x, K_y, K_z, K_t)/|\nabla K|$$

$$|\nabla K| = (K_x^2 + K_y^2 + K_z^2)^{1/2}$$

$$\bar{u} = (\xi_x u + \xi_y v + \xi_z w)/|\nabla K|$$

$$\bar{v} = (\eta_x u + \eta_y v + \eta_z w)/|\nabla K|$$

$$\bar{w} = (\zeta_x u + \zeta_y v + \zeta_z w)/|\nabla K|$$

$$K = (\xi, \eta, \zeta), \text{ respectively} \qquad \textbf{(9)}$$

The derivation of Equation (9) can be found in Appendix A.

2.3 Thin-Layer Navier-Stokes Approximation

It is known that the velocity and pressure vary rapidly near a solid surface in the direction normal to the surface. On the other hand, flow characteristics are generally smooth along the surface, unless singularities exist. Retaining only the viscous gradient terms corresponding to the direction normal to the surface can save computing resources, yet maintain enough computational accuracy. In this manner, the thin-layer Navier-Stokes equations can be obtained as

$$\frac{\partial \hat{Q}}{\partial t} + \frac{\partial}{\partial \xi}(\hat{F}) + \frac{\partial}{\partial \eta}(\hat{G}) + \frac{\partial}{\partial \zeta}(\hat{H} - \hat{H}_v) = 0 \qquad \textbf{(10)}$$

Certainly, viscous gradient terms can also be retained in the ξ, and η directions because, in CFL3D, solid surfaces can be placed on any block surfaces. The laminar viscous terms can be included in all ξ, η, ζ directions simultaneously. However, turbulence viscous terms can only be added at most in two directions simultaneously.

It should be noted that the turbulent equations are derived with a time-averaging procedure. By decomposing every flow variable into the sum of average value and fluctuation, such as $u_i = \bar{u}_i + u_i'$, time-averaging of momentum equations would produce unknown terms such as $\bar{\rho}\,\overline{u_i' u_j'}$. These new unknowns

(called Reynolds stresses) need to be specified to close the system of equations in a technique called turbulence modeling. In the present application, turbulence modeling is accomplished by an algebraic method in which these Reynolds stresses are specified in a form similar to the viscous terms. As a result, the final form of the equations to be solved is the same as Eq. (10) except that the coefficient of viscosity (μ) is to be replaced by $\mu + \varepsilon$, where ε is the eddy viscosity. In Section 2.8, the way ε is calculated will be summarized.

2.4 Approximate Factorization

The thin-layer Reynolds-averaged Navier-Stokes equations are solved by three-factor approximate factorizations. For example, at time step n + 1, Equation (10) can be written as

$$[\frac{I}{J\Delta t} + \delta_\xi \frac{\partial \hat{F}}{\partial Q} + \delta_\eta \frac{\partial \hat{G}}{\partial Q} + \delta_\zeta(\frac{\partial \hat{H}}{\partial Q} - \frac{\partial \hat{H}_v}{\partial Q})]^n \Delta Q = -R^n \qquad (11)$$

where R^n is the residual. Equation (11) can be factorized into three equations along ξ, η, ζ sweep directions as follows:

$$[\frac{I}{J\Delta t} + \delta_\xi \frac{\partial \hat{F}}{\partial Q}]^n [I + J\Delta t \delta_\eta \frac{\partial \hat{G}}{\partial Q}]^n [I + J\Delta t \delta_\zeta(\frac{\partial \hat{H}}{\partial Q} - \frac{\partial \hat{H}_v}{\partial Q})]^n = -R^n$$

$$[\frac{I}{J\Delta t} + \delta_\xi \frac{\partial \hat{F}}{\partial Q}]^n \Delta Q^* = -R^n \qquad (12)$$

$$[\frac{I}{J\Delta t} + \delta_\eta \frac{\partial \hat{G}}{\partial Q}]^n \Delta Q^{**} = (\frac{I}{J\Delta t})\Delta Q^* \tag{13}$$

$$[\frac{I}{J\Delta t} + \delta_\zeta(\frac{\partial \hat{H}}{\partial Q} - \frac{\partial \hat{H}_v}{\partial Q})]^n \Delta Q = (\frac{I}{J\Delta t})\Delta Q^{**} \tag{14}$$

The solution is then updated as

$$Q^{n+1} = Q^n + \Delta Q \tag{15}$$

2.5 Upwind Differencing Scheme

Three distinct upwind difference schemes are provided in this program; e.g., flux difference splitting, flux vector splitting, and central difference with explicit artificial damping. The central difference scheme used in this program is the same as that used in Reference 36 by adding the negative of the following explicit dissipative term to the governing equations:

$$Dq_{ijk} = D_x q_{ijk} + D_y q_{ijk} + D_z q_{ijk} \tag{16}$$

$$\begin{aligned} D_x q_{ijk} &= d_{i+1/2,j,k} - d_{i-1/2,j,k} \\ D_y q_{ijk} &= d_{i,j+1/2,k} - d_{i,j-1/2,k} \\ D_z q_{ijk} &= d_{i,j,k+1/2} - d_{i,j,k-1/2} \end{aligned} \tag{17}$$

$$d_{i+1/2,i,k} = \frac{J_{i+1/2,j,k}}{\Delta \bar{t}}[\varepsilon^{(2)}_{i+1/2,j,k}(q_{i+1,j,k} - q_{i,j,k}) - \varepsilon^{(4)}_{i+1/2,j,k}(q_{i+2,j,k} - 3q_{i+1,j,k} + 3q_{ijk} - q_{i-1,j,k}] \quad (18)$$

Define

$$\nu_{ijk} = \frac{|\bar{P}_{i+1,j,k} - 2\bar{P}_{ijk} + \bar{P}_{i-1,j,k}|}{|\bar{P}_{i+1,j,k} + 2\bar{P}_{ijk} + \bar{P}_{i-1,j,k}|} \quad (19)$$

$$\varepsilon^{(2)}_{i+1/2,j,k} = k^{(2)}\max(\nu_{i+1,j,k}, \nu_{ijk}) \quad (20)$$

$$\varepsilon^{(4)}_{i+1/2,j,k} = \max[0,(k^{(4)} - \varepsilon^{(2)}_{i+1/2,j,k})] \quad (21)$$

where $k^{(2)}$ and $k^{(4)}$ are artificial damping coefficients. Typically, values of $k^{(2)}$ and $k^{(4)}$ are 1/4 and 1/256, respectively.

In Equation (20), the artificial damping sensor υ_{ijk} is used to sense the existence of shock waves. Theoretically, the pressure distribution is smooth in the flow field if no shock waves exist. Therefore, υ_{ijk} is close to zero. The central difference is used in this situation. If a shock occurs in the flow field, the pressure rises across the shock. The sensor has a value close to one; thus, backward difference becomes the dominant term.

The schemes of flux difference and flux vector splittings are summarized below.

2.5.1 Flux Difference Splitting: The generalized fluxes F, G, and H are split into forward and backward contributions according to the signs of eigenvalues of the Jacobian matrices. Eigenvalues of the Jacobian matrices determine the direction of the propagation waves. If an eigenvalue of the matrix is positive, the wave corresponding to this eigenvalue is moving toward the positive direction. Therefore, backward difference should be used. Otherwise, if the eigenvalue is negative, forward difference should be used. For example, consider the flux in the ξ direction,

$$A = \frac{\partial \hat{F}}{\partial Q} = T\Lambda T^{-1} = T(\Lambda^{+} + \Lambda^{-})T^{-1} \tag{22}$$

where $\Lambda^{\pm} = \frac{\lambda \pm |\lambda|}{2}$, Λ are diagonal matrices formed from the eigenvalues of A.

The left-hand side of Equation (13) can be expressed as

$$[\frac{I}{J\Delta t} + \delta_{\xi} \frac{\partial \hat{F}}{\partial Q}]^{n} \Delta Q^{*} \approx T[\frac{I}{J\Delta t} + \delta_{\xi}^{-}\Lambda^{+} + \delta_{\xi}^{+}\Lambda^{-}]T^{-1}\Delta Q^{*} \tag{23}$$

In the same manner, the flux in the η- and ζ-directions can be split accordingly.

2.5.2 Flux Vector Splitting: The generalized fluxes $\hat{F}$, $\hat{G}$, and $\hat{H}$ are split into forward and backward contributions according to the ratio of flow speed and speed of sound.

For example, consider the flux in the ξ-direction in Equation (10):

$$\delta_\xi \hat{F} = \delta_\xi^- \hat{F}^+ + \delta_\xi^+ \hat{F}^- \tag{24}$$

where δ_ξ^- and δ_ξ^+ denote the backward and forward differences.

Define:

$$M_\xi = \bar{u}/a \quad \text{and} \quad \bar{u} = u/|\nabla\xi| \tag{25}$$

for supersonic flow $(|M_\xi| \geq 1)$

$$\begin{aligned} \hat{F}^+ &= \hat{F},\ \hat{F}^- = 0,\ M_\xi \geq 1 \\ \hat{F}^+ &= 0,\ \hat{F}^- = \hat{F},\ M_\xi \leq -1 \end{aligned} \tag{26}$$

and for subsonic flow $(|M_\xi| < 1)$

$$\hat{F}^{\pm} = \frac{|\nabla\xi|}{J}\begin{bmatrix} f^{\pm}_{mass} \\ f^{\pm}_{mass}[\hat{k}_x(-\bar{u} \pm 2a)/\gamma + u] \\ f^{\pm}_{mass}[\hat{k}_y(-\bar{u} \pm 2a)/\gamma + v] \\ f^{\pm}_{mass}[\hat{k}_z(-\bar{u} \pm 2a)/\gamma + w] \\ f^{\pm}_{energy} \end{bmatrix}$$

$$f^{\pm}_{mass} = \pm\rho a(M_\xi \pm 1)^2/4 \qquad (M_\xi = \frac{\bar{u}}{a})$$

$$f^{\pm}_{energy} = f^{\pm}_{mass}\{[-(\gamma-1)\bar{u}^2 \pm 2(\gamma-1)\bar{u}a + 2a^2]/(\gamma^2+1) + (u^2+v^2+w^2)/2\} \qquad (27)$$

$$\hat{k}_x = \xi_x/|\nabla\xi|,\ \hat{k}_y = \xi_y/|\nabla\xi|,\ k_z = \xi_z/|\nabla\xi|$$

The flux in the η- and ζ-directions can be obtained in the same manner. Derivation of the flux vector splitting formulation can be found in Appendix B. The split-flux difference is implemented as a flux balance across a cell as

$$\delta_\xi \hat{F} = \delta^-_\xi \hat{F}^+ + \delta^+_\xi \hat{F}^- \qquad (28)$$

Since $\Delta\xi = \Delta\eta = \Delta\zeta = 1$, the split-flux difference can be written as

$$\delta_\xi \hat{F} = [\hat{F}^+(Q^-)_{i+\frac{1}{2}} - \hat{F}^+(Q^-)_{i-\frac{1}{2}}] + [\hat{F}^-(Q^+)_{i+\frac{1}{2}} - \hat{F}^-(Q^+)_{i-\frac{1}{2}}] \quad (29)$$

Q is evaluated at cell interface by upwind-biased interpolation.

$$Q^-_{i+\frac{1}{2}} = Q_i + \frac{1}{4}\phi_\xi[(1 - k_\xi)\nabla_\xi + (1 + k_\xi)\Delta_\xi]Q_i \quad (30)$$

$$Q^+_{i+\frac{1}{2}} = Q_{i+1} - \frac{1}{4}\phi_\xi[(1 + k_\xi)\nabla_\xi + (1 - k_\xi)\Delta_\xi]Q_{i+1} \quad (31)$$

where

$$\Delta_\xi Q_i = Q_{i+1} - Q_i \qquad \nabla_\xi Q_i = Q_i - Q_{i-1}$$

$\phi_\xi = 0$ for the first-order upwind, and

$\phi_\xi = 1$, $k_\xi = -1$ for the second-order upwind, and

$\phi_\xi = 1$, $k_\xi = \frac{1}{3}$ for the third-order upwind.

2.6 Multiblock Operation

Usually, an attempt to generate a single grid for a complicated geometry results in highly skewed grids, which in turn result in inaccurate calculations

(Ref. 38). For example, the grid system of the unwrapping type can only describe a simple configuration, such as wing alone or body alone cases. Applying the same grid system to a wing-body configuration, grid smoothing is needed. Also, this grid system usually produces coarse grids on the fuselage while using the same number of grid points on the wing in the unwrapping direction. For a configuration with integrated nozzles, the single-block calculation (grid generation and flow solver) cannot produce accurate results. Therefore, multiblock algorithms become inevitable in the calculation of complex configurations.

In the multiblock calculation, the computational domain is divided into several hexahedral blocks. Basically, the program solves the thin-layer Navier-Stokes equations in individual blocks. Boundary conditions on boundary surfaces of each block have to be specified. If a boundary surface is designated as a patch surface, provision must be made for communication across this block interface.

Generally, the zonal approach bears a number of advantages. Firstly, it avoids the difficulty of generating three-dimensional grids for different types of configurations with appropriate clustering to capture high-gradient flow parameters (Ref. 38). Secondly, zonal methods allow different types of grid topologies to be used to improve mesh efficiency. Thirdly, flow solvers can be written in a structured manner; that is, solution algorithm remains unchanged with appropriate boundary conditions on the block faces to calculate different configurations.

For global computation, a mechanism to transfer information between neighboring blocks must be constructed. Two kinds of techniques, patched-grids (Ref. 39) and overlapping-grids technique (Ref. 40), have been widely used in multiblock applications. In a patched-grids approach, blocks meet at a common interface. Three types of grid arrangements can be used for patched-grids approach (Ref. 39):

(a) one-to-one matching, in which grid lines match across the interface;

(b) MxN-to-one matching, in which grid lines of a cell face match the outer contour of MxN cell surface; and

(c) arbitrary matching, in which there is no restriction on the grid lines' matching.

In the overlapping-grid approach, an overlapping region is required to provide matching solutions across boundary interface. The requirement of a common interface between blocks places restriction on the grid generation process for the patched-grid approach. For the overlapping-grid approach, a great amount of interpolation in the overlapping region is usually required.

CFL3D uses a grid-block patching algorithm based on generalized coordinates. For example, consider two blocks with a common interface. Suppose the spatial flux into block 1 at the interface is desired. Two of the four data points required to construct the split fluxes at the interface come directly from the block 1 values in cells adjacent to the interface. The other two data points can be

obtained by interpolation of the block 2 data to block 1 ghost cell centers projected from block 1.

On each interface plane, flow properties at each cell center are obtained by interpolating flow properties at cell centers of neighboring cell from adjacent block patch surface. To relate the flow properties of block 2 to the image cell center of block 1, interpolations are needed. The interpolations are accomplished by correlating the cell-center properties in block 2 into a polynomial with constant coefficients. In general, a nonlinear polynomial will be formed; therefore, the Newton method is used to determine the corresponding flow properties of the image plate points projected from block 1.

2.7 Jet Application

In the program CFL3D, eight standard boundary conditions are available. A list of the standard boundary conditions can be found in Appendix C. Special purpose boundary conditions can be added following the multiblock coordinate orientation. In the current work, a jet block has to be formed to simulate nozzle exit conditions. The nozzle exit plane is treated as one boundary surface of the jet block. A special routine has been developed to specify the nozzle exit conditions and include the jet in the computation. On the other boundary surfaces, boundary conditions can be specified as patching or in-/out-flow surfaces.

The nozzle exit conditions are

$$q = \begin{bmatrix} \rho \\ u \\ v \\ w \\ P \end{bmatrix}_{jet} \tag{32}$$

Usually, the nozzle pressure ratio (NPR) is given for a certain test condition. The nozzle exit pressure can then be obtained through the assumption of isentropic expansion:

$$\frac{P_{tj}}{P_j} = (1 + \frac{\gamma - 1}{2} M^2)^{\frac{\gamma}{\gamma-1}} \tag{33}$$

The thrust vectoring angles are determined by the ratios between velocity components u, v, and w. The jet deflection angle in the longitudinal direction, δ, equals $\tan^{-1}$ (w/u); the deflection angle in the lateral direction equals $\tan^{-1}$ (v/u).

The jet boundary conditions in the computation are set up as cell center boundary conditions. This implies that the boundary conditions are specified at the cell centers of the cells adjacent to the boundaries. For example, if the jet is moving to the right-hand side, the centers of the cells on the left-hand side of the nozzle exit plane are specified with the designated nozzle exit conditions. Usually, the jet conditions are assumed to be uniform inside the nozzle. For thrust vectoring computation, the flow region starting from the nozzle exit plane can be computed according to the Navier-Stokes equations.

2.8 Turbulence Model

The effect of turbulence modeling is accounted for through the concept of eddy viscosity. The eddy viscosity is computed by the standard Baldwin-Lomax algebraic turbulence model (Ref. 41):

$$\varepsilon = \frac{\varepsilon_w N_{sw}^2 + \varepsilon_{sw} N_w^2}{N_{sw}^2 + N_w^2} \tag{34}$$

where ε_w and N_w are the eddy viscosity and directed distance from the wall.

In the Baldwin-Lomax two-layer model, the eddy viscosity is given by

$$\varepsilon = \begin{cases} \varepsilon_{inner} & y \leftarrow y_{crossover} \\ \varepsilon_{outer} & y_{crossover} < y \end{cases} \tag{35}$$

where y is the normal distance from the wall and $y_{crossover}$ is the smallest value of y at which values ε_{inner} equals ε_{outer}.

The eddy viscosity of the inner layer is determined by

$$\varepsilon_{inner} = \rho \ell^2 |\omega| \tag{36}$$

where

$$\ell = ky[1 - \exp(y^+/A^+)]$$

$|\omega|$ is the magnitude of the vorticity.

$$|\omega| = \sqrt{\left(\frac{\partial u}{\partial y} - \frac{\partial v}{\partial x}\right)^2 + \left(\frac{\partial v}{\partial z} - \frac{\partial w}{\partial y}\right)^2 + \left(\frac{\partial w}{\partial x} - \frac{\partial u}{\partial z}\right)^2}$$

and

$$y^+ = \frac{\sqrt{\rho_w \tau_w} y}{\mu_w}$$

The eddy viscosity of the outer layer is determined by

$$\varepsilon_{outer} = KC_{cp}F_{wake}F_{KLEB}(y) \tag{37}$$

where K is the Clauser constant, and C_{cp} is another coefficient. The value of F_{wake} is determined by

$$F_{wake} = \min\begin{Bmatrix} Y_{max}F_{max} \\ \text{or} \\ C_{wk}Y_{max}U_{dif}^2/F_{max} \end{Bmatrix} \tag{38}$$

$$F_{max} = \max(y|\omega|[1 - \exp(-y^+/A^+)])$$

$$U_{dif} = \left(\sqrt{u^2 + v^2 + w^2}\right)_{max} - \left(\sqrt{u^2 + v^2 + w^2}\right)_{min}$$

The value of $F_{KLEB}(y)$ is

$$F_{KLEB}(y) = \left[1 + 5.5\left(\frac{C_{KLEB}y}{y_{max}}\right)^6\right]^{-1} \tag{39}$$

The constants used in CFL3D are

$A^+ = 26$

$C_{cp} = 1.6$

$C_{KLEB} = 0.3$

$C_{wk} = 0.25$

$K = 0.4$

$k = 0.018$

2.9 Grid Generation

2.9.1 Surface Grid Generation

If the boundaries of a surface are specified, the coordinates on the surface can be obtained by various interpolation methods. Popular interpolation methods include Lagrange interpolation, Hermite interpolation, spline interpolation, etc. In the EAGLE program (Ref. 34), the Lagrange interpolation is recommended, although other interpolation functions are available.

The general form of one-dimensional (ξ) Lagrange interpolation is

$$\gamma(\xi) = \sum_{n=1}^{N} \phi_n(\frac{\xi}{I})\gamma_n, \quad \phi_n(\frac{\xi}{I}) = \prod_{\ell=1}^{N} \frac{\xi - \xi_\ell}{\xi_n - \xi_\ell} \tag{40}$$

where N is the number of points in the ξ interpolation domain and $\xi \varepsilon [0, \ I]$. For example, for a two-point Lagrange interpolation,

$$\gamma(\xi) = (1 - \frac{\xi}{I})\gamma_1 + \frac{\xi}{I}\gamma_2 \tag{41}$$

The general form of two-dimensional (ξ, η) Lagrange interpolation is

$$\begin{aligned}\gamma(\xi, \eta) = &\sum_{n=1}^{N} \phi_n(\frac{\xi}{I})\gamma(\xi_n,\eta) + \sum_{m=1}^{M} \psi_m(\frac{\eta}{J})\gamma(\xi,\eta_m) \\ &- \sum_{n=1}^{N}\sum_{m=1}^{M} \phi_n(\frac{\xi}{I})\psi_m(\frac{\eta}{J})\gamma(\xi_n, \eta_m)\end{aligned} \tag{42}$$

where

$$\psi_m(\frac{\eta}{J}) = \prod_{\ell=1}^{M} \frac{\eta - \eta_\ell}{\eta_m - \eta_\ell}$$

M is the number of points in the η interpolation domain, and $\eta \varepsilon [0, \ 1]$. From Equation (42), the coordinates of the grid points can be obtained.

2.9.2 Three-Dimensional Grid Generation

2.9.2.1 Algebraic Grid Generation: In a three-dimensional domain (ξ, η, ζ), the interpolation becomes

$$\begin{aligned}\gamma(\xi, \eta, \zeta) &= \sum_{n=1}^{N} \phi_n(\frac{\xi}{I})\gamma(\xi_n, \eta, \zeta) + \sum_{m=1}^{M} \psi_m(\frac{\eta}{J})\gamma(\xi, \eta_m, \zeta) \\ &+ \sum_{t=1}^{T} \theta_t(\frac{\zeta}{K})\gamma(\xi, \eta, \zeta_t) - \sum_{n=1}^{N}\sum_{m=1}^{M} \phi_n(\frac{\zeta}{I})\psi_m(\frac{\eta}{J})\gamma(\xi_n, \eta, \zeta) \\ &- \sum_{n+1}^{N}\sum_{t=1}^{T} \phi_n(\frac{\xi}{I})\theta_t(\frac{\zeta}{k})\gamma(\xi_n, \eta, \zeta_t) - \sum_{m=1}^{M}\sum_{t=1}^{T} \psi_m(\frac{\eta}{J})\theta_t(\frac{\zeta}{k})\gamma(\xi, \eta_m, \zeta_t) \\ &+ \sum_{n=1}^{N}\sum_{m=1}^{M}\sum_{t=1}^{T} \phi_n(\frac{\xi}{I})\psi_m(\frac{\eta}{J})\theta_t(\frac{\zeta}{k})\gamma(\xi_n, \eta_m, \zeta_t)\end{aligned} \tag{43}$$

The grids can be produced by using Equation (43). These are the so-called algebraic grids. Usually this type of grid generation system produces smooth grid coordinates. The main advantages of this algebraic grid generation are simplicity and saving of computing time. From Equation (43) the grids are produced based on the boundary spacing. Therefore, boundary point spacing is critical in this system. For example, in flow calculation the spacing near abruptly changing contour should be small. Therefore, the spacing should be small while specifying the boundary points for surface generation in the EAGLE. In other words, users need good judgement while using the algebraic grid generation system. One way to avoid the disadvantages inherent in using the algebraic grid generation system is to use the elliptic grid generation system.

2.9.2.2 Elliptic Grid Generation: The purposes of elliptic grid generation system are controlling coordinate line distribution, and orthogonality in the field. Elliptic grids can be generated by solving the Poisson equations:

$$\nabla^2 \xi^i = P^i \qquad (i = 1, 2, 3) \tag{44}$$

in which p^i is the control function.

Many types of control functions can be used in Equation (44). Control functions to control spacing, orthogonality, curvature, etc., are all different. For example, functions to control the spacing can be written as

$$p^i = A^i + \frac{r_{\xi_i}}{\gamma}, \quad A^i = -\frac{\gamma_{\xi_i \xi_i}}{\gamma_{\xi_i}} \tag{45}$$

where γ is the arc length of a grid line along the boundary surface.

Detailed formulation of the control functions can be found in Reference 34. In solving the Poisson equations, the algebraic grids obtained from the transfinite interpolation are used for initial guesses. Then iterative procedures are used to solve Equation (44) until satisfactory results are obtained.

3. RESULTS

For the nozzle flow calculation, validation of the computational method will be demonstrated first. Subsequently, several aerodynamic phenomena related to thrust vectoring will be discussed. They are

(1) induced pressure variation on the solid surface,

(2) thrust vectoring effect on expansion and shock waves in the jet,

(3) jet static pressure effect on the thrust vectoring effect, and

(4) thrust vectoring effect on the leading edge vortex.

3.1 Jet Model Validation--a 90-Degree Rectangular Jet

A physical model simulating the vectored jet flow is first employed in this study. Validation of this jet model is necessary before performing the thrust vectoring calculation.

Usually, the process of computational fluid dynamics validation is described from two perspectives: numerical-error validation, and physical-model validation (Ref. 42). Errors associated with the first aspect are time and space discretization, grid refinement and numerical dissipation. To eliminate uncertainty in the numerical validation, a simple configuration in steady flow is preferred. The second aspect of CFD validation is associated with the governing equations and turbulence models. In CFL3D, thin-layer Reynolds-averaged Navier-Stokes equations and Baldwin-Lomax turbulence models are used. The Baldwin-Lomax

turbulence model is mainly developed for a solid surface such as a wing. This model is not appropriate for jet turbulence effect. Therefore, in the first example, a laminar-flow case is used.

An experimental study of a 90-degree rectangular jet in a crossflow was presented in Reference 22. The rectangular jet has an aspect ratio of 0.25. The jet is injected into the crossflow from a flat plate. A test condition with a jet-to-freestream speed ratio (R) = 2.2 is chosen for computation. The jet exit speed in the experiment was 225 ft/sec. With a jet-to-freestream ratio of 2.2, the freestream speed is about 100 ft/sec. The Reynolds number based on the flat plate length is 93600. Because of the low Reynolds number, turbulence effect is not considered in the calculation. As mentioned in the conditions of CFD validation, a simple-configuration with laminar flow is desired. For this rectangular jet, grid skewness is eliminated.

In this calculation, flow conditions are taken to be

$M_\infty = 0.1$

$\alpha = 0$

$U_{jet} = 0$

$V_{jet} = 0$

$W_{jet} = 2.2\ M_\infty$

$P_{jet} = P_{inf}$

Velocity vectors shown in Figure 1 are the calculated velocity components slightly away from the flat plate (at cell centers of the cells adjacent to the flat

plate). It is seen that the incoming flow slows down as it approaches the jet. The jet boundary acts like a solid body placed in the crossflow. This blockage effect causes the incoming flow to travel around the jet. The divided external flows eventually merge behind the jet region. As a result of flow merging, circulations occur in this region. Pressure distribution on the flat plate is shown in Figure 2. When the flow approaches the jet, high pressure region is created as a result of flow deceleration. When the flow separates and travels around the jet, flow accelerates on the sides and downstream of the jet. As a result, low pressure regions are created. Pressure distributions from experiment and calculation are presented in Figure 3. As shown in this figure, computed results agree reasonably well with the measurement. Evidently, this jet model used in the computation is capable of simulating the vectored-jet effect.

3.2 Thrust Vectoring Interference on Wing-Body Configuration

An investigation was conducted in the Langley 16-foot transonic tunnel to determine the induced lift characteristics of the vectored-thrust concept in which a rectangular jet-exhaust nozzle was located in the fuselage at the wing trailing edge. A sketch showing the external geometry of the model is presented in Figure 4. The wing has a leading-edge sweep of 50 degrees, streamwise NACA 64A406 airfoil sections, an aspect ratio of 3.0, and a taper ratio of 0.3. The fuselage has rectangular cross sections with rounded corners and had an effective fineness ratio of 7.28. The afterbody boattail angle was 12.5 degrees (Ref. 19). As shown in Figure 5, thrust vectoring was obtained by using circular-arc turning vanes. Also

shown in the same figure, this configuration has a convergent nozzle, which implies that the nozzle exit Mach number can not be greater than unity. For a certain nozzle pressure ratio (NPR), the nozzle exit pressure can be estimated according to the isentropic assumption, providing the jet flow is choked. Difficulties associated with modeling the turning vanes are grid generation, and viscous effect related to the rapid geometric changes. In this study, turning-vane mechanism is not modeled in the calculation. In the simulation of the vectored thrust, instead of having the actual turning vanes, nozzle exit conditions as described in Section 2.7 are used.

Because of the complexity of the geometry, ten blocks are used to model the flow fields around this configuration. Some grid topologies of this configuration are shown in Figure 6. As shown in Figure 5, the top and bottom walls occupy about 15% of the nozzle height. To account for the wall effects, these walls are modeled as solid surfaces. However, the turning vanes and supporting struts, which occupies about 30% of the nozzle exit area, are not included in the calculation. Therefore, total exit area in the computation is about 30% larger than the actual exit area. With the same jet speed and pressure, the mass flow rate in the computation is 30% larger than the actual jet flow rate. A larger jet flow rate might cause the vectored jet effects being overpredicted in the computation.

As shown in Figure 5c, the vane-turning angle (δ_d) is used as one of the test parameters. From measurement (Ref. 19), effective jet-turning angles depend on vane-turning angles as well as thrust coefficients. Figure 7 shows the effective jet-

turning angle under various vane-turning angles and thrust coefficients. In the computation, effective jet-turning angles are used to simulate jet-vectoring effects. Jet total pressure is obtained from Figure 8 at corresponding jet conditions.

Jet conditions used to investigate the jet-induced variation of pressure are as follows:

	M_∞	α	δ_d	M_{jet}	P_{jet}/P_i nf	C_T
1	0.8	3.2°	0°	1.0	1.0	0.06
2	0.8	3.2°	30°	1.0	1.0	0.06

Calculated pressure contours on this configuration are shown in Figures 9 and 10. The upper surface pressure contours are shown in Figure 9. Comparing these two sets of pressure contours, it is seen that the vectored-jet generates lower pressure on the upper surface of the afterbody than the straight jet. Furthermore, a lower pressure region is observed on the wing when the vectored-jet is incorporated. On the other hand, higher pressure regions are generated on the lower surfaces when the vectored-jet is on (Figure 10). Computed pressure distributions on the afterbody are compared with data in Figure 11.

On the upper surface, the predicted pressure distribution shows more rapid changes around the corner of the ramp (x/X = 0.2 to x/X = 0.5). This is most likely affected by not having enough grid points in the boundary layer. When the

number of grid points is increased, the flow simulation is improved (Ref. 43). The calculation also shows the thrust vectoring effects on the ramp. At the region near the exit (x/X = 0.8 to x/X = 1.), a lower pressure distribution is obtained when the jet is vectored. This figure also shows that the vectored jet brings the recovery shock toward the jet.

On the lower surface, the recovery shock is pushed forward by the vectored jet. A higher pressure distribution is also induced. Sectional pressure distributions on the wing are shown in Figure 12. On the wing, higher pressure on the lower surface and lower pressure on the upper surface are induced by the vectored jet. The recovery shock on the upper surface is also moved backwards by the vectored jet.

As mentioned earlier, computational discrepency occurs at the ramp corner region. This region features rapid geometric variation. Expansion waves and flow acceleration are expected. One possible reason for the discrepancy is that the recovery shock waves are not well captured because of insufficient grid resolution in the boundary layer. To correctly predict the shock strength and location, very dense grids and/or adaptive grids are needed. The grid density in the current calculation is not high enough to resolve the boundary layer flow and capture the strong shock waves. A lower Mach number is then used to demonstrate the thrust vectoring calculation. This configuration is calculated under the following conditions

	δ_d	Alpha	Mach	M_{jet}	P_{jet}
1	0°	-0.3°	0.7	1.0	1.0
2	30°	-0.3°	0.7	1.0	1.0

Figure 13 shows the pressure distribution on the center plane of the afterbody. The calculated results agree with the experiments well. Again, the calculation demonstrates the thrust vectoring effects; i.e., lower pressure on the upper surface and higher pressure on the lower surface of the afterbody. Pressure distributions on the wing are shown in Figure 14. Again, a more negative pressure distribution on the upper surface and a more positive pressure distribution on the lower surface are observed. The calculation shows that the vectored-jet induces similar thrust vectoring effects on the wing as well.

3.3 Thrust Vectoring Effect on Shock and Expansion Waves

After the computational method has been verified, some thrust vectoring effects will be elucidated based on computed results. For this purpose, the fuselage-alone configuration of Figure 4, as shown in Figure 15, is used to calculate the thrust vectoring effect on shock and expansion waves. This configuration has rectangular cross sections with rounded corners and has an effective fineness ratio of 7.28. This configuration was calculated under the following jet conditions.

	M_∞	α	δ_d	M_{jet}	P_{jet}/P_{inf}
1	0.9	0°	30°	1.7	1.0
2	0.9	0°	30°	1.7	1.0

Grid topologies of this configuration are shown in Figure 16. For a boattail configuration, flow expansion will occur at the deflecting point. At a transonic speed, if the ramp angle is large enough, a supersonic region will be created by the flow expansion. As the flow travels downstream, it eventually becomes subsonic. A "recovery shock" will occur between the expansion waves and the free stream flow downstream. In this section, thrust-vectoring effects on the expansion waves and the recovery shock will be discussed. The expansion ramp angle of this configuration is 12.5 degrees. With a jet vectored at an angle larger than the ramp deflection angle, the jet shear layer creates a second expansion region. Therefore, a second supersonic region may be present as a result of thrust-induced expansion. Figure 17 shows supersonic regions on this configuration. These regions are indicated by shading. As shown, a supersonic region occurs at the ramp even if the jet is not vectored. But the rest of the region about the nozzle remains subsonic. When the jet is ejected at an angle of 30 degree, not only the ramp region but also the region near the nozzle exit becomes supersonic. This calculation indicates that the flow outside the jet is deflected with the jet. Therefore, another expansion region is created by the thrust-vectoring jet. Figure

18 shows the Mach number distribution along the center line of the upper surface. For the case with the 30-degree jet, the Mach number distribution indicates that supersonic regions exist at the ramp and the jet exit plane. On the other hand, the Mach number distribution for the case with a straight jet shows only a supersonic region at the ramp. The rest of the region remains subsonic. As can be seen, at the region near the jet exit, the flow Mach number is even lower than the freestream mach number ($M < 0.9$ near the exit). Possible reasons for this phenomenon will be discussed in the next section.

3.4 Jet Static-Pressure Effects

Experimental work by Compton (Ref. 44) showed that the exhaust gas physical properties can be related to the jet plume shape and the entrainment and so influence the jet interference on afterbody pressure distribution. When the jet static pressure is greater than the outside pressure, the jet plume boundary will expand (Fig. 19). When the jet boundary expands, plume blockage occurs. Plume blockage can be related to the initial expansion angle of the plume boundary. The angle is the Prandtl-Meyer expansion angle of the jet flow when expanding from its internal exhaust static pressure to the external static pressure at the exit plane. As a result, a Prandtl-Meyer wedged-shaped region will be created at the nozzle edge, and creation of expansion waves is to be expected (Ref. 44). Expansion waves travel across the jet stream and reflect from the free jet boundaries as weak shocks. This wave-reflecting process goes on until viscous effects damp out the flow. With the waves reflecting inside the jet, alternating

high and low pressure regions will be created inside the jet. Two nozzles of NPR = 5 with different jet pressures are calculated to demonstrate the relation between the jet pressure and shock waves contained in the jet stream. The nozzle exit conditions are given in the following table.

	M_∞	α	δ	M_{jet}	P_{jet}/P_{inf}
1	0.8	0°	0°	1.3	1.8
2	0.8	0°	0°	1.7	1.0

Calculated velocity distribution for the first case is illustrated in Figure 20. The pressure and Mach number contours are presented in Figures 21 and 22, respectively. The first case, M_{jet} = 1.3 and P_{jet}/P_{inf} = 1.8, produces strong shock waves inside the jet (Fig. 21a). The pressure contour on the symmetric plane clearly shows the alternation between low- and high-pressure regions. However, for the second jet condition ($P_{jet} = P_{inf}$, Fig. 21b), the pressure contours on the symmetric plane hardly show the shock waves pattern. Figure 22 shows the jet shear layers associated with these two cases. When the jet pressure is high, the jet plume tends to expand at the nozzle exit (Fig. 22a). When the plume blockage occurs, as a result of flow turning and deceleration, pressure distribution on the boattail will rise. As shown in Figure 23, the jet with a higher static pressure also induces higher pressure on the afterbody. These calculated results for straight jets are summarized in Figure 24. These calculations demonstrated the capability

of computing the effect of jet static pressure on flow properties of the shock-containing jet.

Straight jet calculations show that a jet with high static pressure produces larger Prandtl-Meyer expansion and stronger jet-containing shock. As a result of higher jet pressure, the upper surface of the afterbody sustains higher pressure distribution. For the thrust vectoring application, when the jet is deflected downwards, low pressure on the upper surface is desired. However, for a deflected jet, if the upper portion of the jet plumes out, the upper portion of the jet stream does not follow the jet vectored axis. Therefore, the external upper surface flow decelerates and induces a more positive pressure region. To demonstrate the effect of the jet static pressure on the pressure distribution of the afterbody, two cases with the same NPR yet different static pressures are tested. Nozzle exit conditions of these cases are listed below.

	M_∞	α	δ_d	M_{jet}	P_{jet}/P_{inf}
1	0.8	0°	30°	1.3	1.8
2	0.8	0°	30°	1.7	1.0

The computed results are presented in Figures 25-27 for the Mach contours, pressure contours, and pressure distributions on the plane of symmetry, respectively. By comparing Figures 25a and 25b, it is seen that with a higher jet static pressure, flow expansion on the upper surface of the afterbody is much

reduced. This phenomenon can also be seen from the pressure contours shown in Figures 26a and 26b. Figure 27 again indicates that a more negative C_p on the upper surface of the afterbody is obtained with a lower jet static pressure.

To evaluate the aerodynamic performance of these configurations, computed total forces based on the wing reference area are compared as follows:

	C_L	C_D	C_m
$M_{jet} = 1.3$ $P_{jet} = 1.8\ P_{inf}$	0.544	0.067	-0.27
$M_{jet} = 1.7$ $P_{jet} = 1.0\ P_{inf}$	0.55	0.085	-0.28

It is seen that the nozzle with a lower static jet pressure produces a slightly higher lift and more negative pitching moment. However, the drag coefficient is much higher. These calculations demonstrated static pressure effects on the vectored-jet performance.

3.5 Delta Wing with Thrust Vectoring Effect

This section discusses thrust vectoring effects on the leading edge vortices. Various theories of vortex formation have been proposed. Based on presently available results, a simple model (Ref. 46) for vortex formation will be used to explain the computational results. The leading edge vortex can be divided into

two parts: the inner core and the outer core. The inner core is characterized by a high axial velocity, which can reach three times the freestream speed. The outer core is characterized by axial and swirling velocity components that are approximately equal in magnitude. A model for the sequence of events leading to the formation of a leading edge vortex is described as follows.

(1) The leading-edge sweep and pressure difference around the leading edge cause the flow to rotate about a central axis to form a rotating core. This core is called the inner core.

(2) After the inner core is formed, the swirling component of the inner core causes the separated shear layer to wrap around the inner core and form the outer core. For conditions where the vortex breaks down, the inner core diffuses, resulting approximately equal magnitude in the swirling and axial velocity components.

A 63-degree delta wing with a thick base (Fig. 28) is set up to investigate the vectored-jet effect on the leading-edge vortex. In this figure, shaded trapezoids indicate the nozzle exit planes. According to the sequence of leading-edge vortex formation, pressure difference and shear layer viscosity are two important factors. Previous delta wing calculations obtained by the CFL3D show good agreement with experimental data (Ref. 35). For the present configuration, the same grid topology as described in this reference is used. As shown in Figure 29, a block of 60 x 21 x 25 points is constructed for the wing and wake region. A second block of

25 x 17 x 9 points is constructed to fill the space created by the thick base. A patched-grid method is used between these two main blocks.

This configuration was computed under nozzle exit conditions listed below.

	δ_d	M_{jet}	P_{jet}	M_∞	α
1	jet-off	jet-off	jet-off	0.6	25°
2	0°	2	P_{inf}	0.6	25°
3	30°	2	P_{inf}	0.6	25°

As shown in Figures 30-32, because of the thrust vectoring effect, the pressure distributions on the upper surface in all these cases is different in the trailing-edge regions. However, along the leading edge near the apex the pressure distributions are quite similar. Therefore, the vorticity near the apex for all cases is not much affected. As shown in Figure 33, inner core patterns of all cases are similar in the front portion of the vortex cores. However, near the trailing edge, the core with thrust vectoring effect tends to contract. One possible reason for this phenomenon is that the thrust momentum tends to bring the vortex core toward the jet. With the extra flow acceleration, the vortex core has more axial momentum along the streamwise direction. Since the outer core vortex is induced by the inner core swirling velocity, the outer vortex sheets should also be different. As shown in Figure 34, with higher momentum in the axial direction, the vortex

sheets in the case with vectored jet are more organized than the case without thrust vectoring effect.

One way to present the vortex structure is by showing the sectional total pressure contours. For an irrotational flow, the total pressure is constant throughout the flow field. When a vortex flow occurs, the total pressure reduces as the vorticity increases. Because of the vorticity, the inner core bears a lower total pressure distribution compared with other regions. As shown in Figure 35, the vortex under the effect of a vectored jet has lower total pressure in the inner core than the configuration with a straight jet. In other words, a positively vectored jet ($\delta_d > 0°$) can increase the vorticity. As mentioned earlier, the vortex breaks down when the axial and swirling velocity components attain approximately equal magnitude. If the axial velocity decading rate can be reduced, the vortex breakdown can be delayed. The present computation shows that with the induced effect from a vectored jet, the axial velocity of a vortex core in the region near the nozzle can be increased. Thus, it is possible that a vectored jet may delay the occurrence of vortex breakdown.

4. CONCLUSIONS

Aerodynamics induced by thrust vectoring schemes have been studied with a computational method. Specifically, configurations with 2D nozzles were used to investigate the aerodynamic effects related to thrust vectoring operations by thin-layer Reynolds-averaged Navier-Stokes solutions. To simulate the jet stream, jet velocity components and static pressures were specified at the nozzle exit. Two configurations were used in the calculation to verify the code, a rectangular jet in the crossflow, and a wing-body combination with a rectangular nozzle. Calculated results for these two configurations were compared with available data. Additional calculations were performed on a fuselage alone with a rectangular nozzle and a thick delta wing of 63-deg sweep to elucidate the thrust vectoring effects. The results indicated that:

(1) Vectored thrust created a blockage effect in the flow field. A higher pressure region was created in the compression side, and a lower pressure was created in the expansion side.

(2) A vectored jet induced flow expansions and shock waves in the jet at a transonic speed such that thrust vectoring effects were reduced.

(3) A vectored jet induced thrust vectoring effects as shown in (1) on the nozzle as well as on near-by lifting surfaces.

(4) A positively vectored jet made the swirling flow of a leading-edge vortex tighter, i.e., less diffusive.

REFERENCES

1. Hiley, P. E.; Wallace, H. W.; and Booze, D. E. "Study of Non-Axisymmetric Nozzles Installed in Advanced Fighter Aircraft." AIAA Paper 75-1316, Sept. 1975.

2. Berrier, B. L.; and Re, R. J. "A Review of Thrust-Vectoring Schemes for Fighter Aircraft." AIAA Paper 78-1023, July 1978.

3. Capone, F. J. "The Nonaxisymmetric Nozzle--It Is for Real." AIAA Paper 79-1810, Aug. 1979.

4. Nelson, B. D.; and Nicolai, L. M. "Application of Multi-Function Nozzles to Advanced Fighters." AIAA Paper 81-2618, Dec. 1981.

5. Capone, F. J.; and Berrier, B. L. "Investigation of Axisymmetric and Nonaxisymmetric Nozzles Installed on a 0.10-Scale F-18 Prototype Airplane Model." NASA TP-1638, 1980.

6. Herbst, W. B. "Future Fighter Technologies." Journal of Aircraft, Vol. 17, Aug. 1980.

7. Lacey, D. W. "Air Combat Adventures from Reaction Control Systems." SAE Tech. Paper Ser. 801177, Oct. 1980.

8. White, S. N. "Feasibility Study for Integrating Thrust Vectoring as Primary Flight Control System." NASA CR-165758, 1981.

9. Heinz, E.; and Vedova, R. "Requirements, Definition and Preliminary Design for an Axisymmetric Vectoring Nozzle, to Enhance Aircraft Maneuverability." AIAA Paper 84-1212, June 1984.

10. Herrick, P. W. "Propulsion Influences on Air Combat." AIAA Paper 85-1457, July 1985.

11. Gallaway, C. R.; and Osborn, R. F. "Aerodynamics Perspective of Supermaneuverability." AIAA Paper 85-4068, Oct. 1985.

12. Berrier, B. L. "Results from NASA Langley Experimental Studies of Multiaxis Thrust Vectoring Nozzles." SAE Paper 881481, 1989.

13. Siuru, William D., Jr. "Supermaneuverability--Fighter Technology of the Future." Airpower Journal, Vol. 2, spring 1988.

14. Capone, F. J.; and Mason, M. L. "Multiaxis Aircraft Control Power from Thrust Vectoring at high Angles of Attack." AIAA Paper 86-1779, 1986.

15. Brown, H., and Fisk, W. S. "Integrated Flight and Propulsion Operating Modes for Advanced Fighter Engines." ASME Paper 83-1994, March 1983.

16. Banks, D. W.; Quinto, P. F.; and Paulson, J. W. "Thrust-Induced Effects on Low-Speed Aerodynamics of Fighter Aircraft." AIAA Paper 81-2612, Dec. 1981.

17. Lander, J. A.; and Palcza, J. Lawrence. "Exhaust Nozzle Deflector Systems for V/STOL Fighter Aircraft." AIAA Paper 74-1169, Oct. 1974.

18. Henderson, W. P.; and Berrier, B. L. "Airframe/Propulsion Integration Characteristics at Transonic Speeds." NASA CP-3020, Vol. 1, Part 1, April 1988.

19. Capone, F. J. "The Effects on Propulsion-Induced Aerodynamic Forces of Vectoring a Partial-Span Rectangular Jet at Mach Numbers from 0.40 to 1.20." NASA TN D-8039, Dec. 1975.

20. Schetz, J. A.; Jakubowski, A. K.; and Aoyagi, K. "Jet Trajectories and Surface Pressures Induced on a Body of Revolution with Various Dual Jet Configurations." Journal of Aircraft, Vol. 20, Nov. 1983, pp. 975-982.

21. Andreopoulos, J.; and Rodi, W. "Experimental Investigation of Jets in a Crossflow." Journal of Fluid Mechanics, Vol. 138, 1984, pp. 93-127.

22. Kavsaoglu, M. S.; Schetz, J. A.; Jakubowski, A. K. "Rectangular Jets in a Crossflow." Journal of Aircraft, Vol. 26, Sept. 1989, pp.793-804.

23. Sherif, S. A.; Pletcher, R. H. "Measurements of the Flow and Turbulence Characteristics of Round Jets in Crossflow." Journal of Fluids Engineering, Vol. 111, June 1989.

24. Yu, F. M.; Wu, J. M.; Vikili, A. D. "Investigation of Vortical Flow Properties of Jet in a Cross Flow." AIAA Paper 88-0698, Jan. 1988.

25. Perkins, S. C., Jr.; Mendenhall, M. "Computing Jet-Exhaust/Crossflow Interactions." ARC-11597, February 1987.

26. Claus, R. W.; Vanka, S. P. "Multigrid Calculations of a Jet in Crossflow." AIAA Paper 90-0444, Jan. 1990.

27. Needham, D. J.; Riley, N.; Lytton, C. C.; Smith, J. H. B. "A Jet in Crossflow." Journal of Fluid Dynamics, Vol. 221, Feb. 1990.

28. Dormieux, J.; Guillen, P.; Abgrall, R. "Numerical Simulation of Transverse Jet Flows by a Nonreactive Two Species Multidomain Euler Flow Solver." AIAA Paper 90-0126, Jan 1990.

29. Van Dalsem, W. R. "Study of V/STOL Flows Using the Fortifield Navier-Stokes Scheme." Proceedings of the International Symposium, Sydney, Australia, Aug. 1987.

30. Oh, T. S.; Schetz, J. A. "Finite Element Simulation of Jets in a Crossflow with Complex Nozzle Configuration for V/STOL Aircraft." AIAA Paper 88-3269, July 1988.

31. Roth, K. R. "Numerical Simulation of a Subsonic Jet in a Crossflow." SAE Paper 872343, Dec. 1987.

32. Carlson, J. R. "Evaluation and Application of VSAERO to a Nonaxisymmetric Afterbody with Thrust Vectoring." Presented at SAE Aerotech 1987 Conference, Oct. 1987.

33. Compton, W. B., and Abdol-Hamid, K. B. "Navier-Stokes Simulations of Transonic Afterbody Flows with Jet Exhaust." AIAA Paper No. 90- 3057, August 1990.

34. Thompson, J. F. "Numerical Grid Generation System User's Manual." USAF Armament Laboratory Technical Report 87-15, 1987.

35. Thomas, J. L.; Taylor, S.; and Anderson, W. K. "Navier-Stokes Computations of Vortical Flows over Low Aspect Ratio Wings." AIAA Paper 87-0207, 1987.

36. Jameson, A.; Schmidt, W.; and Turkel, E. "Numerical Solutions of the Euler Equations by Finite Volume Methods Using Runge-Kutta Time-Stepping Schemes." AIAA Paper 81-1259, June 1981.

37. Van Leer, B. "Flux-Vector Splitting for the Euler Equations." ICASE Report 82-30, 1982.

38. Arabshahi, A.; Whitfield, D. L. "A Multiblock Approach to Solving the Three-Dimensional Unsteady Euler Equations about a Wing-Pylon-Store Configuration." AIAA Paper 89-3401, 1989.

39. Raj, P.; Keen, J. M.; and Singer, S. W. "Applications of a Euler Aerodynamic Method to Free-Vortex Flow Simulation." AIAA Paper 88-2517, 1988.

40. Benek, J. A.; Buning, P. G.; and Steger, J. L. "A 3-D Chimera Grid Embedding Technique." AIAA 85-1523, 1985.

41. Baldwin, B.; and Lomax, H. "Thin-Layer Approximation and Algebraic Model for Separated Turbulent Flows." AIAA Paper 78-257, Jan. 1978.

42. Marvin, J. G.; and Holst, T. L. "CFD Validation for Aerodynamic Flows--Challenge for the 90's." AIAA Paper 90-2995, 1990.

43. Krist, S. E.; Tseng, J. B.; and Lan, C. E., "Numerical Simulation of Propulsion-Induced Aerodynamic Characteristics on a Wing-Afterbody Configuration with Thrust Vectoring," SAE Paper 911174, April 1991.

44. Compton, W. B. "Effects of Jet Exhaust Gas Properties on Exhaust Simulation and Afterbody Drag." NASA TR R-444, Oct. 1975.

45. Pope, Alan. "Aerodynamics of Supersonic Flight." Pitman Publishing Corp., 1958.

46. Ng, T. T. "On Leading Edge Vortex and Its Control." AIAA Paper 89-3346, 1989.

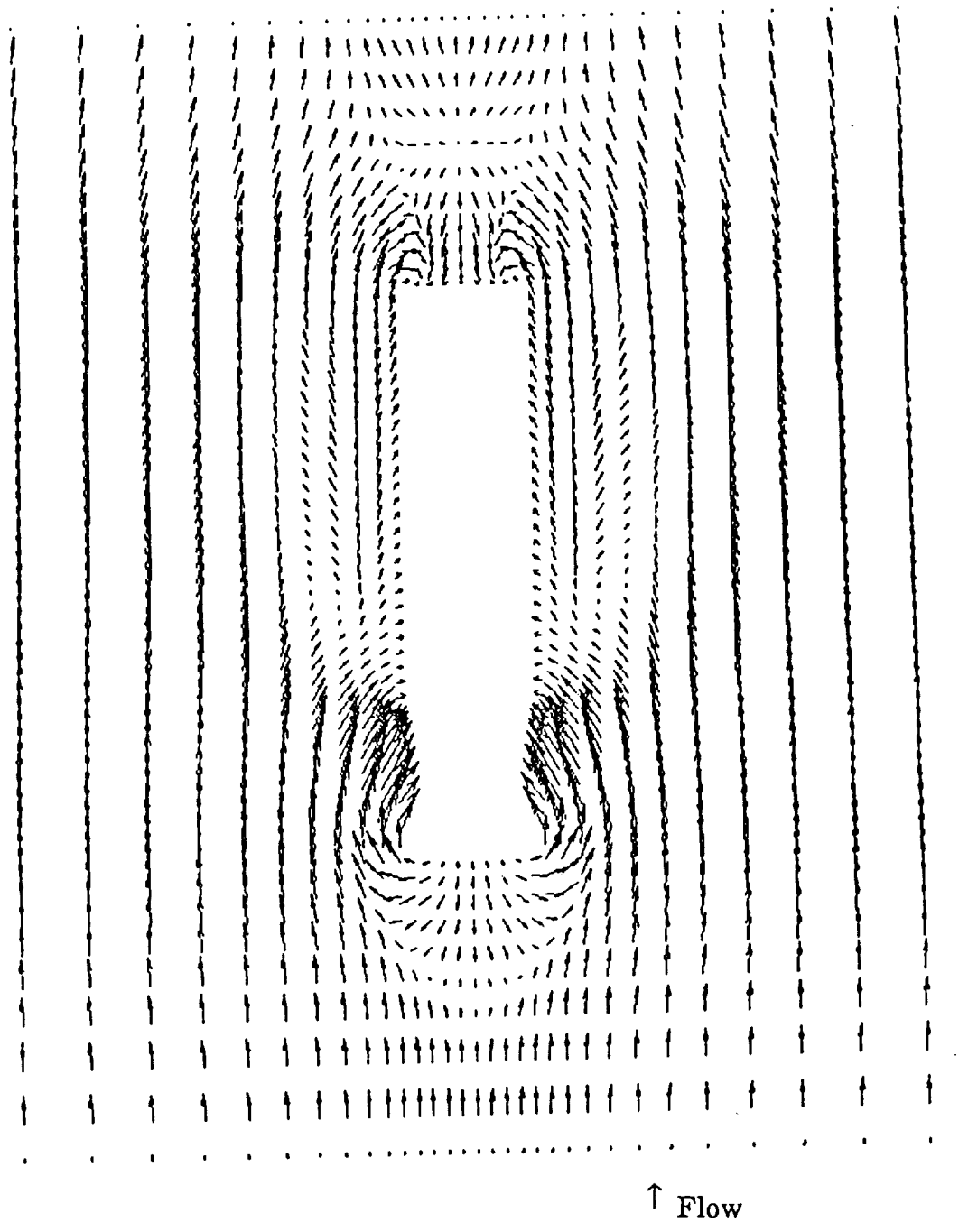

Figure 1 Surface Velocity Vector Plot; 90-Degree Crossjet; R = 2.2.

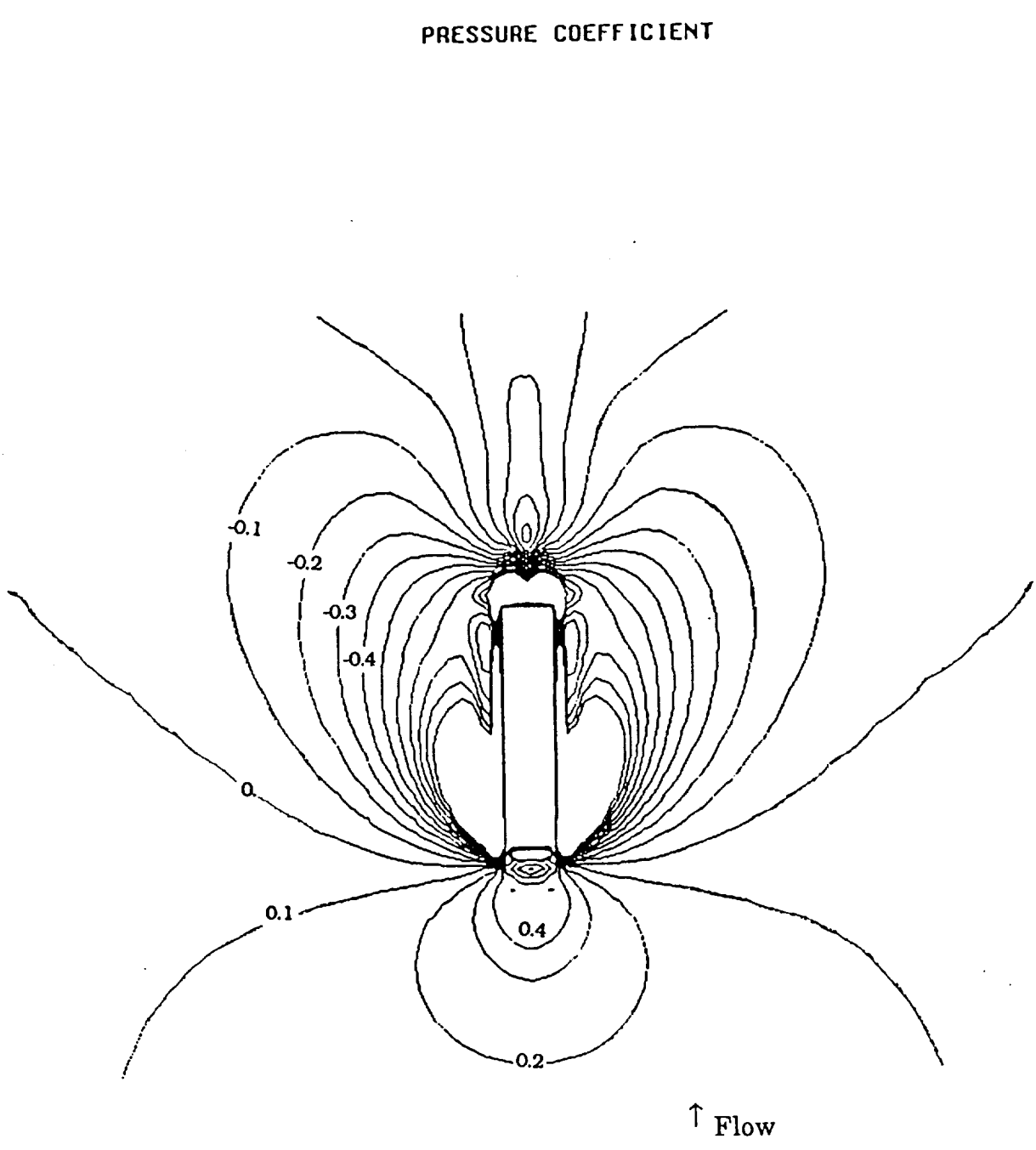

Figure 2 Surface Pressure Contour; 90-Degree Crossjet; R = 2.2.

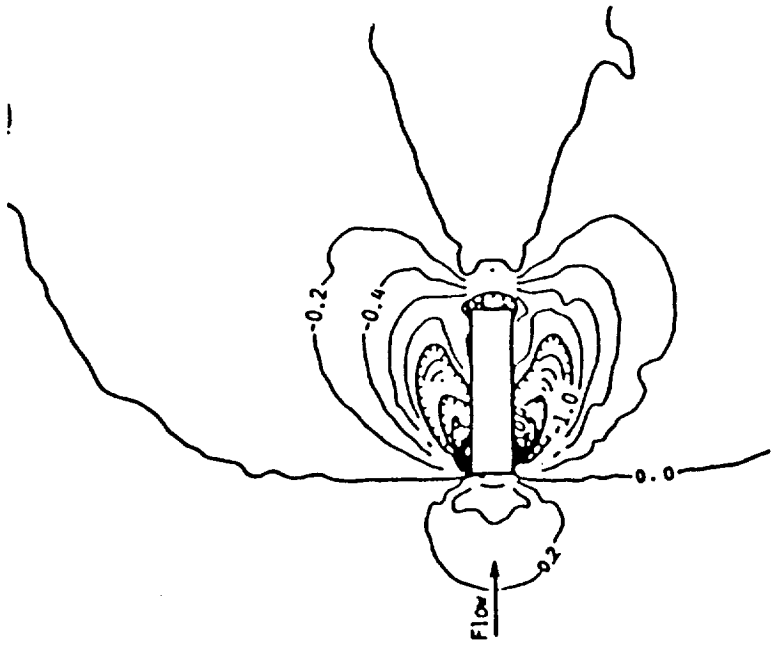

(a) Experiment (Taken from Ref. 22).

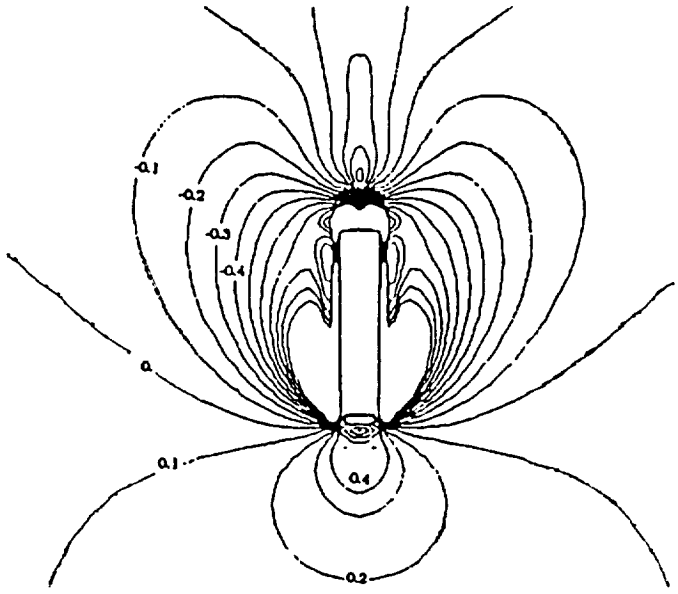

(b) Computation

Figure 3 Surface Pressure Contour Comparison; 90-Degree Crossjet; R = 2.2.

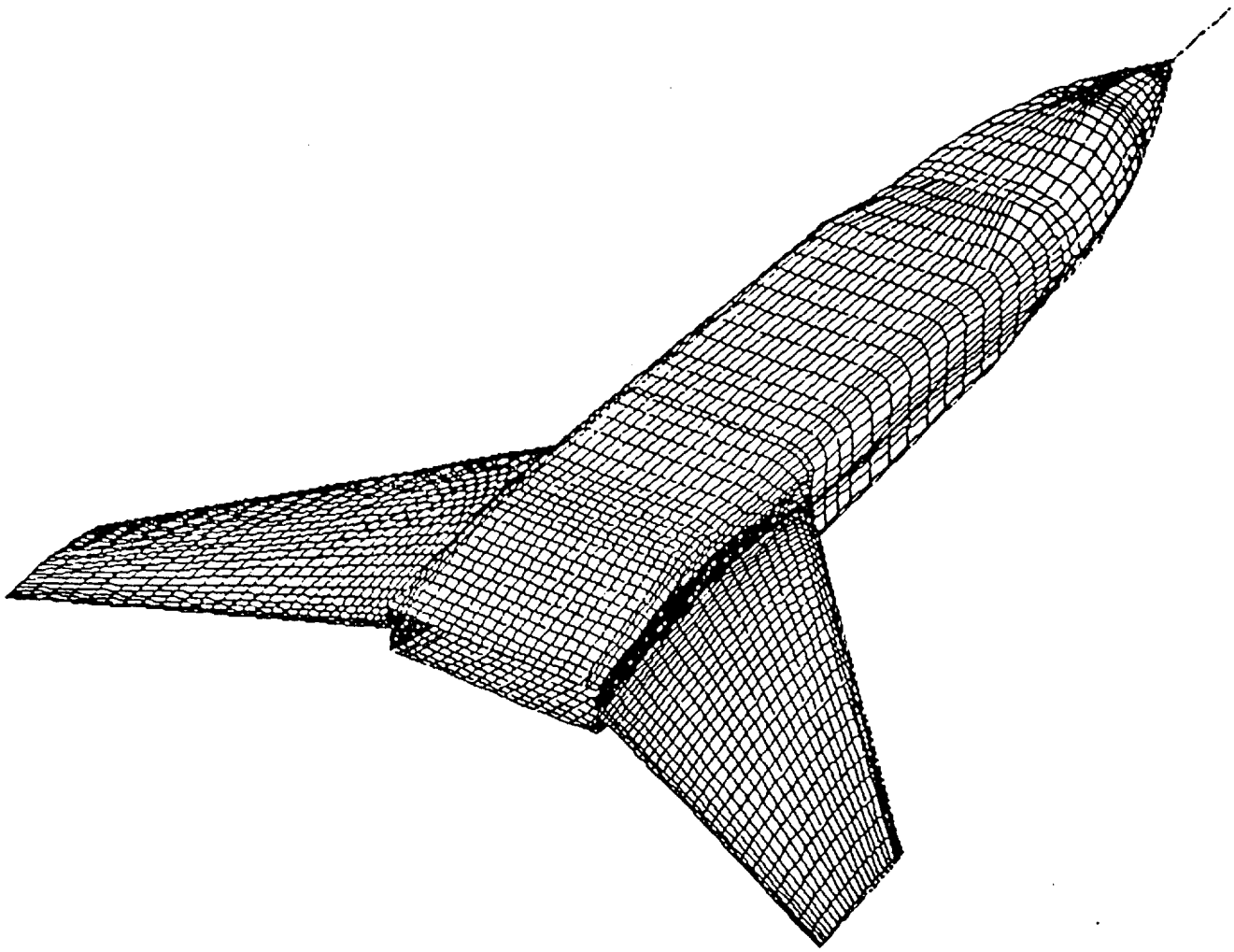

Figure 4 Geometry of the Generic Airplane Configuration.

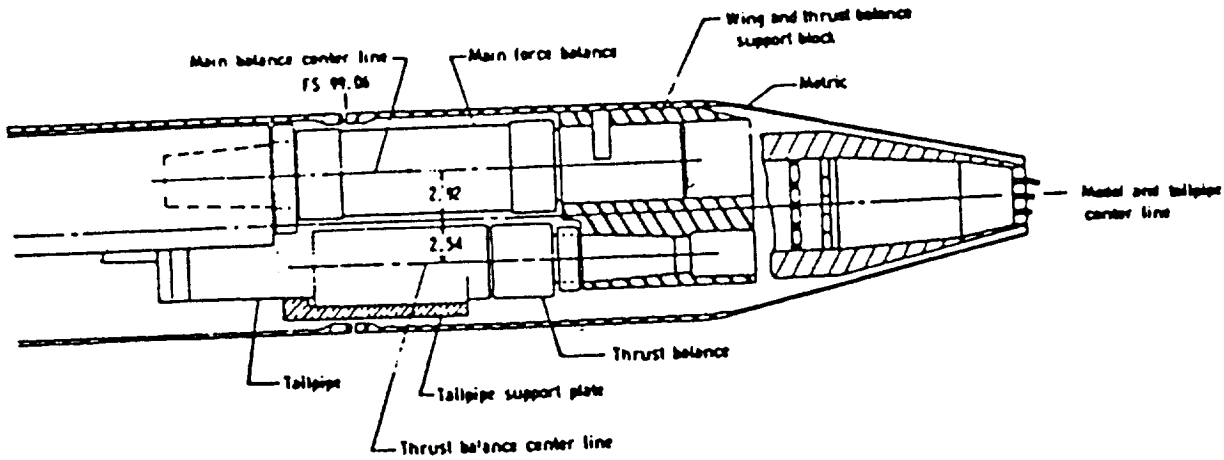

(a) Nozzle Geometry

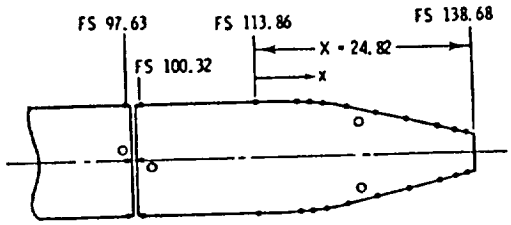

(b) Locations of Pressure Orifices

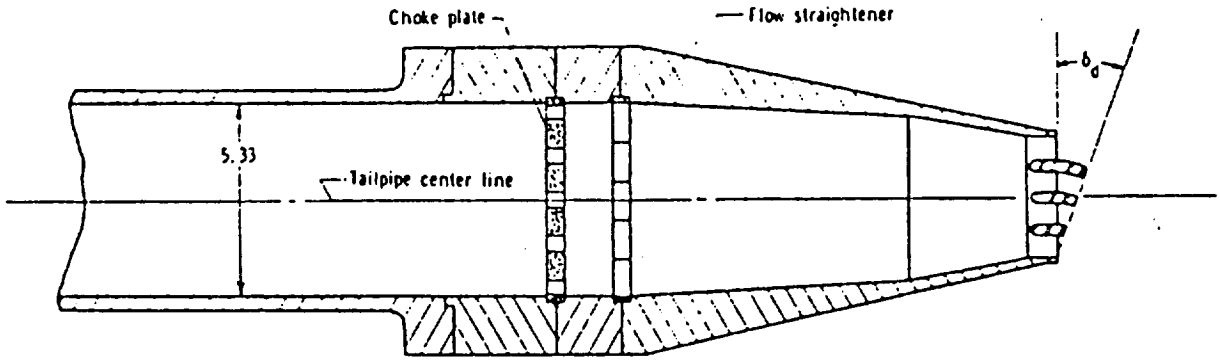

(c) Turning-Vane Geometry

Figure 5 Nozzle and Turning-Vane Equipped in the Generic Airplane Configuration.

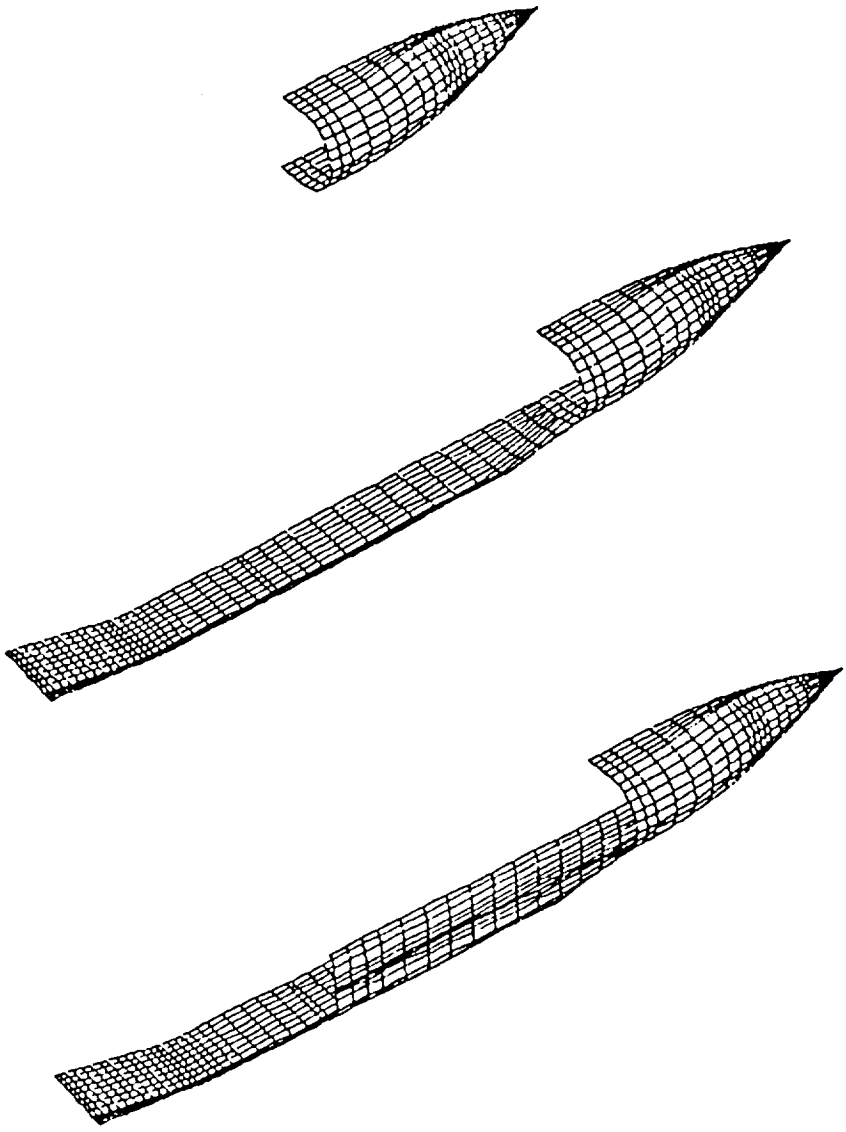

Figure 6 Grid Topologies of the Generic Airplane Calculations.

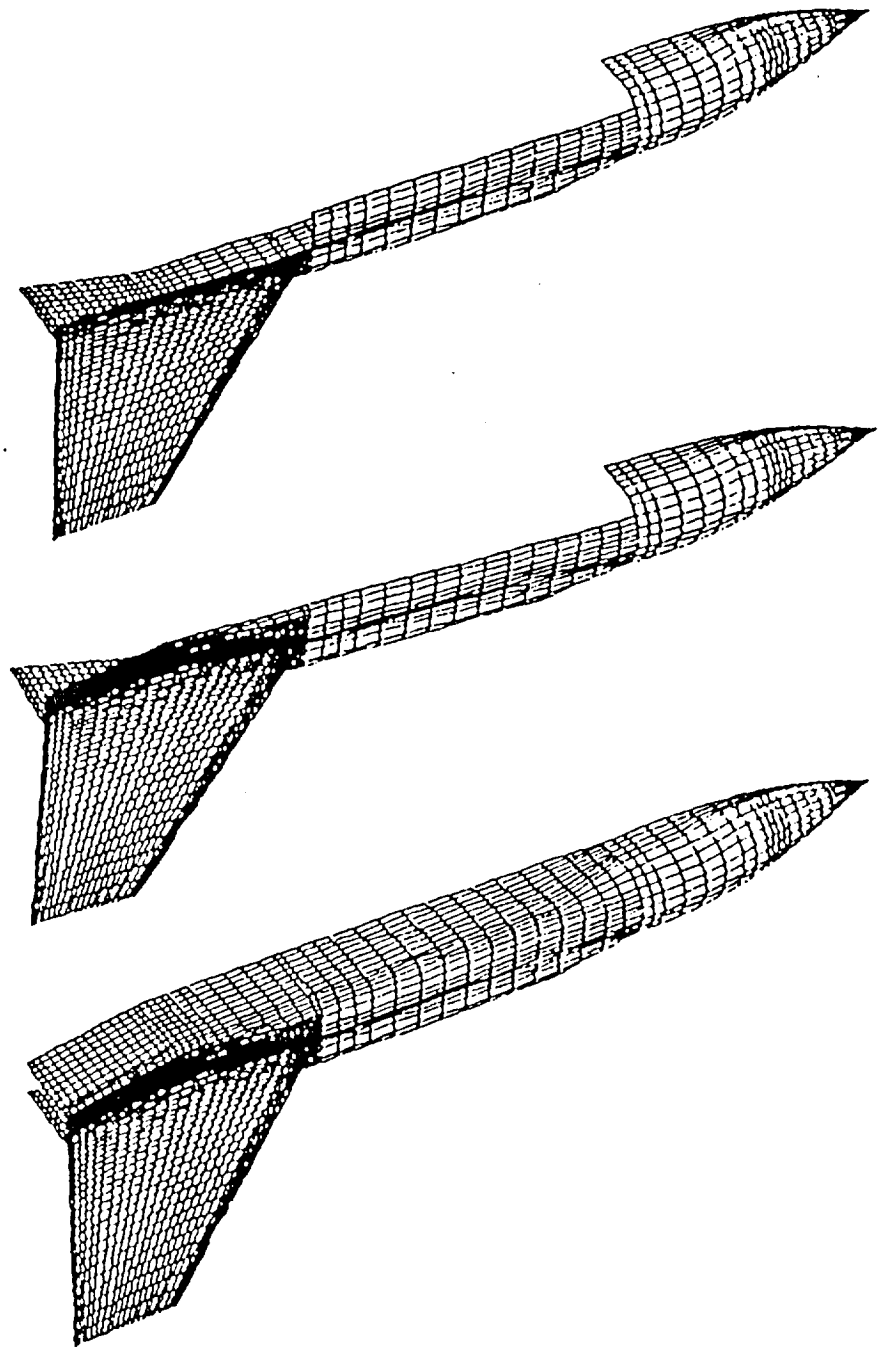

Figure 6 Continued.

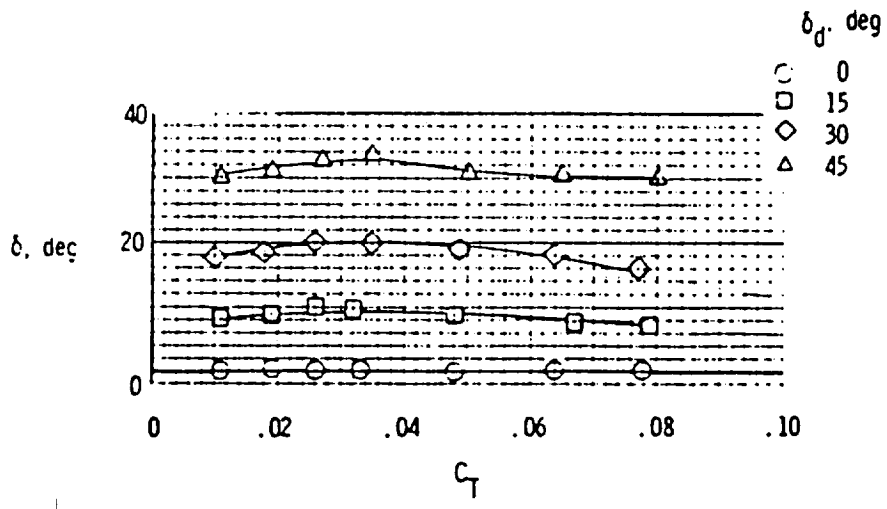

Figure 7 Effective Jet-Turning Angles (Taken from ref. 19).

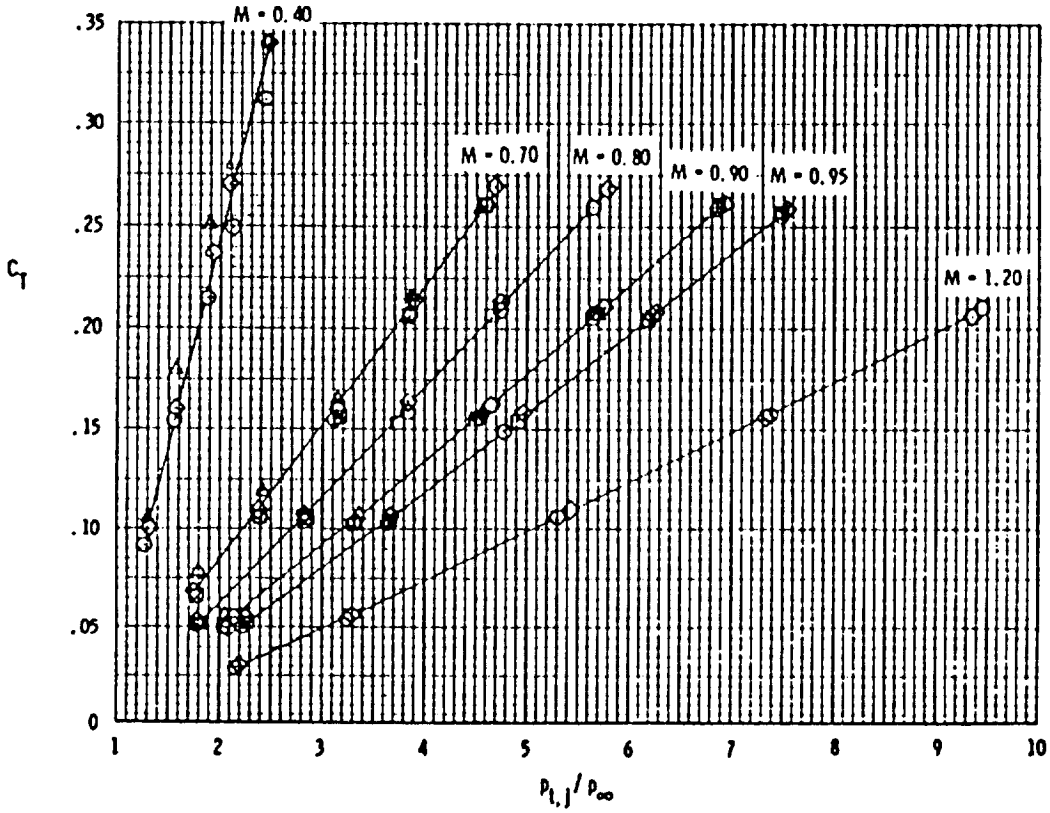

Figure 8 Jet Total Pressure Conversion from Thrust Coefficient (Taken from Ref. 19).

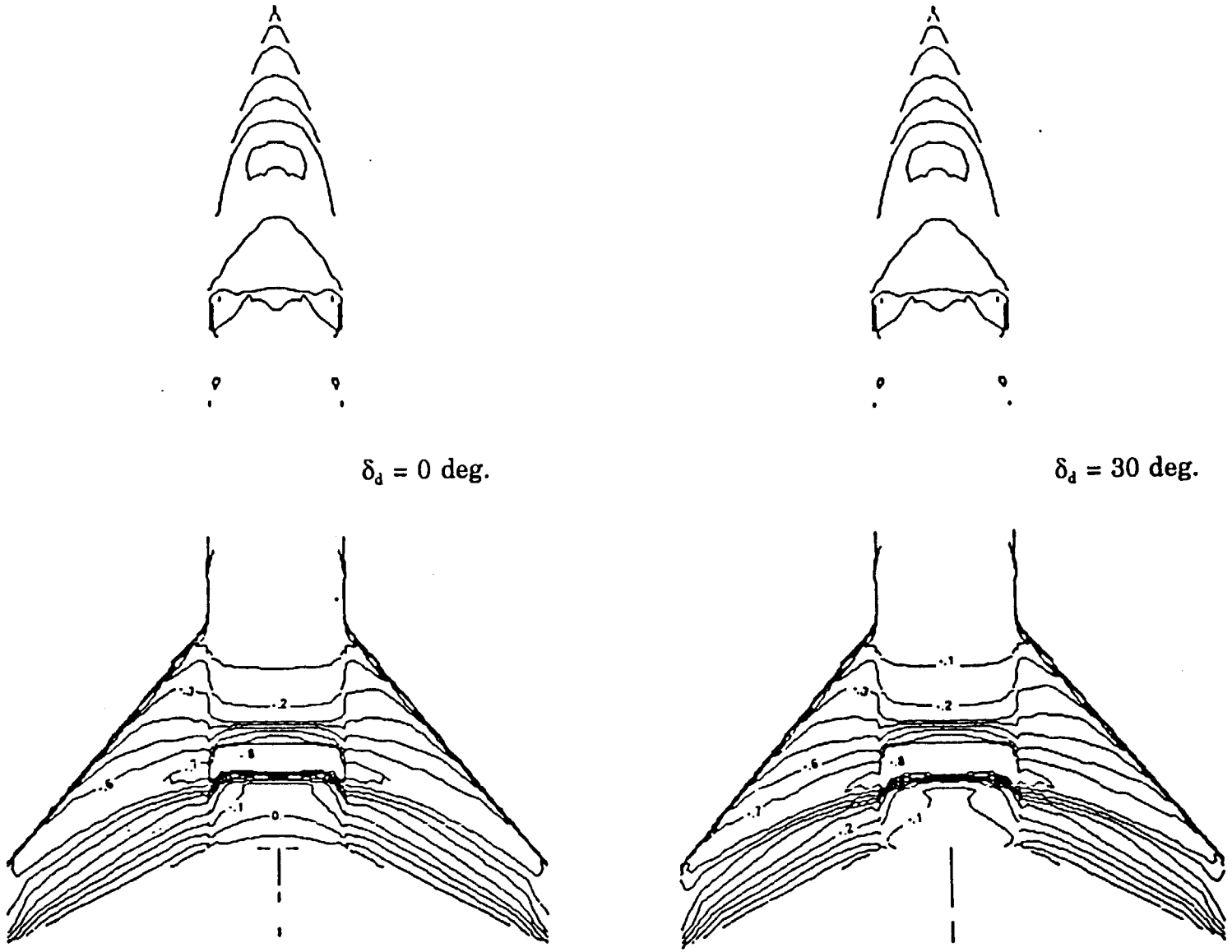

Figure 9 Pressure Contours on the Upper Surface with and without Jet Deflection. C_T = 0.06, M_∞ = 0.8, α = 3.2 deg.

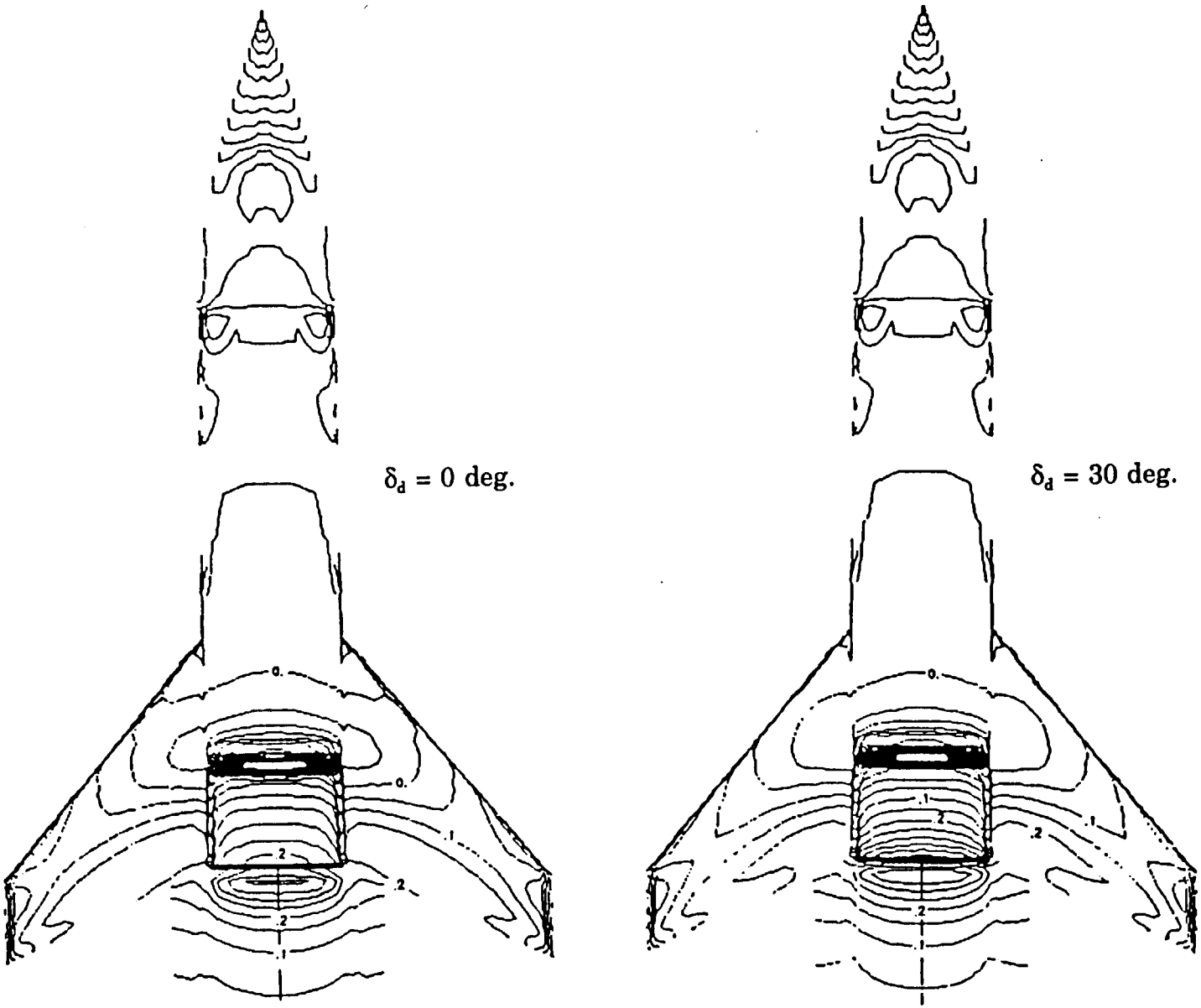

Figure 10 Pressure Contours on the Lower Surface with and without Jet Deflection. C_T = 0.06, M_∞ = 0.8, α = 3.2 deg.

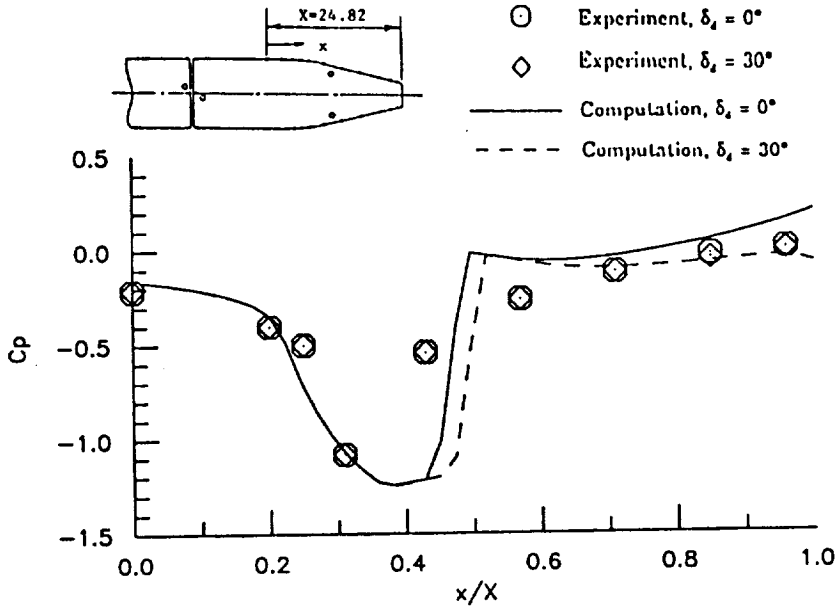

(a) Upper Surface

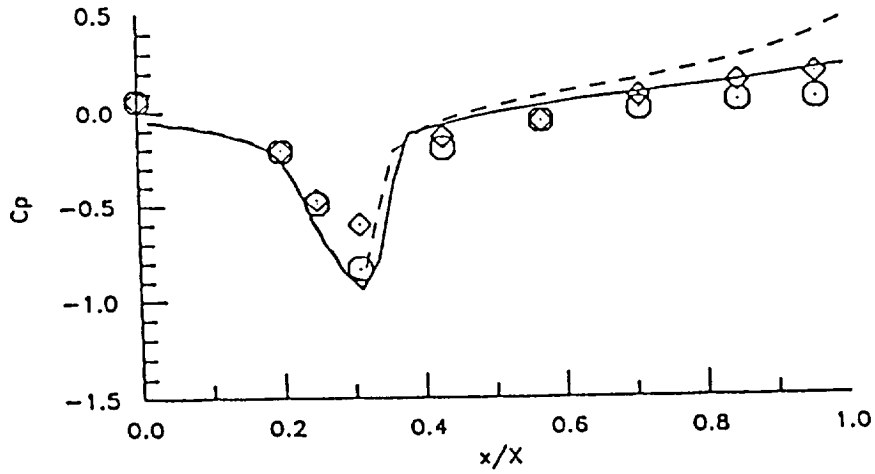

(b) Lower Surface

Figure 11 Sectional Pressure Distributions; 2y/b = 0; M_∞ = 0.8; α = 3.2°; M_{jet} = 1.0; $P_{jet} = P_\infty$.

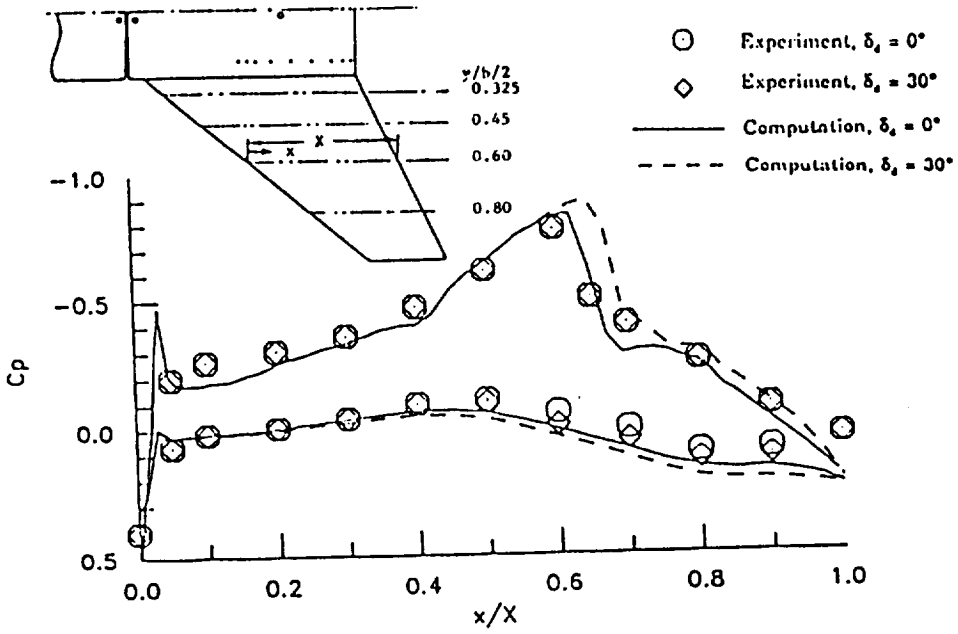

(a) 2y/b = 0.325

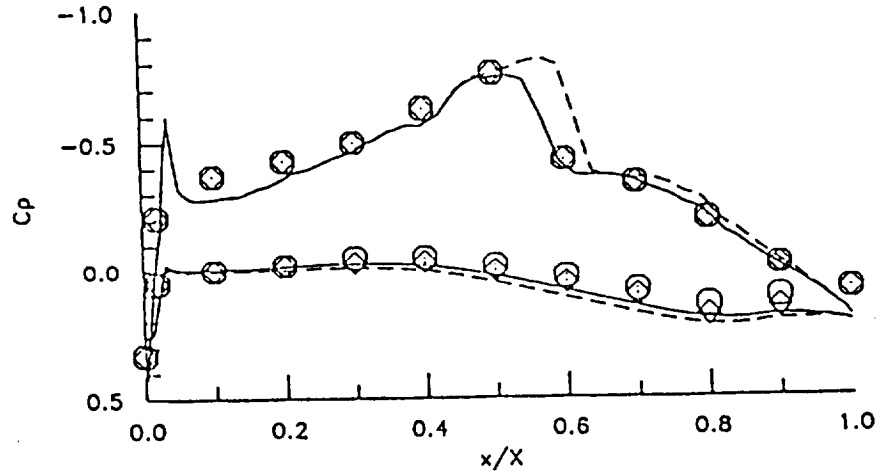

(b) 2y/b = 0.45

Figure 12 Sectional Pressure Distributions on the Wing; $M_\infty = 0.8$; $\alpha = 3.2°$; $M_{jet} = 1.0$; $P_{jet} = P_\infty$.

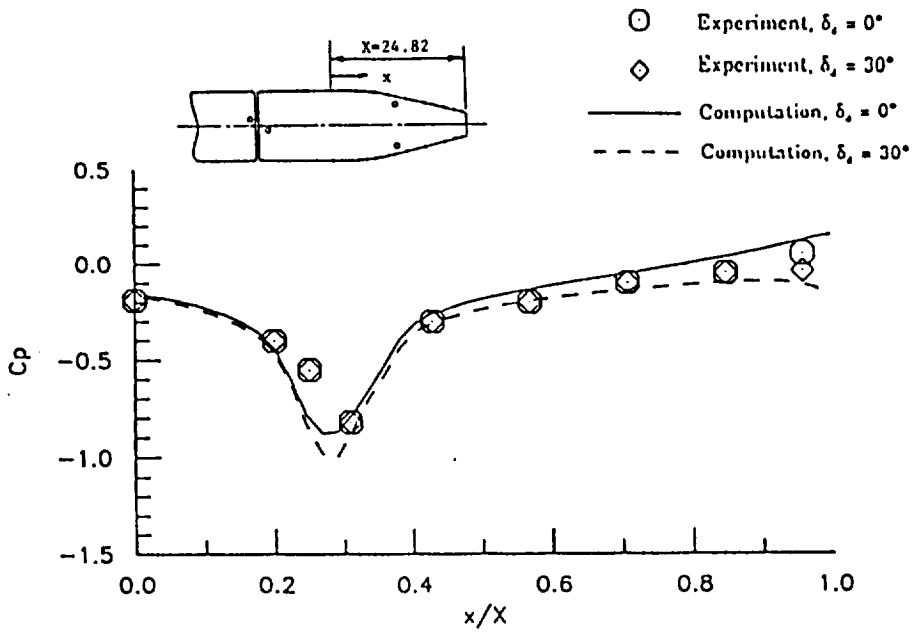

(a) Upper Surface

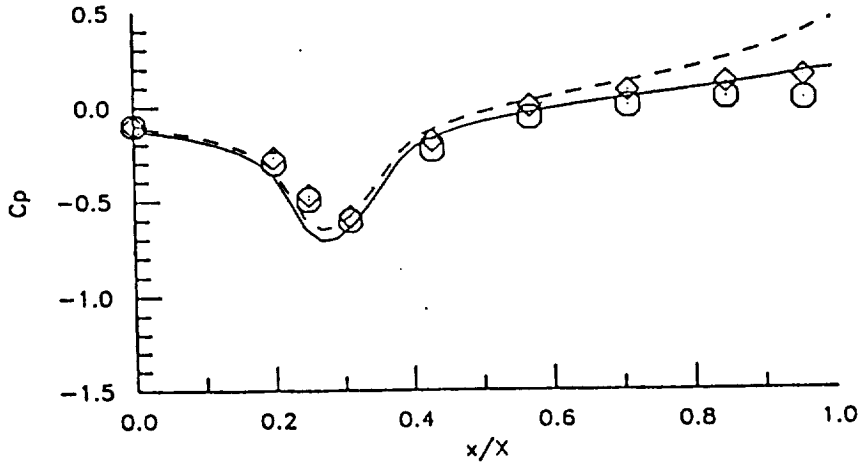

(b) Lower Surface

Figure 13 Sectional Pressure Distributions; 2y/b = 0; M_∞ = 0.7; α = -0.3°; M_{jet} = 1.0; $P_{jet} = P_\infty$.

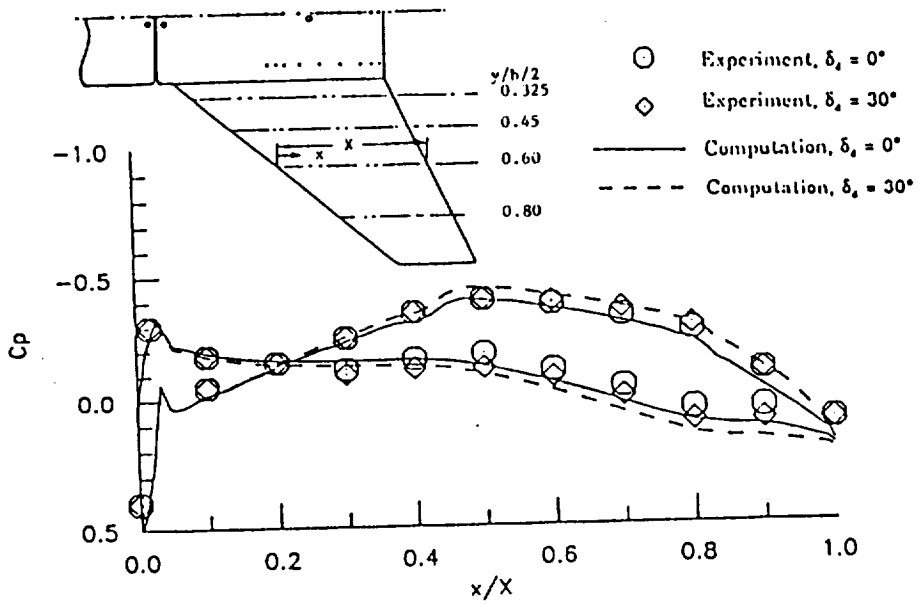

(a) 2y/b = 0.325

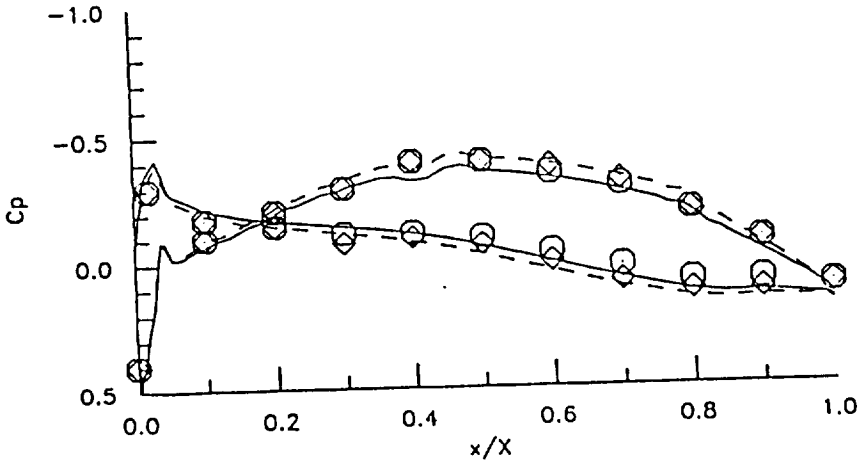

(b) 2y/b = 0.45

Figure 14 Sectional Pressure Distributions on the Wing; $M_\infty = 0.7$; $\alpha = -0.3°$; $M_{jet} = 1.0$; $P_{jet} = P_\infty$.

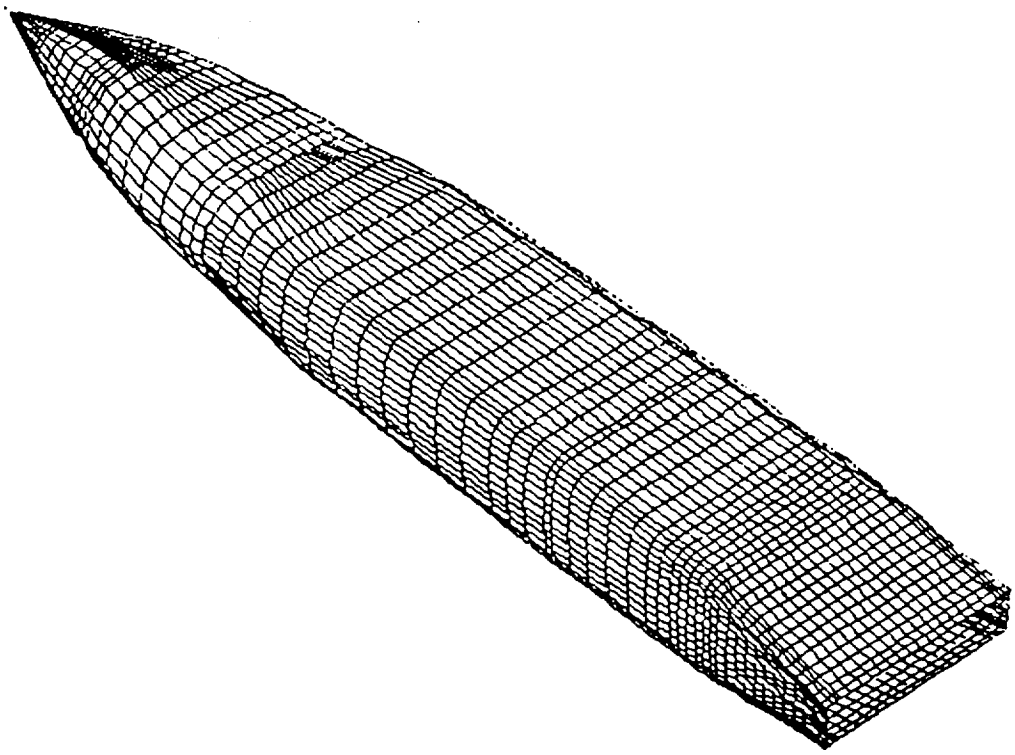

Figure 15 Geometry of a Fuselage with a Rectangular Nozzle.

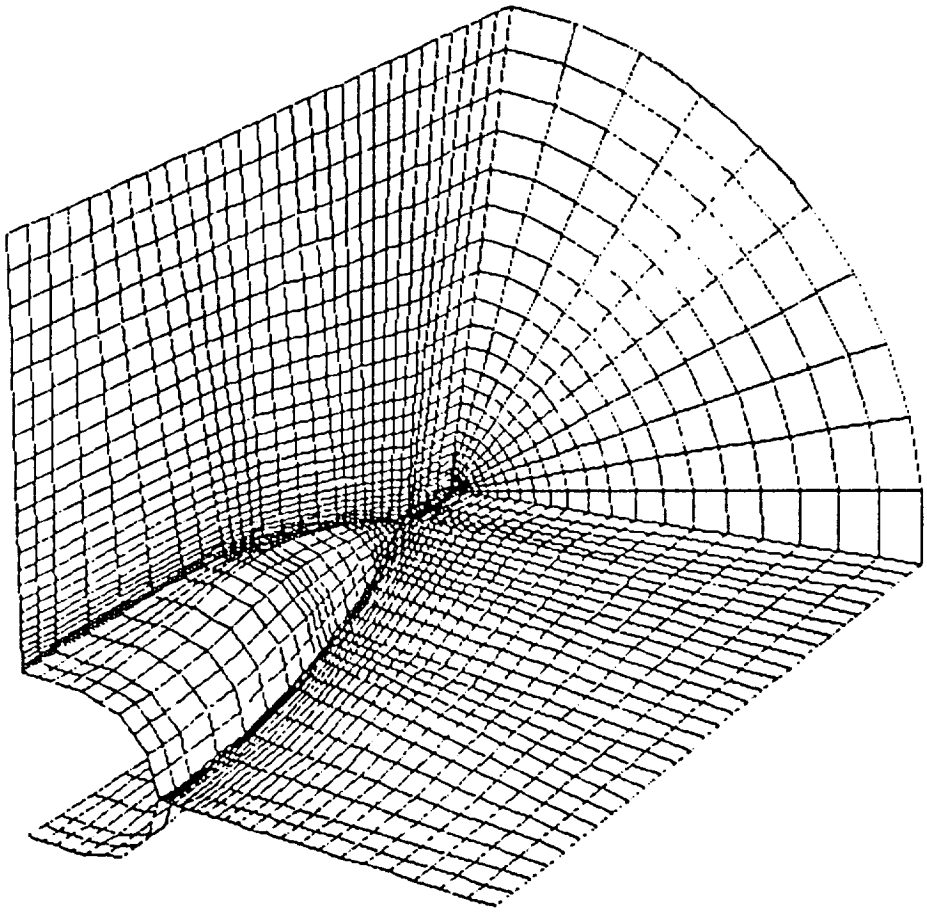

(a) First Block

Figure 16 Grid Topologies for the Fuselage Calculation.

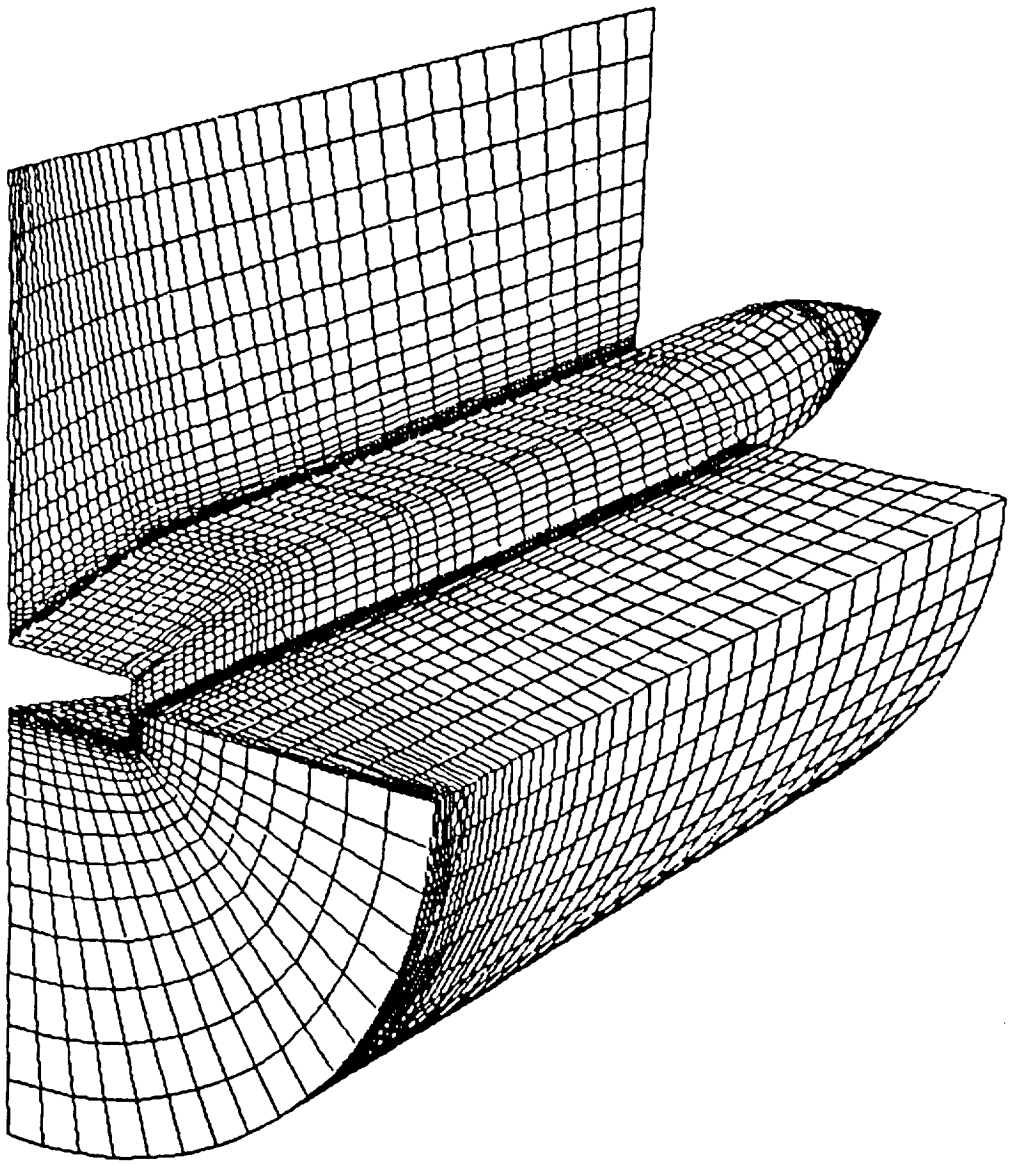

(b) Second Block

Figure 16 Continued.

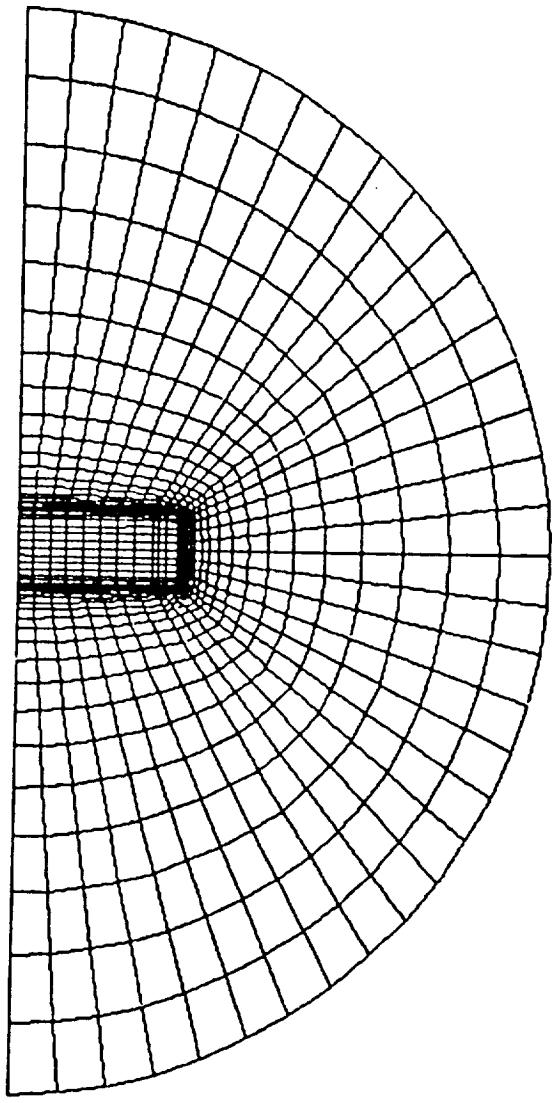

(c) Third Block

Figure 16 Concluded.

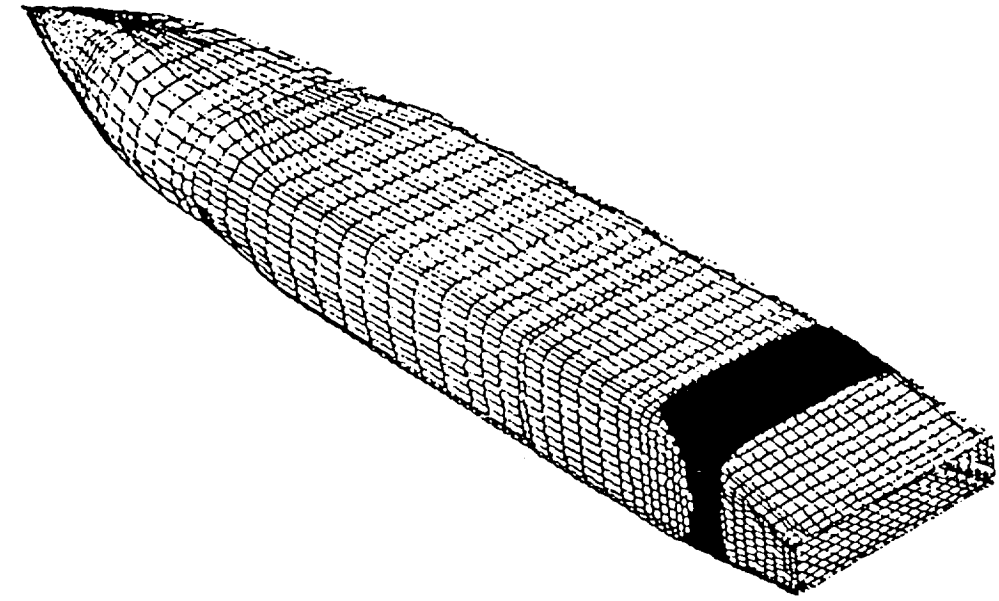

(a) $\delta_d = 0°$

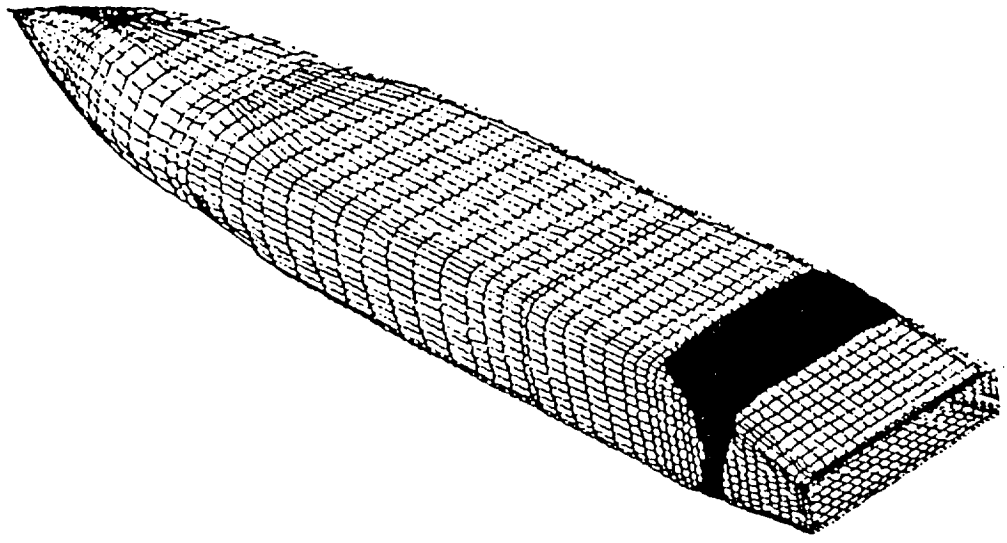

(b) $\delta_d = 30°$

Figure 17 Indication of Supersonic Regions on the Fuselage.

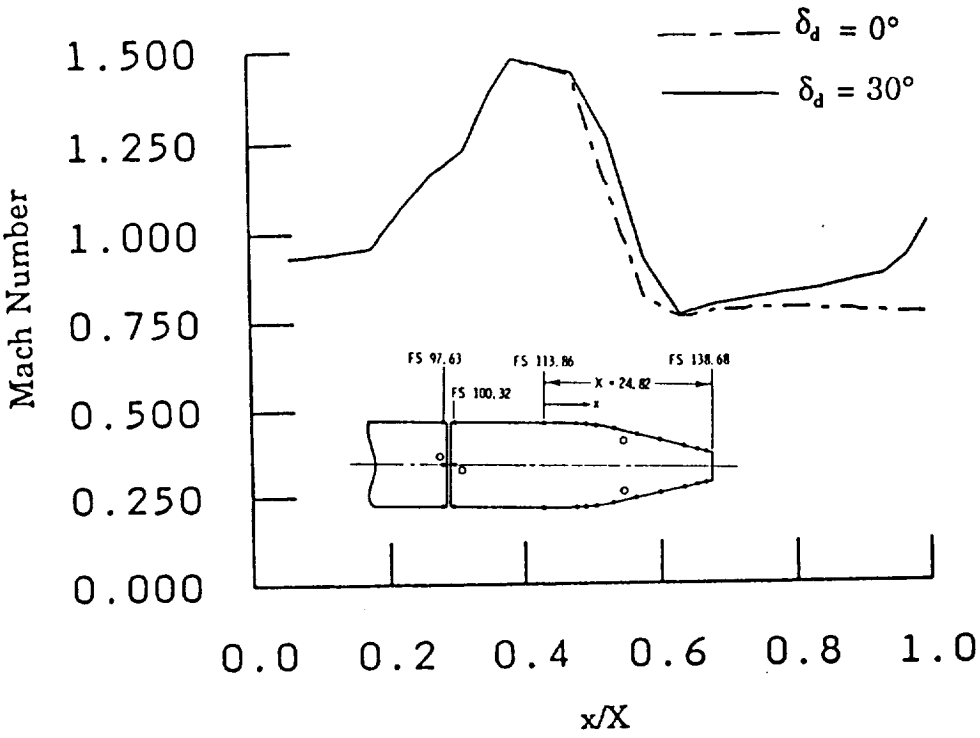

Figure 18 Sectional Mach Number Distributions on the Fuselage; $\alpha = 0°$; M = 0.9; 2y/b = 0.0; $M_{jet} = 1.7$; $P_{jet} = P_{inf}$.

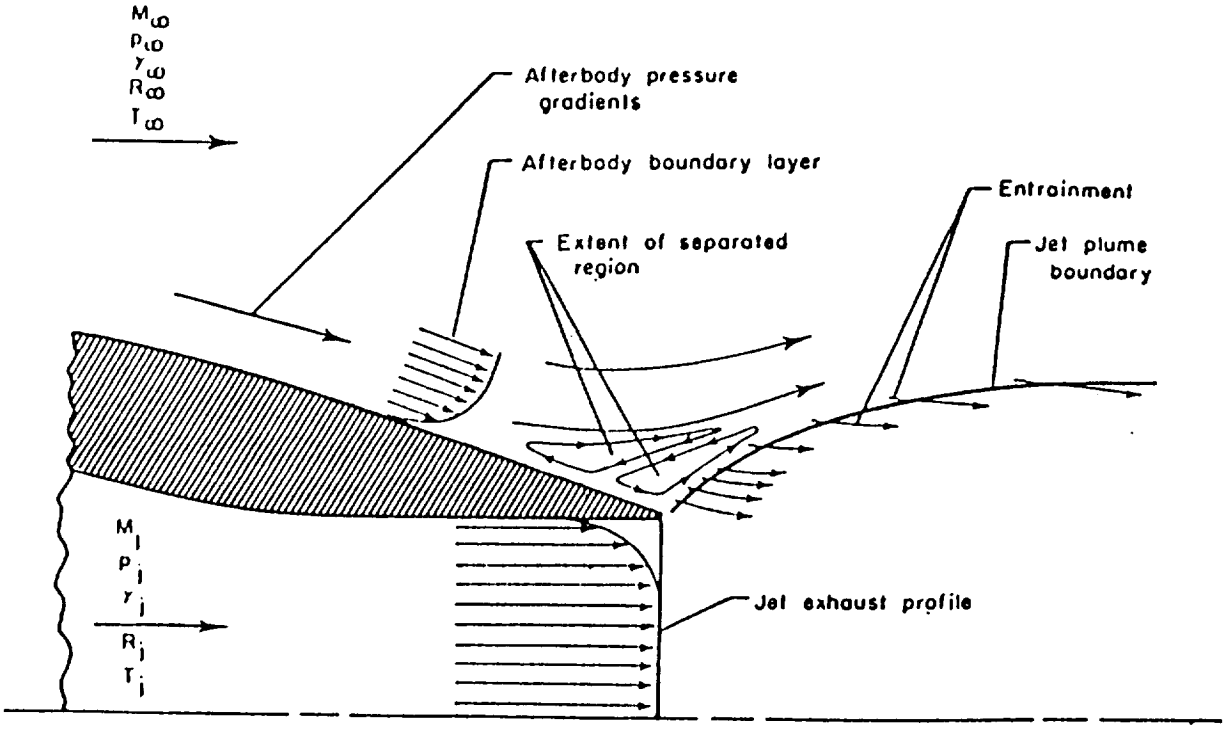

Figure 19 Factors Influencing Jet Interference (Taken from Ref. 43).

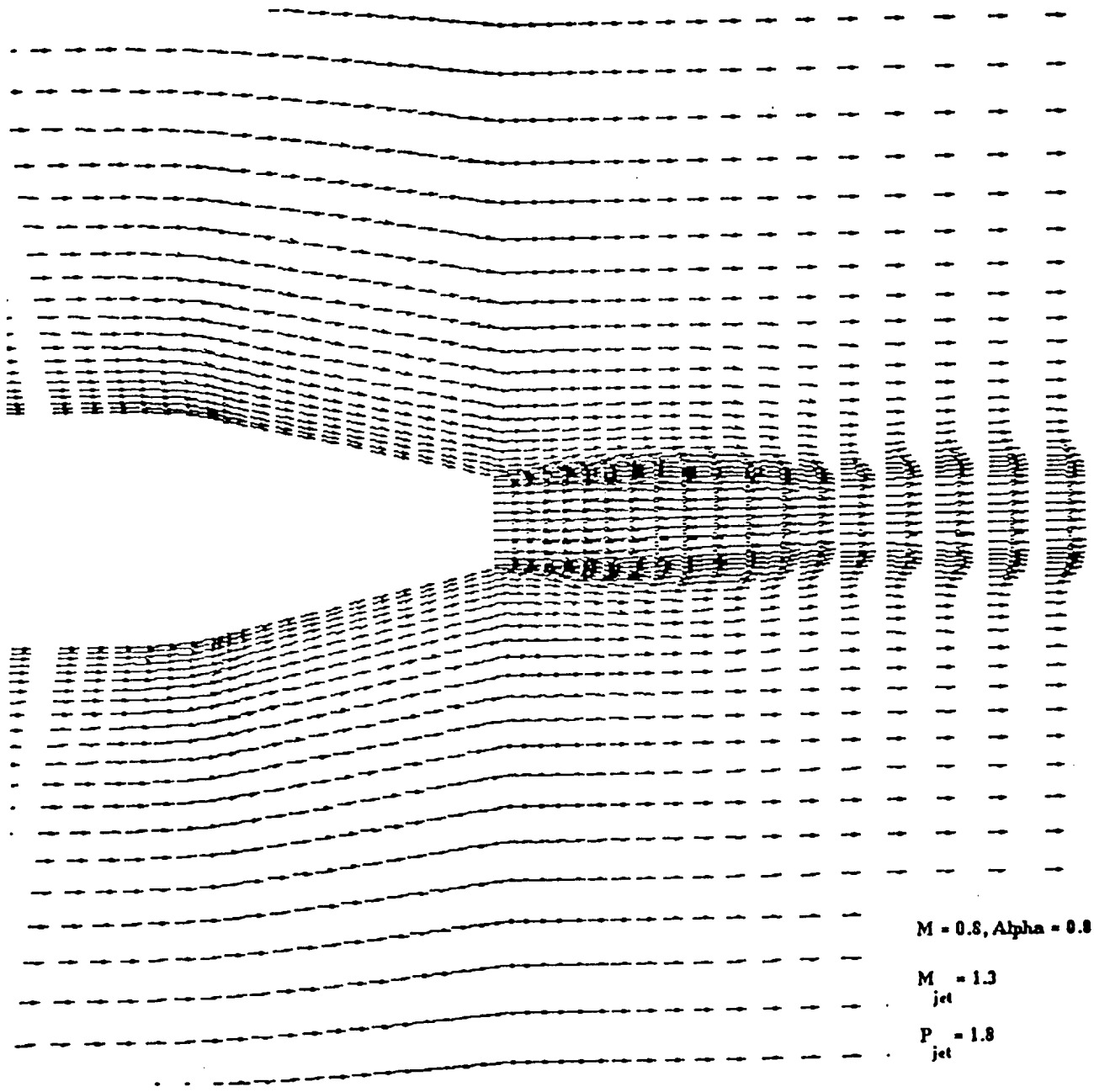

Figure 20 Sectional Velocity Vectors of the Fuselage with a Rectangular Nozzle; M_{jet} = 1.3; P_{jet} = 1.8 P_{inf}; M = 0.8; α = 0°; 2y/b = 0.

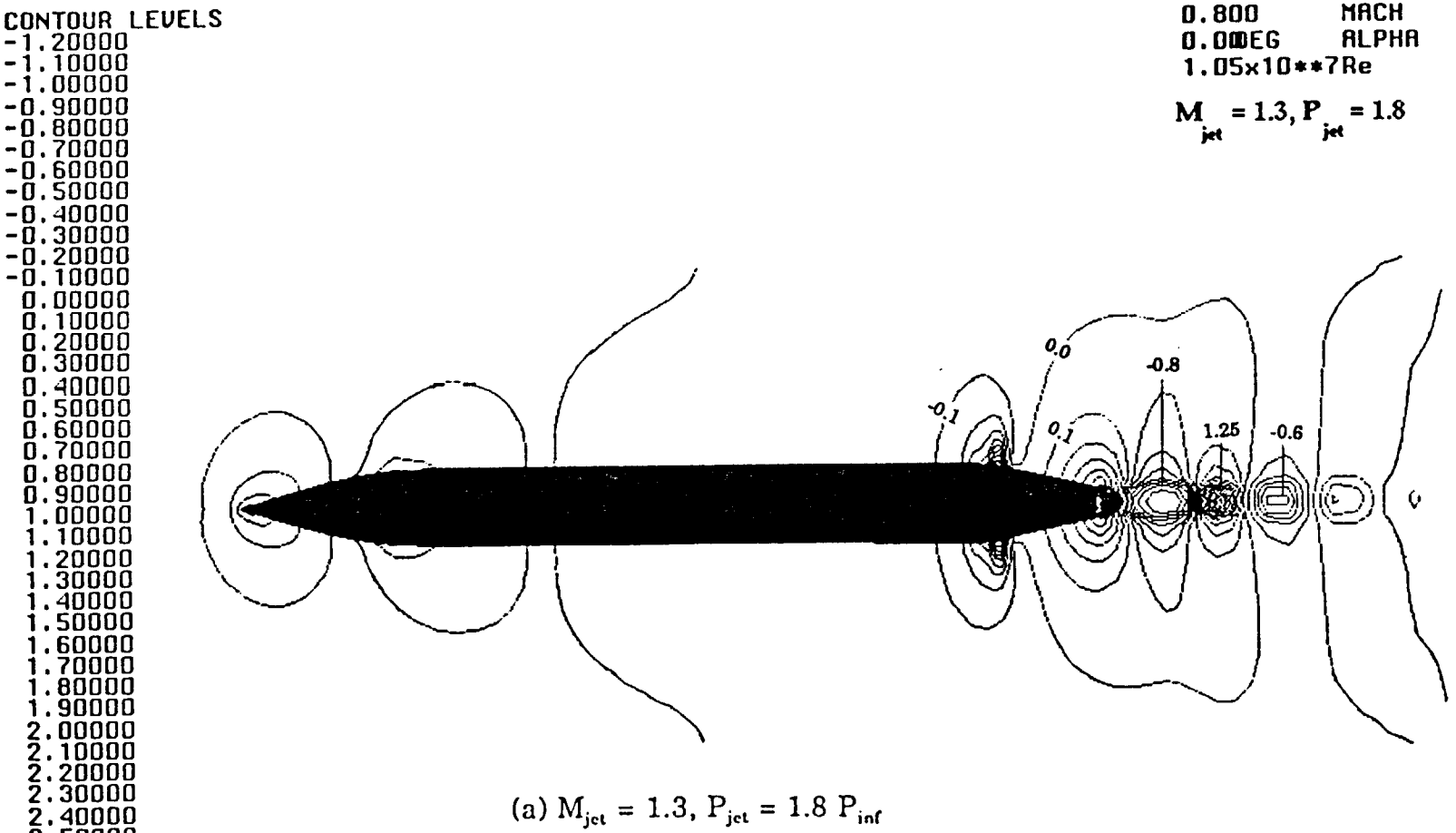

(a) $M_{jet} = 1.3$, $P_{jet} = 1.8\ P_{inf}$

Figure 21 Pressure Contours of the Fuselage Configuration; M = 0.8; $\alpha = 0°$; 2y/b = 0.

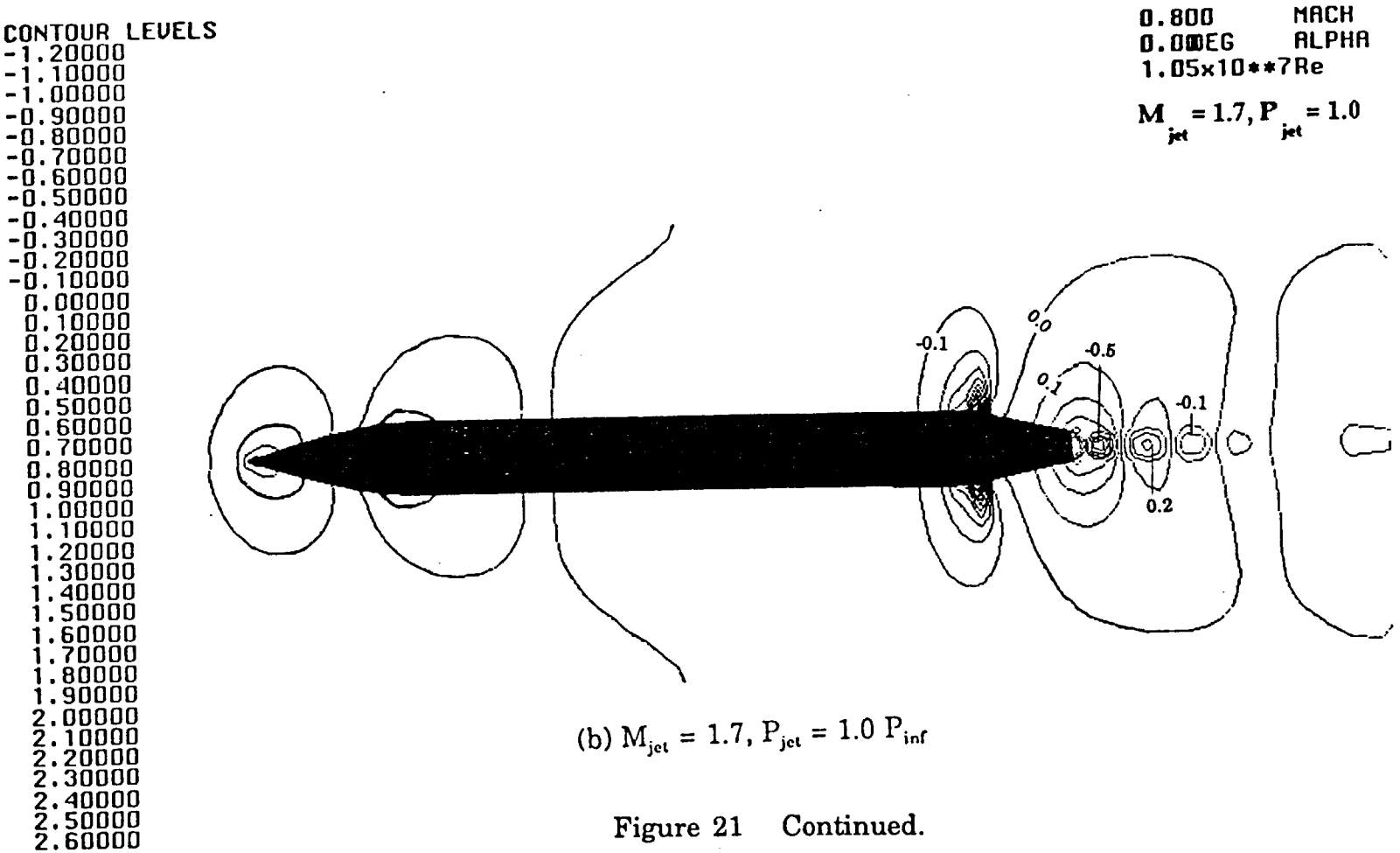

(b) $M_{jet} = 1.7$, $P_{jet} = 1.0\ P_{inf}$

Figure 21 Continued.

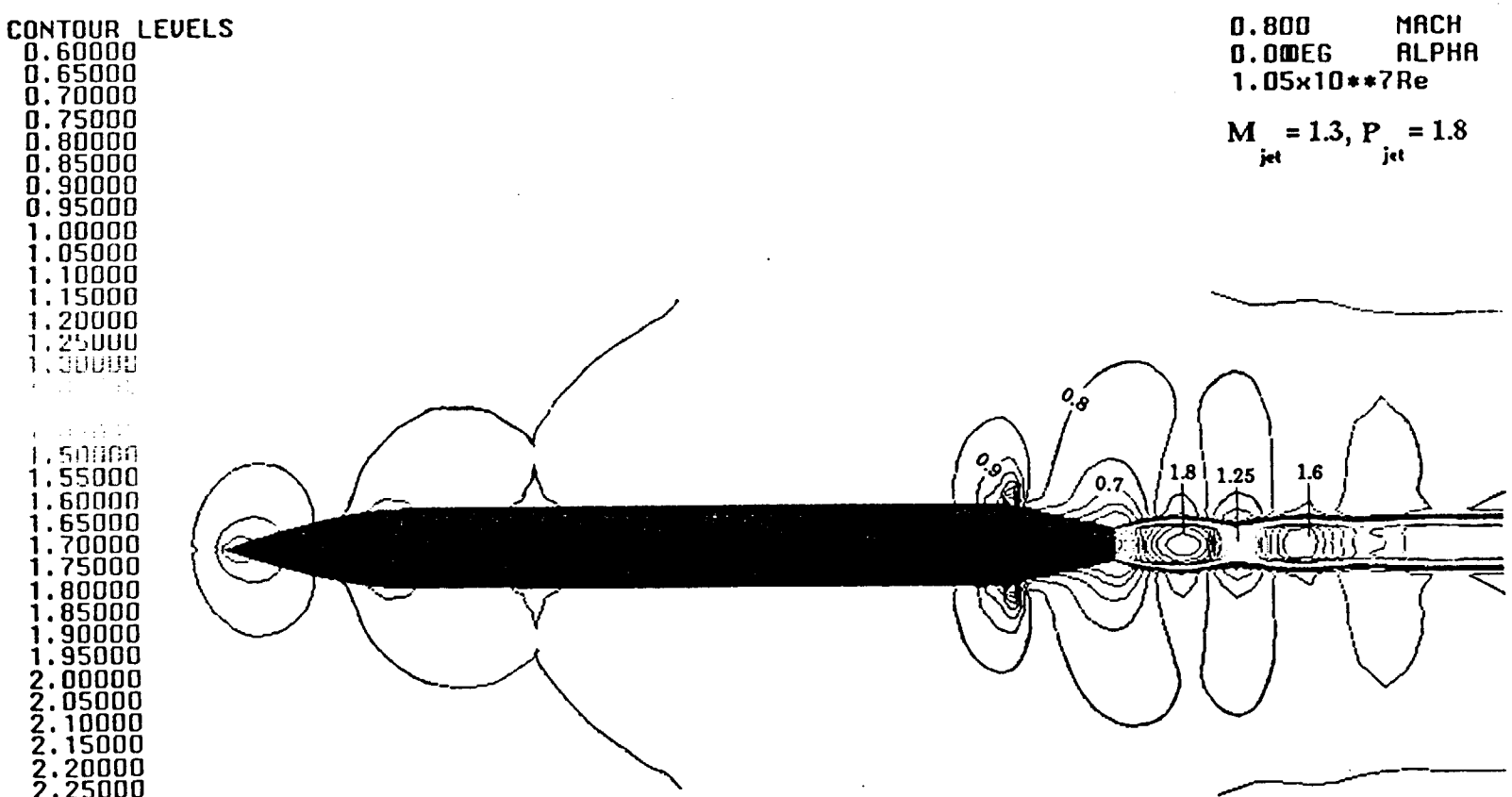

(a) $M_{jet} = 1.3$, $P_{jet} = 1.8\ P_{inf}$

Figure 22 Mach Number Contours of the Fuselage Configuration; M = 0.8; $\alpha = 0°$; 2y/b = 0.

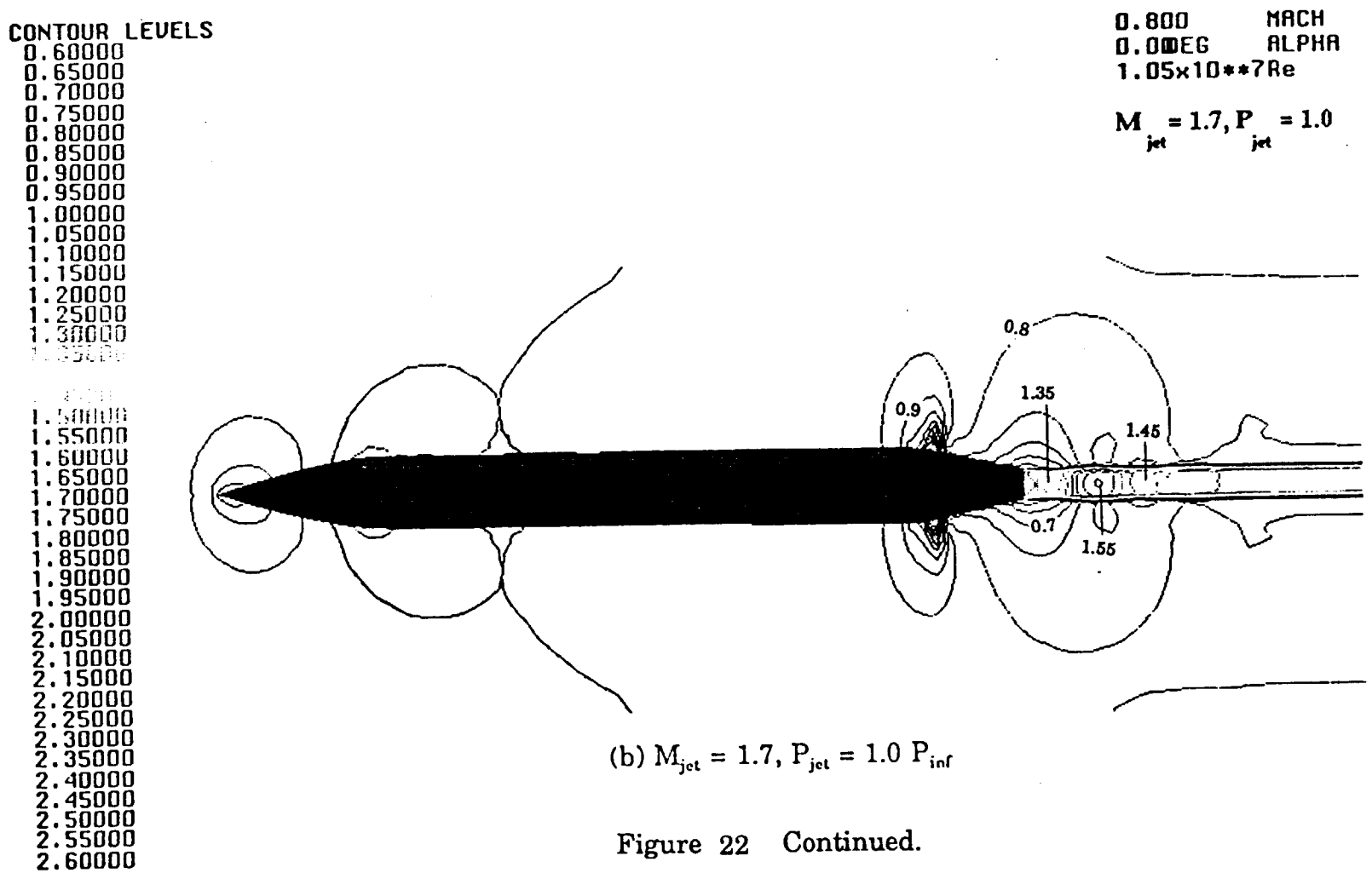

(b) $M_{jet} = 1.7$, $P_{jet} = 1.0\ P_{inf}$

Figure 22 Continued.

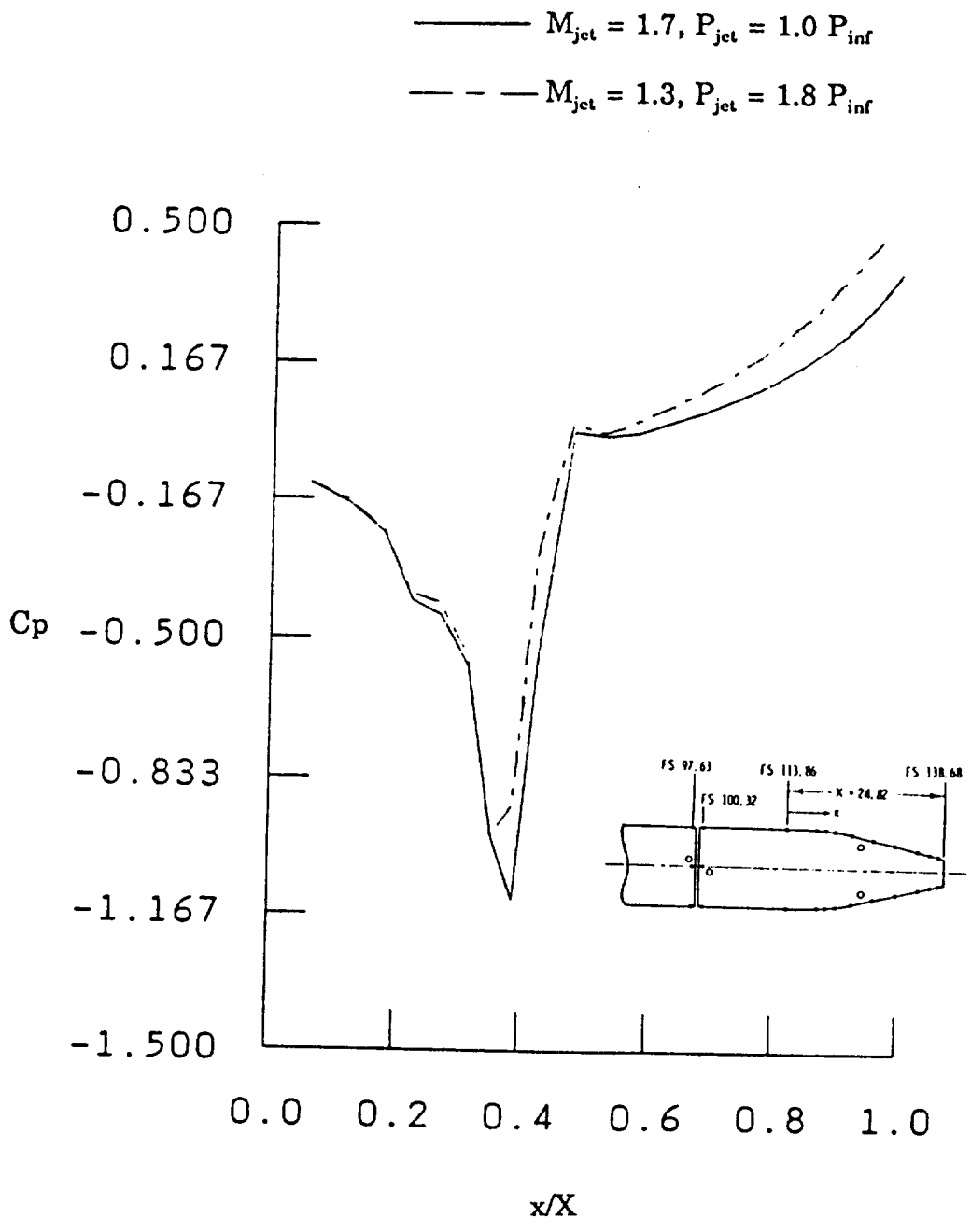

Figure 23 Pressure Distributions on the Afterbody of the Fuselage with a Rectangular Nozzle; $\alpha = 0°$; M = 0.8; 2y/b = 0.

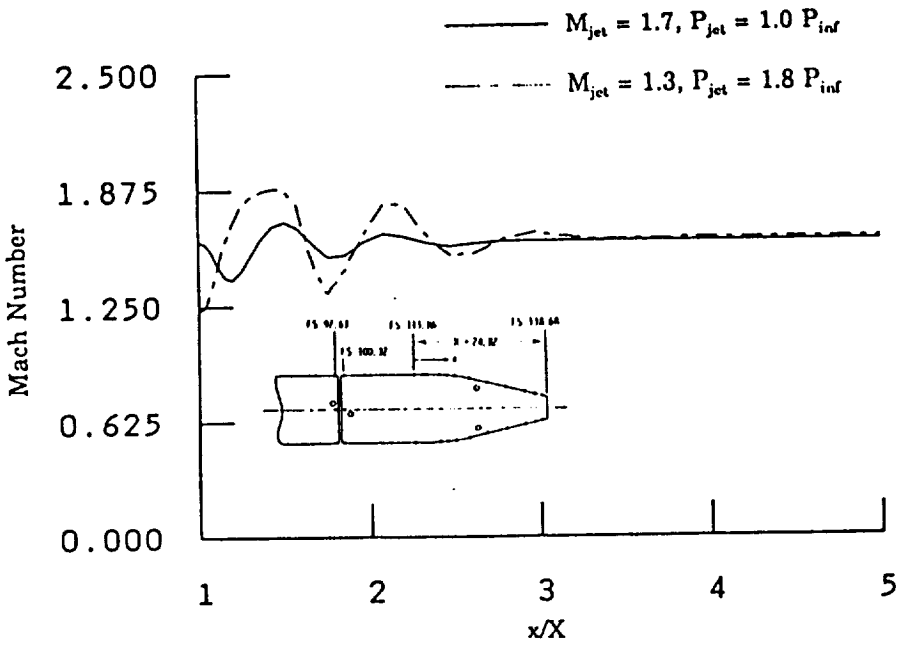

(a) Mach Number

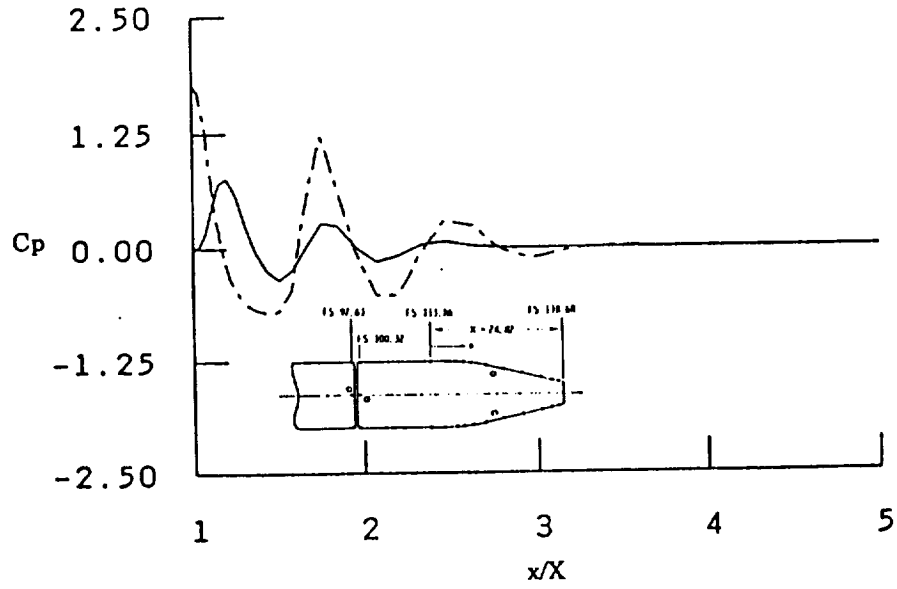

(b) Pressure Coefficient

Figure 24 Flow Properties along the Centerline of the Jet; $\alpha = 0°$; M = 0.8.

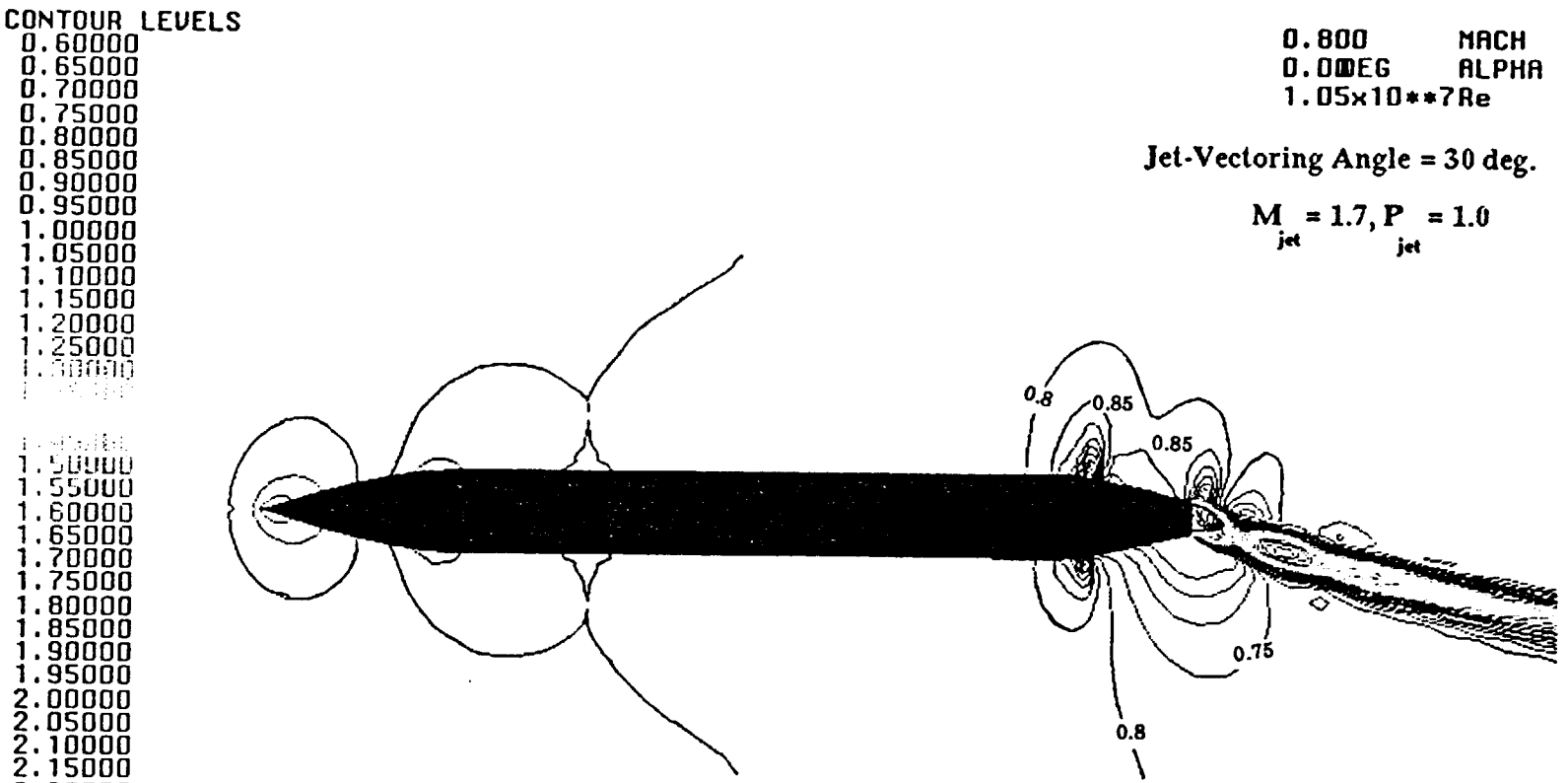

(a) M_{jet} = 1.7, P_{jet} = 1.0 P_{inf}

Figure 25 Mach Number Contours of the Fuselage Configuration; M = 0.8; α = 0°; 2y/b = 0.

(b) $M_{jet} = 1.3$, $P_{jet} = 1.8\ P_{inf}$

Figure 25 Continued.

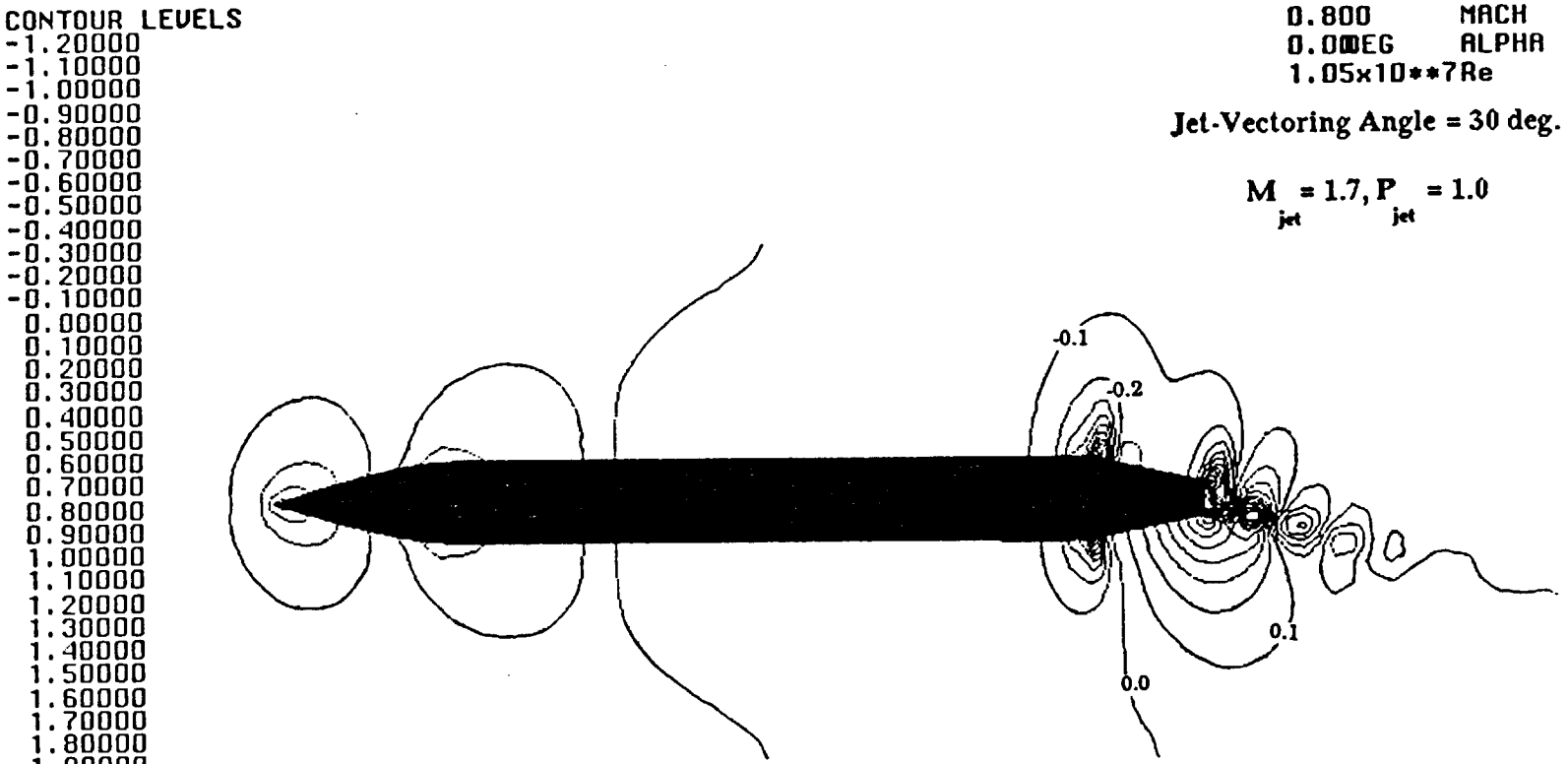

(a) $M_{jet} = 1.7$, $P_{jet} = 1.0\ P_{inf}$

Figure 26 Pressure Contours of the Fuselage Configuration; M = 0.8; $\alpha = 0°$; 2y/b = 0.

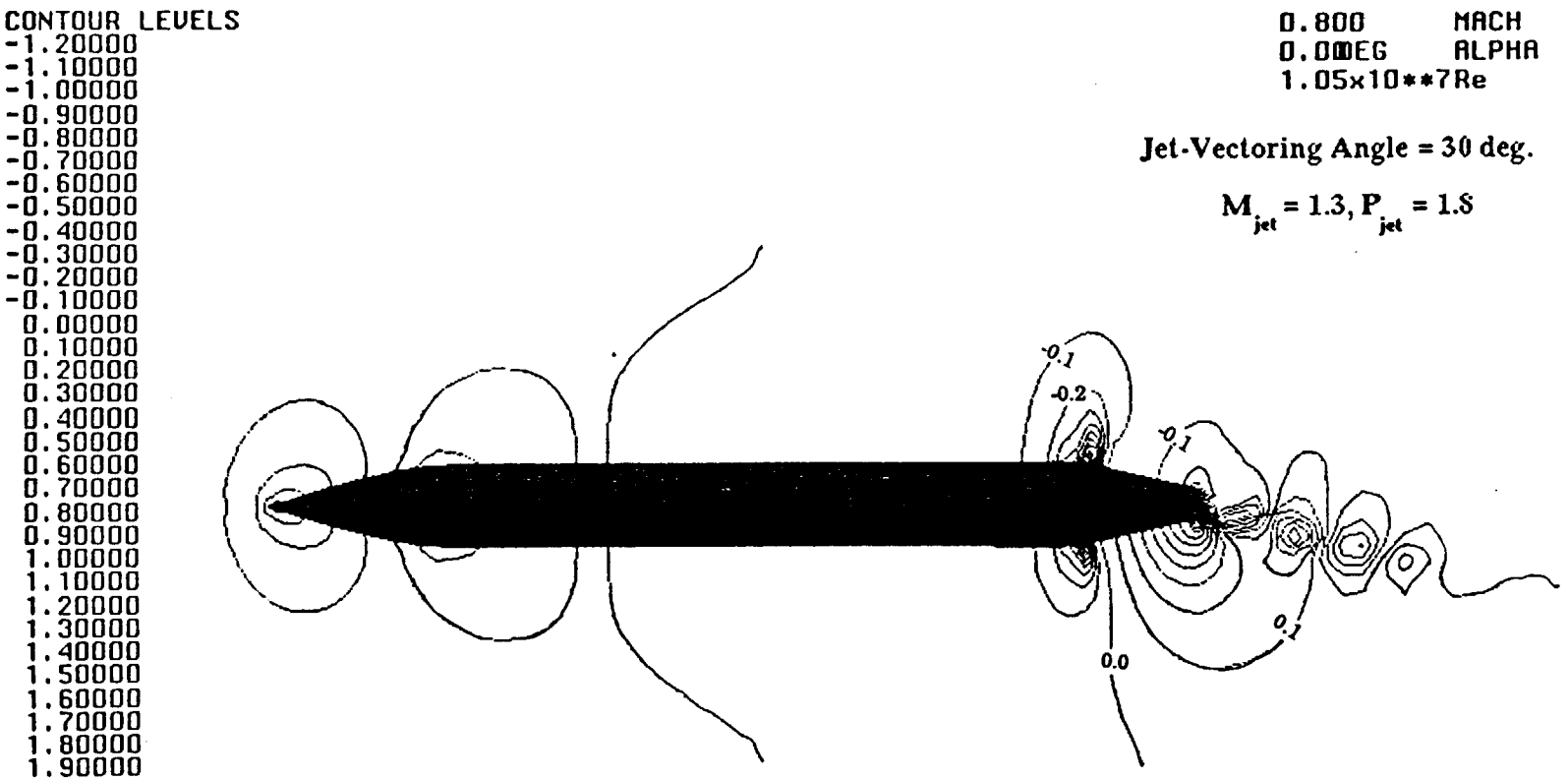

(b) M_{jet} = 1.3, P_{jet} = 1.8 P_{inf}

Figure 26 Continued.

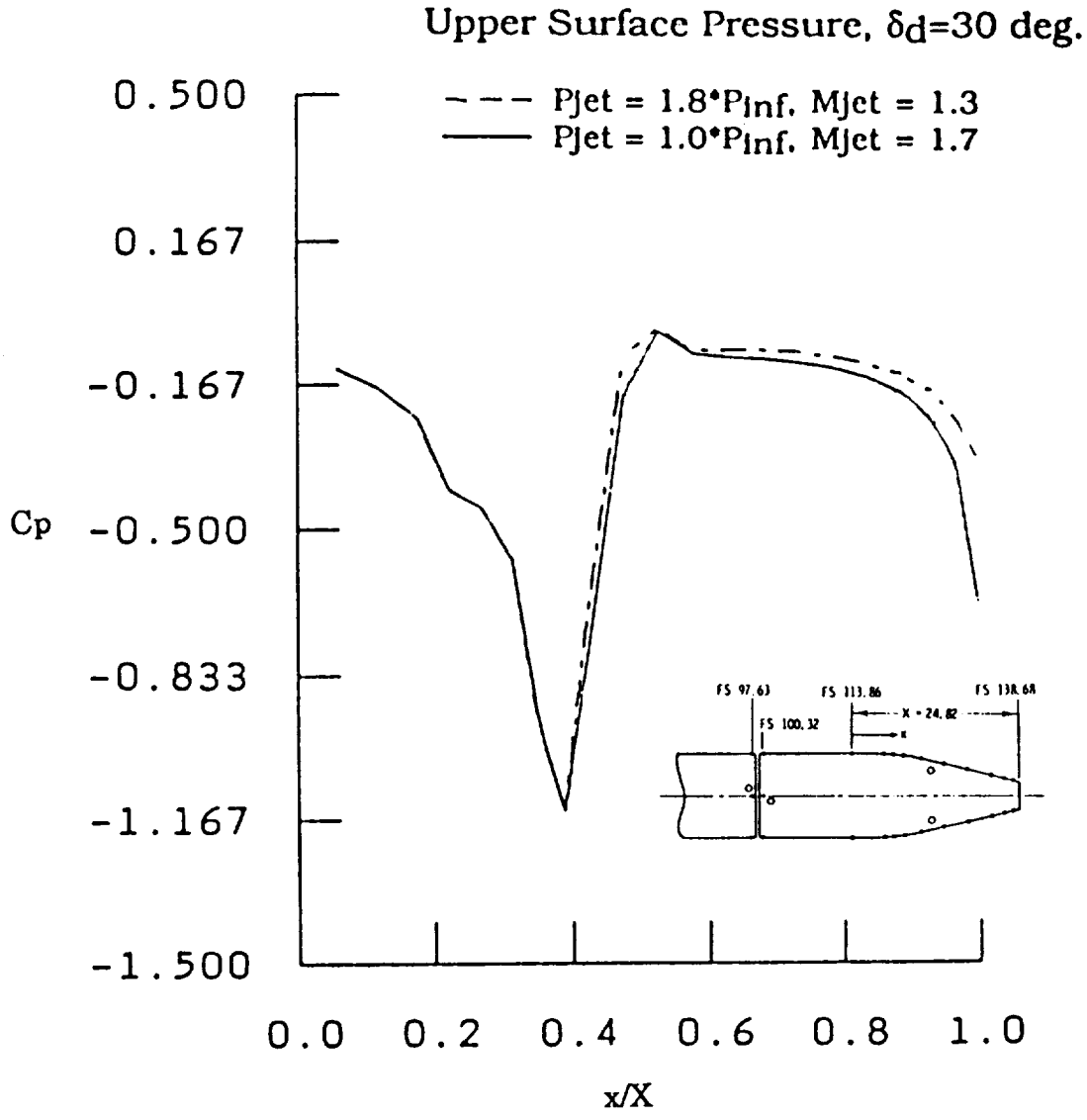

Figure 27 Pressure Distributions on the Upper Surface of the Fuselage Configuration.

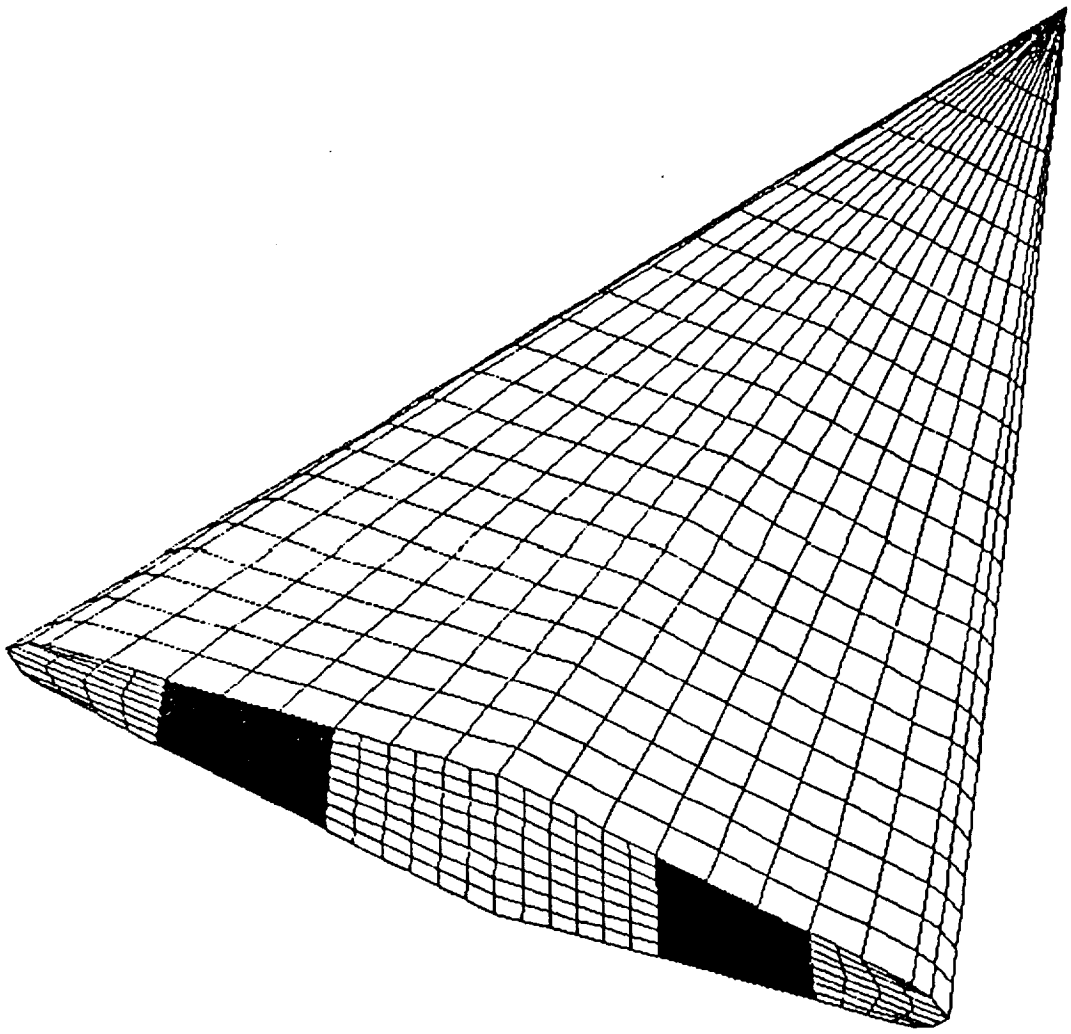

Figure 28 Geometry of the 63-Degree Delta Body with Two Trapezoidal Nozzles.

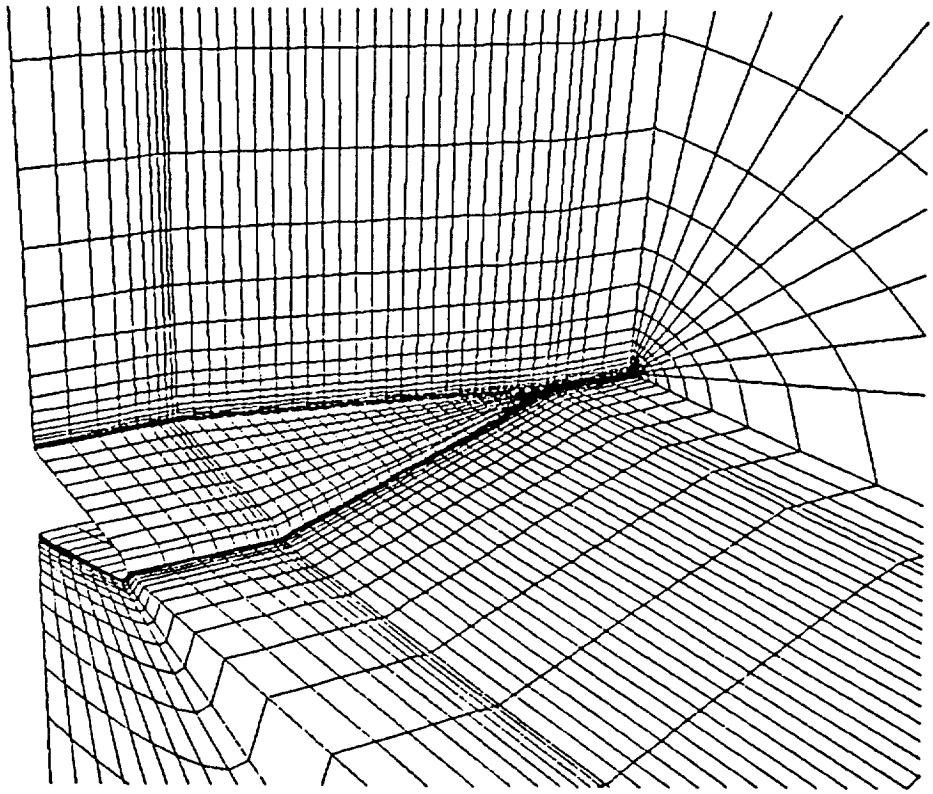

(a) First Block

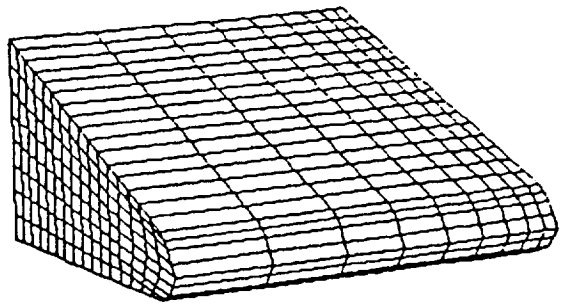

(b) Second Block

Figure 29 Grid Topologies for the Delta Body Calculation.

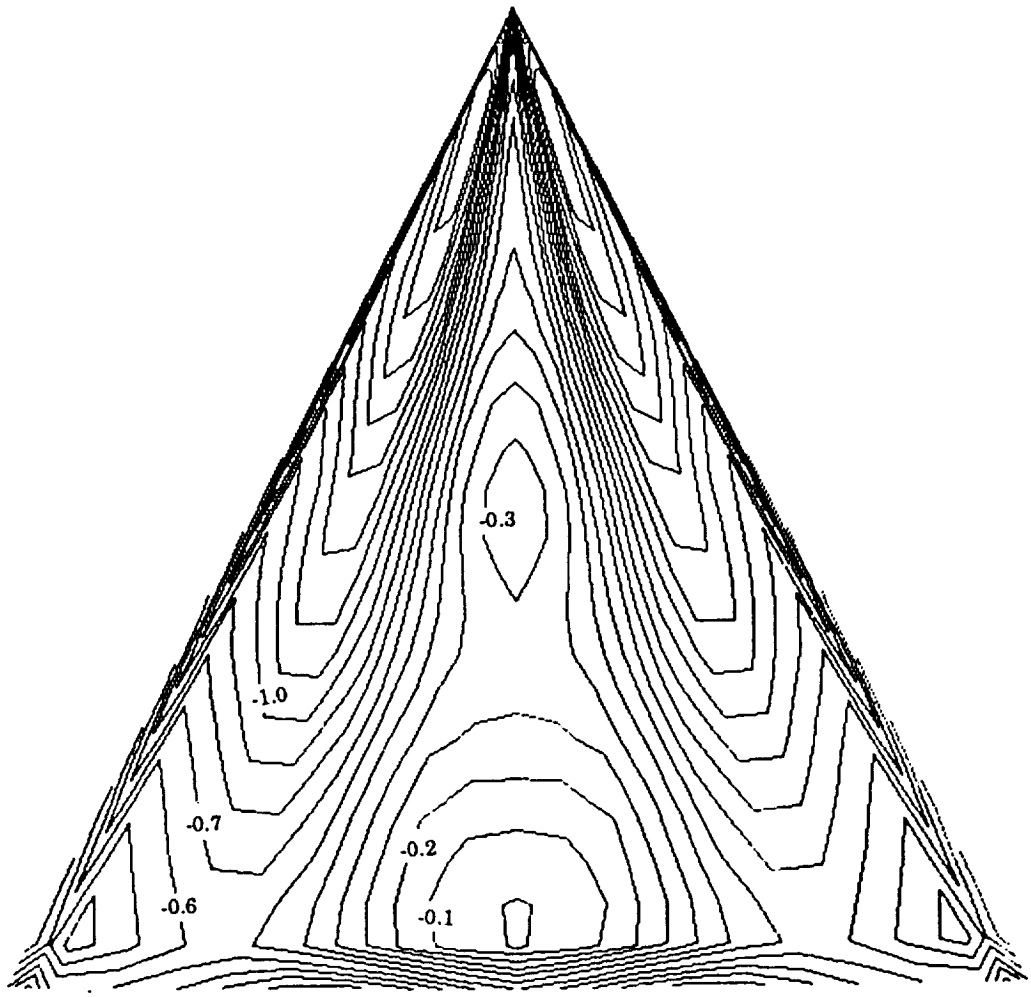

(a) Upper Surface

Figure 30 Pressure Distribution on the 63-Degree Delta Body without Jet; $\alpha = 25°$; $M_\infty = 0.6$.

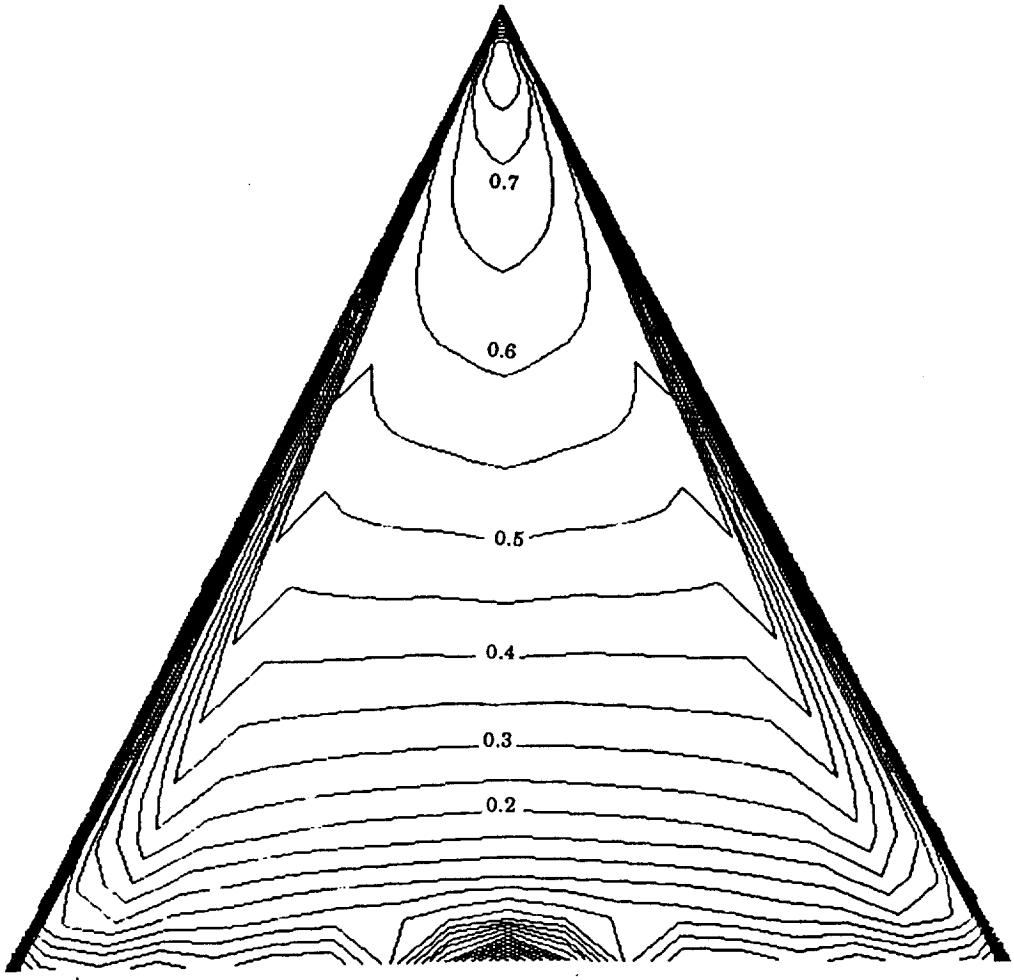

(b) Lower surface

Figure 30 Continued.

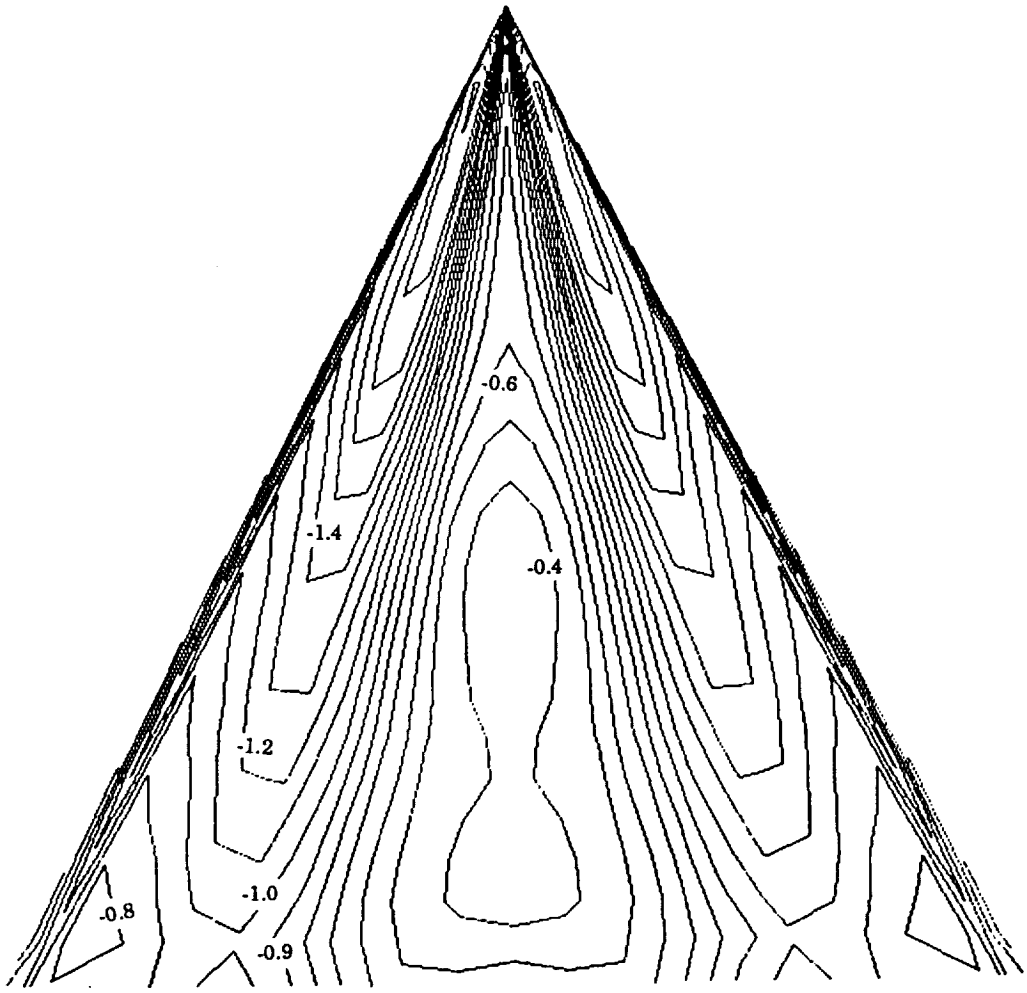

(a) Upper Surface

Figure 31 Pressure Distributions on the 63-Degree Delta Body with Straight Jet; $\alpha = 25°$; $M_\infty = 0.6$; $M_{jet} = 2$; $P_{jet} = P_{inf}$.

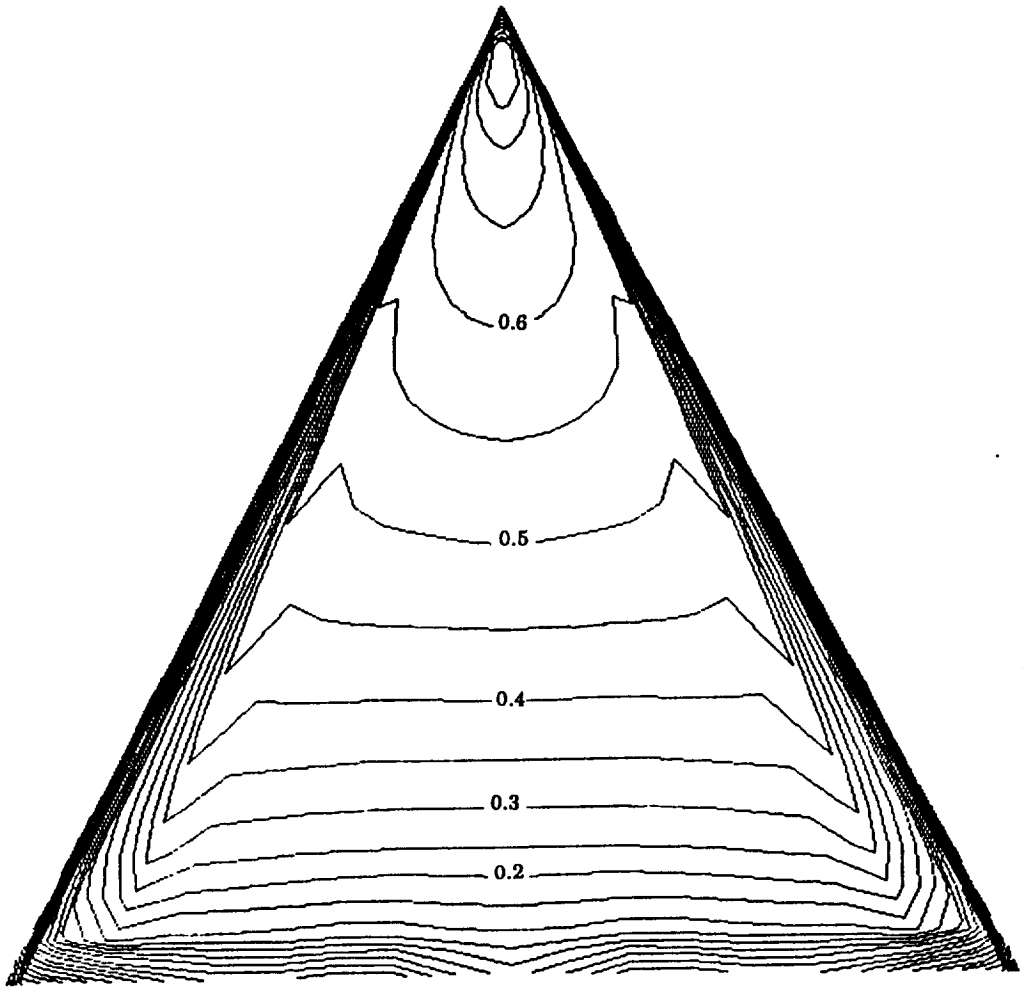

(b) Lower Surface

Figure 31 Continued.

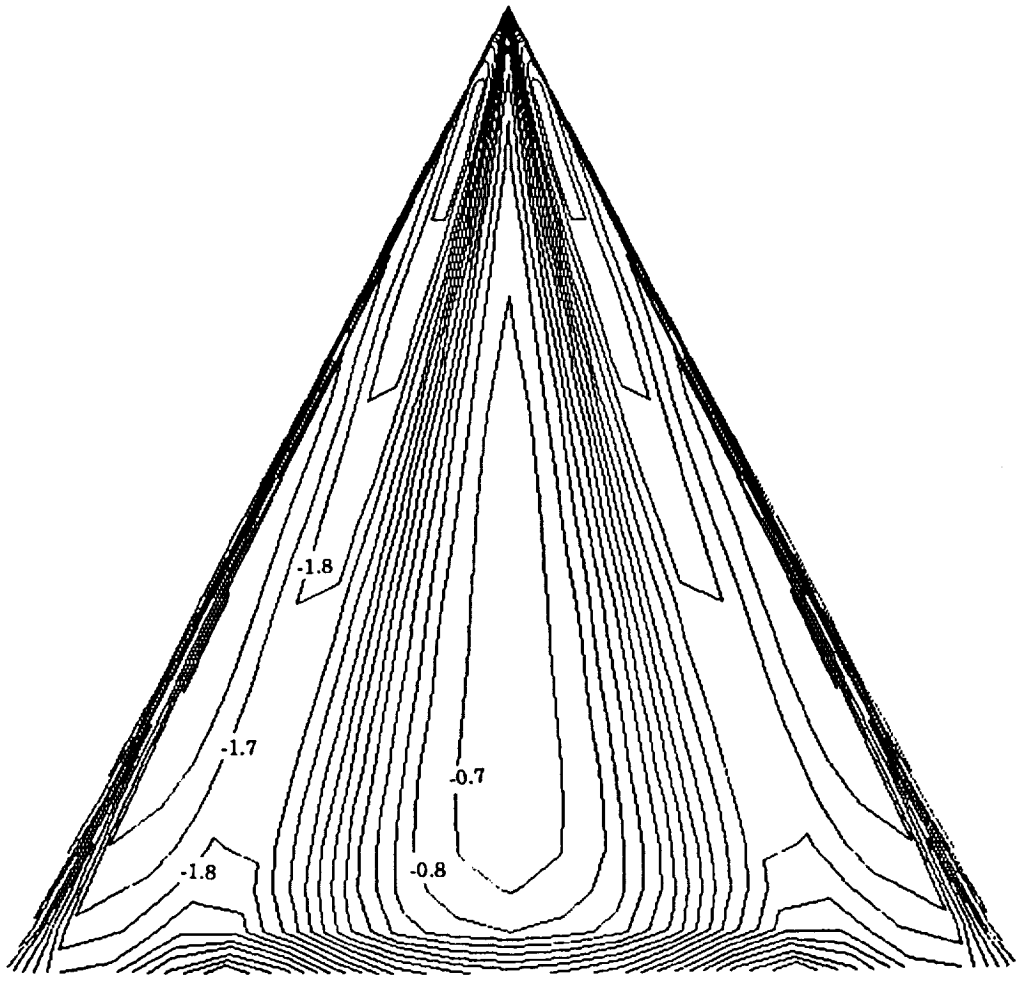

(a) Upper Surface

Figure 32 Pressure Distribution on the 63-Degree Delta Body with 30-Degree Vectored Jet; $\alpha = 25°$; $M_\infty = 0.6$; $M_{jet} = 2$; $P_{jet} = P_{inf}$.

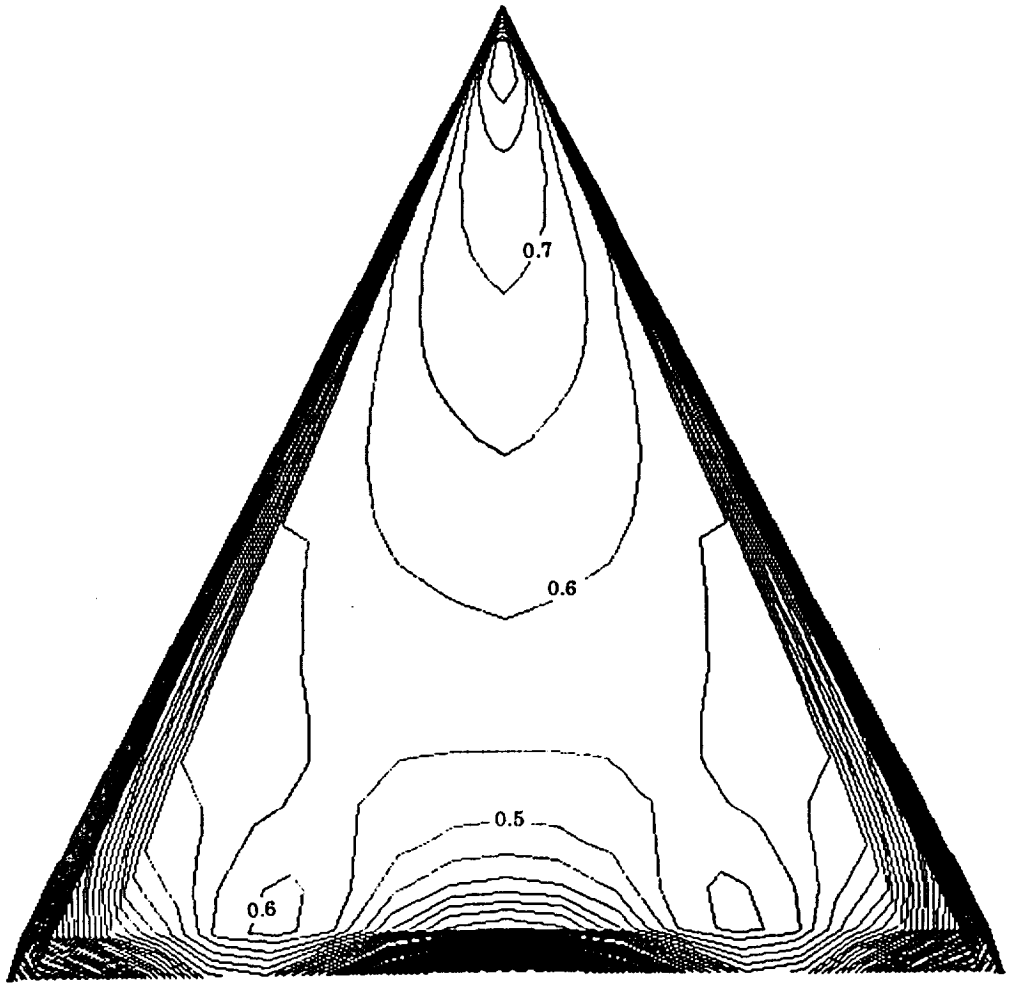

(b) Lower Surface

Figure 32 Continued.

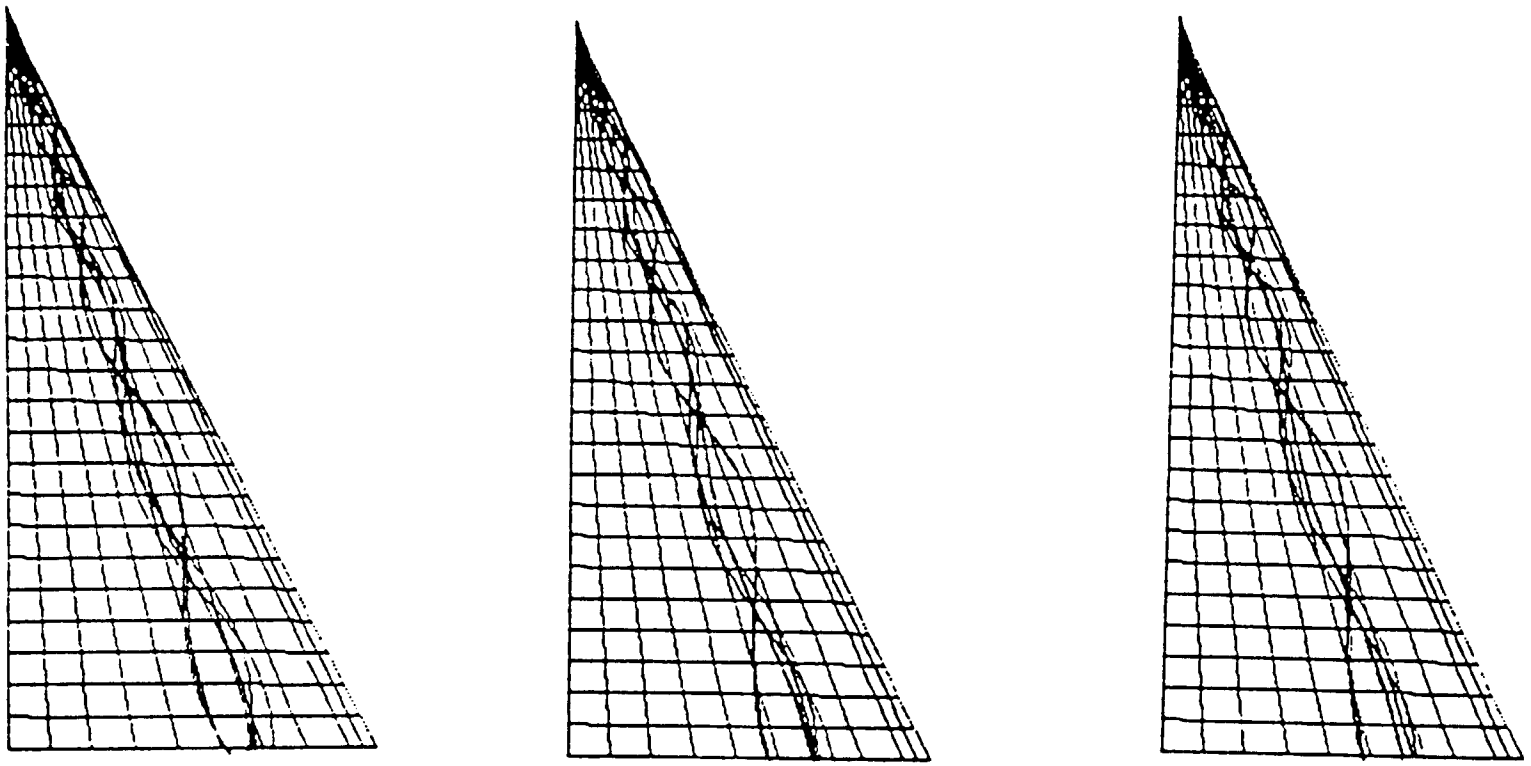

Figure 33 Inner Vortex Filament of the 63-Degree Delta Body with Various Jet Conditions.

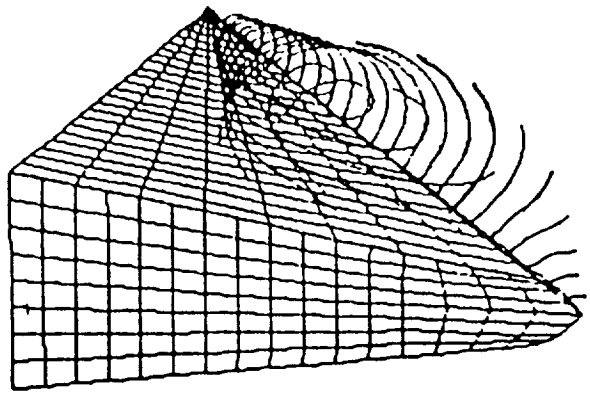

(a) Jet Off

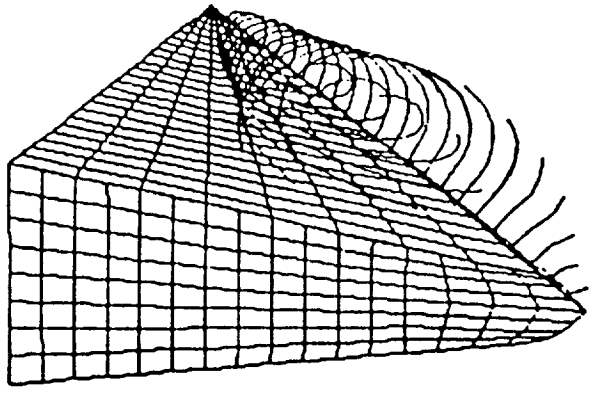

(b) δ_d = 0 deg.

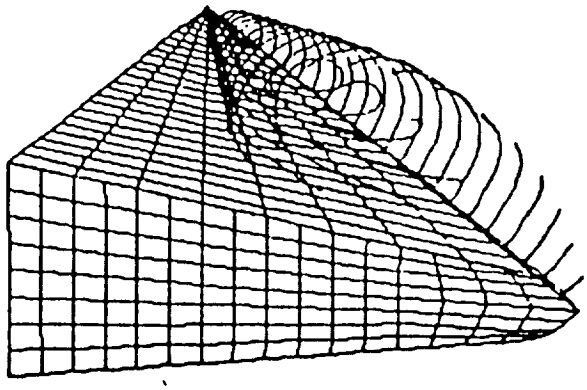

(c) δ_d= 30 deg.

Figure 34 Outer Vortex Filament of the 63-Degree Delta Body with Various Jet Conditions.

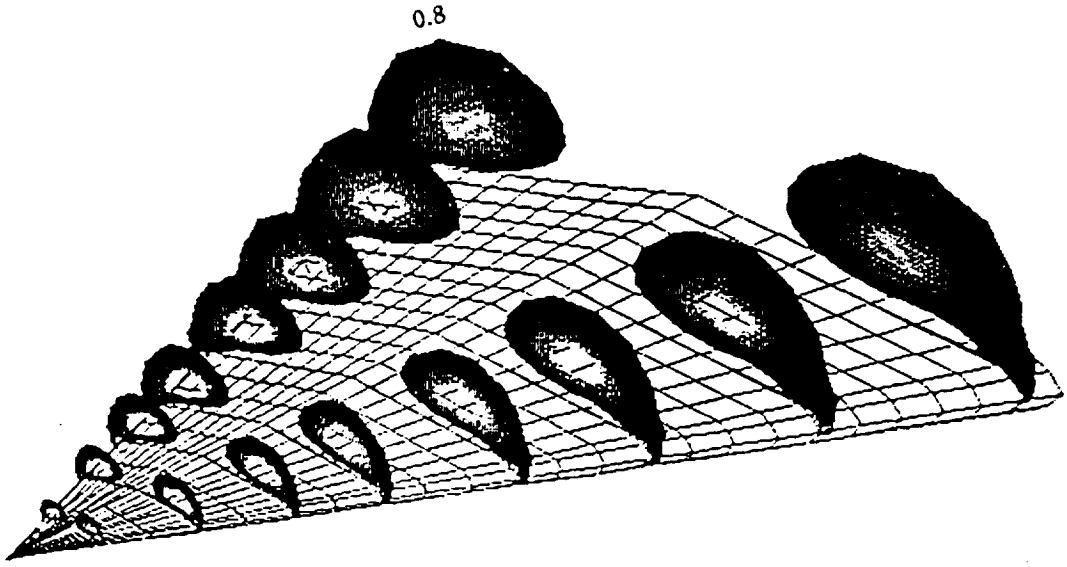

(a) δ_d = 0 deg.

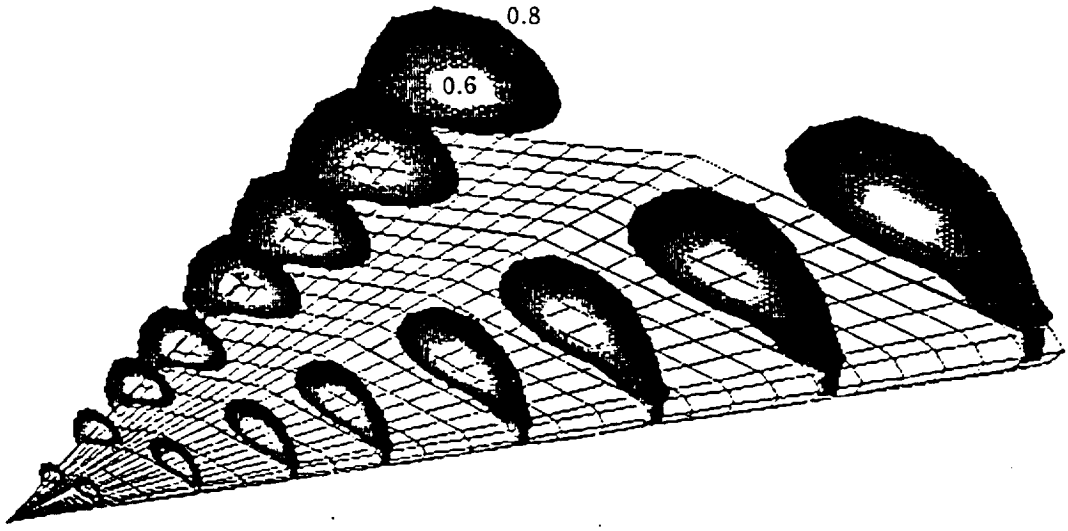

(b) δ_d = 30 deg.

Figure 35 Total Cross Section Pressure Contours of the 63-Degree Delta Wing; α = 25°; M_∞ = 0.6; M_{jet} = 2; $P_{jet} = P_{inf}$.

APPENDIX A:

GENERALIZED TRANSFORMATION

Consider a completely general transformation of the form

$$\begin{aligned} \xi &= \xi(x, y, z) \\ \eta &= \eta(x, y, z) \\ \zeta &= \zeta(x, y, z) \end{aligned} \tag{A.1}$$

The partial derivatives in the x, y, z coordinates can be written as

$$\begin{aligned} \frac{\partial}{\partial x} &= \frac{\partial}{\partial \xi}\xi_x + \frac{\partial}{\partial \eta}\eta_x + \frac{\partial}{\partial \zeta}\zeta_x \\ \frac{\partial}{\partial y} &= \frac{\partial}{\partial \xi}\xi_y + \frac{\partial}{\partial \eta}\eta_y + \frac{\partial}{\partial \zeta}\zeta_y \\ \frac{\partial}{\partial z} &= \frac{\partial}{\partial \xi}\xi_z + \frac{\partial}{\partial \eta}\eta_z + \frac{\partial}{\partial \zeta}\zeta_z \end{aligned} \tag{A.2}$$

Also, the differential form of the generalized coordinate (ξ, η, ζ) can be written as

$$\begin{aligned} d\xi &= \xi_x dx + \xi_y dy + \xi_z dz \\ d\eta &= \eta_x dx + \eta_y dy + \eta_z dz \\ d\zeta &= \zeta_x dx + \zeta_y dy + \zeta_z dz \end{aligned} \tag{A.3}$$

In a matrix form, Equation (A.3) can be written as

$$\begin{bmatrix} d\xi \\ d\eta \\ d\zeta \end{bmatrix} = \begin{bmatrix} \xi_x & \xi_y & \xi_z \\ \eta_x & \eta_y & \eta_z \\ \zeta_x & \zeta_y & \zeta_\xi \end{bmatrix} \begin{bmatrix} dx \\ dy \\ dz \end{bmatrix} \tag{A.4}$$

In a similar manner, the differential form of (x, y, z) can be written as

$$\begin{bmatrix} dx \\ dy \\ dz \end{bmatrix} = \begin{bmatrix} x_\xi & x_\eta & x_\zeta \\ y_\xi & y_\eta & y_\zeta \\ z_\xi & z_\eta & z_\zeta \end{bmatrix} \begin{bmatrix} d\xi \\ d\eta \\ d\zeta \end{bmatrix} \tag{A.5}$$

Therefore,

$$\begin{bmatrix} \xi_x & \xi_y & \xi_z \\ \eta_x & \eta_y & \eta_z \\ \zeta_x & \zeta_y & \zeta_z \end{bmatrix} = \begin{bmatrix} x_\xi & x_\eta & x_\zeta \\ y_\xi & y_\eta & y_\zeta \\ z_\xi & z_\eta & z_\zeta \end{bmatrix}^{-1}$$

$$= J \begin{bmatrix} (y_n z_\zeta - y_\zeta z_\eta) & -(x_\eta z_\zeta - x_\zeta z_\eta) & (x_\eta y_\zeta - x_\zeta y_\eta) \\ -(y_\xi z_\zeta - y_\zeta z_\xi) & (x_\xi z_\zeta - x_\zeta z_\xi) & -(x_\xi yxub\zeta - x_\zeta y_\xi) \\ (y_\xi z_\eta - y_\eta z_\xi) & -(x_\xi z_\eta - x_\eta z_\xi) & (x_\xi y_\eta - x_\eta y_\xi) \end{bmatrix} \tag{A.6}$$

$$J = [(y_\eta z_\zeta - (y_\xi z_\zeta - y_\zeta z_\xi)x_\eta + x_\zeta(y_\xi z_\eta - y_\eta z_\xi)]$$

Equation (2) can be written as

$$\begin{aligned} &=> \frac{\partial Q}{\partial t} \\ &+ \frac{\partial}{\partial \xi}(F - F_u)\xi_x + \frac{\partial}{\partial \eta}(F - F_u)\eta_x + \frac{\partial}{\partial \zeta}(F - F_u)\zeta_x \\ &+ \frac{\partial}{\partial \eta}(G - G_v) + \frac{\partial}{\partial \eta}(G - G_u)\eta_y + \frac{\partial}{\partial \zeta}(G - G_u)\zeta_y \\ &+ \frac{\partial}{\partial \xi}(H - H_u)\xi_x + \frac{\partial}{\partial \eta}(H - H_v)\eta_y + \frac{\partial}{\partial \zeta}(H - H_v)\zeta_z = 0 \end{aligned} \qquad \textbf{(A.7)}$$

where

$$\frac{\partial Q}{\partial t} = \frac{\partial Q}{\partial \xi}\frac{\partial \xi}{\partial t} + \frac{\partial Q}{\partial \eta}\frac{\partial \eta}{\partial t} + \frac{\partial Q}{\partial \zeta}\frac{\partial \zeta}{\partial t} + \frac{\partial Q}{\partial t}$$

Equations (8) and (9) can be obtained by rearranging Equation (A.7).

APPENDIX B:

DERIVATION OF VAN LEER'S FLUX VECTOR SPLITTING FORMULATION

The goal of van Leer's flux vector splitting (Ref. 37) is to split the flux $f(\varpi)$ into a forward flux $f^{+}(\varpi)$ and a backward flux $f(\varpi)$; that is,

(1) $f(\omega) = f^{+}(\omega) + f^{-}(\omega)$; and

(2) $df^{+}/d\omega$ have all non-negative eigenvalues, and

$df^{-}/d\omega$ have all non-positive eigenvalues.

Considering the one-dimensional Euler equations, the full flux can be written as

$$f(\rho, u, p, e) = \begin{pmatrix} \rho u \\ \rho u^2 + p \\ \rho u e + p u \end{pmatrix} = f(\rho, C, M) = \begin{pmatrix} \rho C M \\ \rho C^2 (M^2 + \frac{1}{\gamma}) \\ \rho C^3 M (\frac{1}{2} M^2 + \frac{1}{\gamma - 1}) \end{pmatrix}$$

The flux is split under the following restriction:

(1) $f^{+}(\omega) \equiv f(\omega)$ when $M \geq 1$

$f^{-}(\omega) = f(\omega)$ when $M \leq -1$

(2) $f^{+}(M) = \pm f^{-}(-M)$, if $f(M) = f(-M)$

(3) $\dfrac{df^{\pm}}{d\omega}$ must be continuous

(4) $\dfrac{df^{\pm}}{dw}$ must have one eigenvalue vanish for $|M| < 1$

(5) $f^{\pm}(M)$ must be a lowest-possible-degree polynomial in M.

The polynomials of the flux are determined as

$$f^{\pm} = \begin{bmatrix} f_1^{\pm} \\ f_2^{\pm} \\ f_3^{\pm} \end{bmatrix} = \begin{bmatrix} \pm \rho C(M \pm 1)^2/4 \\ f_1^{\pm}[(\gamma - 1)u \pm 2C]/\gamma \\ f_1^{\pm}[(\gamma - 1)u \pm 2C]^2/2(\gamma^2 - 1) \end{bmatrix}$$

For three-dimensional Euler equations, the x-flux can be written as

$$f = \begin{pmatrix} \rho u \\ \rho u^2 + p \\ \rho uv \\ \rho u\omega \\ (\exp)u \end{pmatrix} = \begin{pmatrix} \rho u \\ \rho(u^2 + C^2/\gamma) \\ \rho uv \\ \rho u\omega \\ \rho u[\frac{1}{2}(u^2 + v^2 + w^2) + C^2/\gamma - 1] \end{pmatrix}$$

where

$$e = \frac{p}{\gamma - 1} + \frac{1}{2}\rho(u^2 + v^2 + w^2),\ C = \sqrt{\frac{\gamma p}{\rho}}$$

$$f = \begin{bmatrix} f_1^{\pm} \\ f_2^{\pm} \\ f_3^{\pm} \\ f_4^{\pm} \\ f_5^{\pm} \end{bmatrix} = \begin{bmatrix} \pm \rho C(M_x \pm 1)^2/4 \\ f_1^{\pm}(\gamma - 1)u \pm 2C)/\gamma \\ f_1^{\pm} \cdot v \\ f_1^{\pm} \cdot \omega \\ f_1^{\pm}\left\{\left[\frac{(\gamma - 1)u \pm 2C}{2(\gamma^2 - 1)}\right]^2 + \frac{1}{2}(v^2 + w^2)\right\} \end{bmatrix}$$

In Equation (25),

$$\hat{F} = \frac{|\Delta\xi|}{J}\left[\xi_x F + \xi_y G + \xi_z H\right]$$

$$\hat{F}^{\pm} = \frac{|\Delta\xi|}{J}\left[\xi_x F^{\pm} + \xi_y G^{\pm} + \xi_z H^{\pm}\right]$$

$$= \frac{|\Delta\xi|}{J}\begin{bmatrix} \pm\rho C(M_\xi \pm 1)^2/4 \\ f_1^{\pm}(\bar{u}\xi_x + \bar{v}\xi_y + \bar{w}\xi_z) + \xi_x(f_1^{\pm}[-u \pm 2C]/\gamma) \\ f_1^{\pm}(\bar{u}\eta_x + \bar{v}\eta_y + \bar{w}\eta_z) + \xi_y(f_1^{\pm}[-u \pm 2C]/\gamma) \\ f_1^{\pm}(\bar{u}\zeta_x + \bar{v}\zeta_y + \bar{w}\zeta_z) + \xi_z(f_1^{\pm}[-u \pm 2C]/\gamma) \\ f_1^{\pm}\{[-(\gamma - 1)\bar{u}^2 \pm 2(\gamma - 1)\bar{u}C + 2a^2]/(\gamma^2 + 1) \\ \qquad + (u^2 + v^2 + w^2)/2\} \end{bmatrix}$$

APPENDIX C:

BOUNDARY CONDITIONS USED IN CFL3D

Standard Boundary Conditions:

1000	free stream
1001	reflection of x-z plane
1002	extrapolation
1003	inflow/outflow
1004	viscous surface
1005	inviscid surface
1006	x-y plane
1007	axisymmetric

Special Purpose Conditions:

1146	jet exit plane